University of Sussex

Tracing star formation and AGN activity at radio frequencies

Dániel Csaba Molnár

Submitted for the degree of Doctor of Philosophy

University of Sussex

May 2018

Declaration

I hereby declare that this thesis has not been and will not be submitted in whole or in part to another University for the award of any other degree. This thesis is written in the paper based style, as approved by the University.

Chapter 2 was published in *Further evidence for a quasar-driven jet impacting its neighbour galaxy: The saga of HE0450-2958 continues*, Molnár et al., 2017, Monthly Notices of the Royal Astronomical Society, Volume 467, Issue 1, p.586-596. I contributed to all aspects of this paper, with other authors giving comments, advice and helped in some aspects of the analysis.

Chapter 3 was published in *The infrared-radio correlation of spheroid- and disc-dominated star-forming galaxies to $z \sim 1.5$ in the COSMOS field*, Molnár et al., 2018, Monthly Notices of the Royal Astronomical Society, Volume 475, Issue 1, p.827-838. I contributed to all aspects of this paper, with other authors giving comments, helped in some aspects of the analysis and provided access to data.

Signature:

Dániel Csaba Molnár

UNIVERSITY OF SUSSEX

Dániel Csaba Molnár, Doctor of Philosophy

Tracing star formation and AGN activity at radio frequencies

Summary

My research has focused on locating and measuring star formation and AGN activity in different environments with interferometric and single-dish radio observations. As my first PhD project, I studied the complex interaction between an intermediate redshift ($z \sim 0.3$) starburst galaxy and a nearby (~ 7 kpc separation) QSO using sub-arcsecond VLA observations. I found new evidence for jet-induced star formation activity in the companion galaxy, making the system a strong candidate for this rare, and potentially important process in the early Universe. In my second paper, I investigated the infrared-radio correlation (IRRC) of spheroid- and disc-dominated galaxies in the COSMOS field out to $z \sim 1.5$. With 1.4 GHz data and Herschel photometry I found that the redshift evolution reported in recent works is due to an increasing radio excess emission associated with spheroid-dominated galaxies, compared to disc-dominated ones, i.e. the 'purest' star-forming systems in our sample. I theorize that the extra radio power in spheroid-dominated systems is due to low-level AGN activity, even though these sources were not identified by most commonly-used diagnostics as AGN hosts. This finding will significantly increase the accuracy of future high-redshift radio surveys measuring star formation. In my third project I assembled and analysed the largest-to-date low-z IRRC sample of galaxies. I demonstrated the importance of selection effects influencing IRRC statistics, and carried out an improved IRRC analysis that yielded more accurate measures of the correlation's properties. With rich ancillary data it will provide insight into the physical processes that give rise to the IRRC. Finally, I adopted an MCMC-based model optimization to fit a radiative transfer model to ammonia line spectra of a binary molecular cloud core. I determined the physical structures and the masses of the cores and found they are gravitationally unbound.

Acknowledgements

Ezt a dolgozatot édesanyámnak, és eltávozott nagyszüleimnek, Teri mamának, Jenő papának és Árpi papának ajánlom. Hiányoztok nagyon, de remélem jól érzitek magatokat fényév távolsagra innen! Igyekszem gyakran arra nézni.

This thesis is dedicated to my mother, and my grandparents who passed away, Teri mama, Jenő papa and Árpi papa. I miss you a lot, but I hope you're having a good time light-years away from here! I often try to look your way.

First and foremost I owe the largest and most sincere thanks to my supervisor, Mark Sargent! He kept me motivated and guided me tirelessly with great empathy and patience, and I cannot be grateful enough for all the effort (far beyond what is usual) he put into mentoring me.

I thank my 'temporary supervisors' and hosts in Zagreb and Heidelberg, Vernesa Smolčić and Eva Schinnerer, for providing me the awesome opportunity to join their teams and their excellent support for the rest of my PhD. My thanks to the entire VLA-COSMOS team and all my further collaborators named in the following pages for their great feedback that contributed in many many ways to this thesis. I also acknowledge support from the Science and Technology Facilities Council (grant number ST/M503836/1).

All the amazing friends I made in the past few years – you turned moving across the Channel to a strange new land into an exciting and fun journey. Special thanks go to my THOA housemates, who became my family-in-another-country. Alex for all those times he pulled the wrong token from the chaos bag; my lil' bro, Benoît, for standing by me since day one; Heena for patiently putting up with us; Ridwan, for every hearty laugh and also the quiet moments; and of course for THOA v2: Panka for the constant stream of treats from home; and Jacob for liking every single film we have seen together.

The staff and PhD community in the Astronomy Centre is exceptional. I am especially grateful to my officemates; Steve for being our all-time pubmeister, Charlotte and Antonio for welcoming me warmly (back in the ancient times), Sean for inspiring me to maybe, hopefully one day go back to running, and Michaela for that one time she brought Charlie in. My 'cosmic' nemeses Zé and Ana, the always-laughing Lucía, my late-dinner-mate Hannah, komrads Sunayana and Mateja,

Azizah, who kept me ‘humble’, Rose, my radio buddy, friend Ciaran and all the great people in the astro corridor receive massive thanks too. Last but not least, I want to say cheers to the legendary and respectful Dr. Scott ‘Bestie’ Clay and Dr. David ‘FacebookUser’ Sullivan for the top bants.

I owe a great deal of gratitude to the people who supported me during my extended visits. The Zagreb crew: Lana (potato!), Olga, Ivan, Mladen, Oskari, Nicola and Dinko. I still wear the sports department t-shirt! Special thanks go to Jacinta, who talked me through some very critical moments. I would also like to thank my dear friends in Heidelberg: Sarah for the irregular but lovely coffee breaks and Philipp for being my travelling room mate.

I am grateful to Saci for listening to my complaints even from the other end of the world. B811 – Gábor, István and Karesz. Thank you for the endless memes! Extended-B811 – Dia, thanks for letting us in your flat despite all the Klein bottles of the world coming with us, and thank you, Anna, for letting me become part of your family! I also thank the entire Szántód team (Dani & Kati, Pite, Ádám, Rita, Viki, Csibe, Nóri, Gyuri & Zsófi, KZD and Kálmán bá) for the annual summer retreats and your undying friendship. Here’s to another 10 years and more! Orsi, thank you for the burger breaks! Hugs to my token non-astro friend, Laura. Thanks to Száva and Anita for making me want to migrate to Zürich.

And finally, but most importantly, I want to express my love and gratitude to my family: my dad, Panka and Babi mama, who supported me during all of this despite the personal cost. I am grateful to Gabi for always making me feel at home. I would like to thank my aunts, Tünde and Noémi, for keeping the family together during difficult times.

Végül, de a legfontosabb helyen, szeretném kifejezni hálám es szeretetem családomnak: apukámnak, Pankának és Babi mamának, akik mindigvégig támogattak személyes áldozatuk árán is. Köszönöm Gabinak, hogy hála neki, mindig otthon éreztem magam. Továbbá szeretném megköszönni nagynénéimnek, Tündének és Noéminek, hogy együtt tartották a családot a nehéz idökben is.

The chances of finding out what's really going on in the Universe are so remote, the only thing to do is hang the sense of it and keep yourself occupied.

DOUGLAS ADAMS

Contents

List of Tables

List of Figures

Chapter 1

Introduction

Astronomy embodies the ancient quest of humanity to learn the nature of celestial objects. Thus, by design, it poses challenging questions to answer. Even in the age of space travel most subjects of our investigation are impossible to visit and directly study. And when we looked, we have been restricted to observe with unaided eyes throughout the most of our history. These obstacles, however, only inspired innovation – for example Galileo Galilei, in order to enhance his vision, turned a telescope towards the sky, and could describe new details of Solar system bodies and discovered that the Milky Way consists of many stars closely packed together; William Herschel found invisible, infrared radiation and thus was the first to expand our view on the Universe beyond visible light; Joseph von Fraunhofer built the spectroscope and paved the way of describing the chemical composition of stars and planets. With these new inventions our overall understanding of nature grew rapidly, which in turn aided the development of new technologies, resulting in a sudden growth of astrophysical knowledge in the 19^{th} century and turn of the 20^{th} century. Stars were classified based on their colours and composition, subsequently their evolutionary tracks were broadly drawn on the colour – absolute magnitude plane (the so-called Hertzsprung–Russell diagram; HRD), and it was established that our Solar system is part of a larger conglomerate of stars, the Milky Way. Absorption of stellar light in the interstellar space lead to the discovery of interstellar medium (ISM), gas and dust inhabiting the interstellar space.

In the early 20^{th} century, astronomical debate revolved around nebulae, mysterious, fuzzy looking objects. Some of them appeared blurred patches of light even with the largest telescopes of the time, and hence divided the scientific community; some believed they are all part of the Milky Way, which spans the entire Universe, others argued that the unresolved ones are much more distant collections of stars and ISM, so-called “island Universes” (a term coined by the philosopher Immanuel Kant) similar to our own Galaxy. This argument was settled mainly when Edwin Hubble could resolve some of the stars in the Andromeda galaxy. Among these he identified Cepheid-type

variable stars, whose absolute brightness is related to their pulsation periods (Leavitt and Pickering, 1912), thus provided a distance estimate that placed M31 outside of our Galaxy (Hubble, 1929b). Measuring the distances of several more nebulae with this technique, Hubble also found a relation between distance and spectral line shift (Hubble, 1929a). This shift, z, is defined as

$$z \equiv \frac{\lambda_{\rm obs} - \lambda_0}{\lambda_0}, \tag{1.1}$$

where $\lambda_{\rm obs}$ is the observed wavelength of a given spectral line, and λ_0 is its rest-frame wavelength at which the radiation was originally emitted by the source. It is non-zero if the relative velocity of the observer and the source is non-zero. Hubble's data showed that the further galaxies are, the more their lines are shifted towards longer wavelengths, (i.e. red in the optical regime, hence z in astronomy is called redshift) and became known as Hubble's Law. This result implies that almost all other galaxies are moving away from ours, which lead to the discovery of the expanding Universe. Hubble's initial calibration of redshift as a measure for distance has been superseded since then by more sophisticated models (most recently e.g. Planck Collaboration et al., 2016), nevertheless modern cosmology can relate observed redshifts to cosmological distances.

Since Hubble's observations, nearly a century ago, extragalactic astronomy, the branch of astrophysics that studies the properties, formation and evolution of galaxies, became one of the most important fields of modern astronomy.

1.1 Galaxies

Galaxies are gravitationally bound systems that consist of stars, ISM and dark matter. The observed variety of their shapes and colours naturally raise questions, such as e.g. what physical processes form the different types of galaxies, how does their stellar content change with time, how do they interact, etc. In order to form a framework in which these questions can be understood, Edwin Hubble grouped galaxies into different types according to their apparent optical morphologies. This so-called Hubble tuning fork or Hubble sequence, with some more recent extensions, is a tool used even today to study galaxies. Fig. 1.1. presents a schematic illustration of the Hubble morphological classes.

The main types are: ellipticals (**E**), normal and barred spirals (**S** and **SB**, respectively) and irregular galaxies (**Irr**). Ellipticals are relaxed, generally featureless systems with smooth light distributions that appear as ellipses on optical images. According to how elongated they look, they are further split into E0 – E7 classes, where the integer is the measured, rounded ellipticity of a given source. By this definition, E0's are round and E7's are very elongated. This classification however, is not directly linked to their true 3D physical structures, but rather their projected shape,

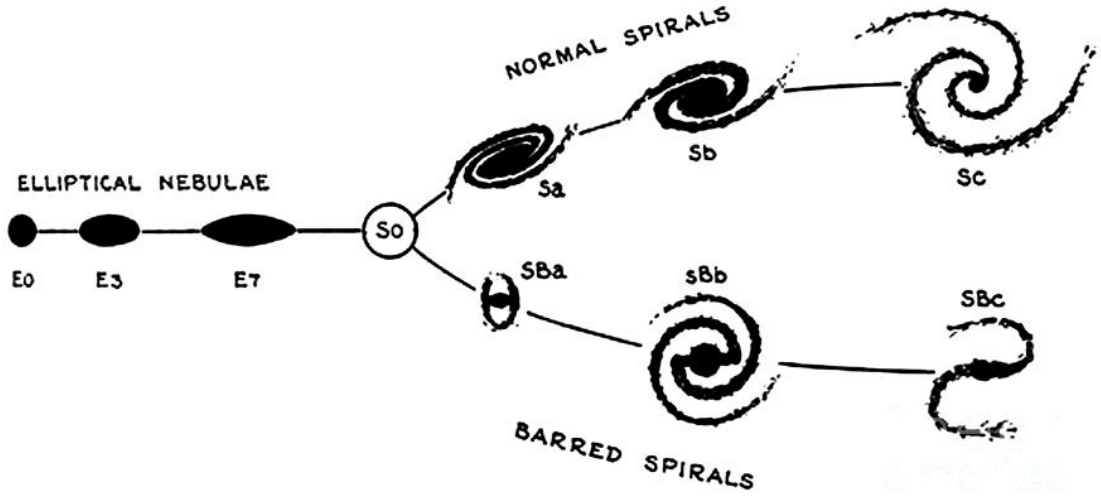

Figure 1.1: The Hubble tuning fork diagram illustrating galaxy morphology types. From: Hubble (1936).

which depends on our viewing angle, e.g. an E0 can be a face-on system while an E7 edge-on, and still have similar intrinsic shapes. Spirals show more complex structures – a central concentration of light, called the bulge, and a flattened disk. SB sources have a linear structure crossing the bulge, called a bar. Spiral arms are local maxima of stellar distribution with many young stars, and they originate from the bulge in S galaxies and from the endpoints of the bar in SB's. Subcategories for both S and SB objects are denoted by latters a, ab, b, bc, c, cd and d, where Sa and SBa galaxies have tightly wound up spiral arms and a dominant bulge, and Sd and SBd sources have patchy, fragmented arms with wide opening angles, and relatively faint bulges. There is a further transition class between ellipticals and spirals, the lenticulars (**S0**). These are also disk galaxies with a central bulge, similar to spirals, but do not have spiral arms. Finally, irregulars are galaxies that do not fit into any of these previous classes due to their disturbed, amorphous shapes. These are often interacting systems. It is common practice to call ellipticals and lenticulars "early-types", and spirals and irregulars "late-types". It should be emphasized, that this nomenclature is not indicative of any time evolution whereby e.g. early-types transform into late-types, it is rather just a historical artefact.

Observations show that these different classes of galaxies have on average different physical properties. For example, elliptical sources on average have older stellar populations, their stellar kinematics are dominated by random motions, on the other hand, spirals are younger objects that actively form stars, and their stellar orbits are more regular. However, these types fail to capture some differences in other fundamental properties, such as masses and sizes. As a result,

nowadays the Hubble scheme is mainly used as a classification tool, while the main questions of extragalactic astronomy focus on understanding the physical processes that regulate various galaxy characteristics (e.g. stellar and gas masses, star formation properties, etc.) and investigate how different scaling relations came to be (e.g. between stellar mass and star formation rate – see Sect. 1.1.1; central black hole mass and bulge mass – see Sect. 1.1.4, etc.). These correlations suggest, that similar galaxies in the multi-dimensional space of morphologies and other physical parameters have fairly similar formative and evolutionary histories, i.e. the way their baryons were assembled is similar – we ultimately wish to link these to observable quantities. My work has mainly focussed on galaxy evolution, thus in order to give my thesis results a broader context, I will now describe some important process that influence galaxy formation.

1.1.1 Star formation

The Universe's dark matter distribution provides the framework for galaxy evolution. It produces a large scale gravitational potential, which pulls baryons towards large assemblies, haloes of dark matter. This in-falling gas is initially heated via shocks. Once it reaches thermal equilibrium in the halo (10^4 – -10^8 K) it cools via bremsstrahlung and collisions followed by photon emission and decay to ground state. If the gas has some heavy elements or molecules, emission line radiation adds another cooling channel. Since these processes require two particles, they are typically more efficient at higher densities. Eventually gas cools and migrates to the centre of the dark matter halo forming a protogalaxy.

A small fraction of cold gas condensates into clusters of stars across the galaxy (more on this process in Sect. 1.1.3). The mass distribution of a newly formed stellar population is called the initial mass function (IMF). There are different formulae that give its precise functional form (e.g. Salpeter, 1955; Kroupa, 2001; Chabrier, 2003, are commonly used). The most massive stars ($\geq$ 8 $M_{\odot}$) among these use up their hydrogen reservoirs rapidly (in $\sim$ 10^7 – 10^8 years), and return heavier elements, that were produced during their life, into the surrounding ISM via supernova explosions. This enriches the ISM with metals, which will subsequently form new generations of stars. Less massive stars on the other hand spend several Gyrs on the stellar main sequence, and hence effectively lock material away from this galactic gas circulation. Galaxies can replenish their gas supplies and continue forming new stars by accreting gas from the inter galactic medium (IGM), or by merging with other galaxies, and thus gradually, or in bursts, undergo stellar mass growth. These processes give off a number of detectable signatures – young stars emit photons at ultraviolet wavelengths, which are then absorbed by interstellar dust, and re-processed into infrared radiation. They also ionize the ISM in their vicinity, which gives rise to nebular line emission. Once they

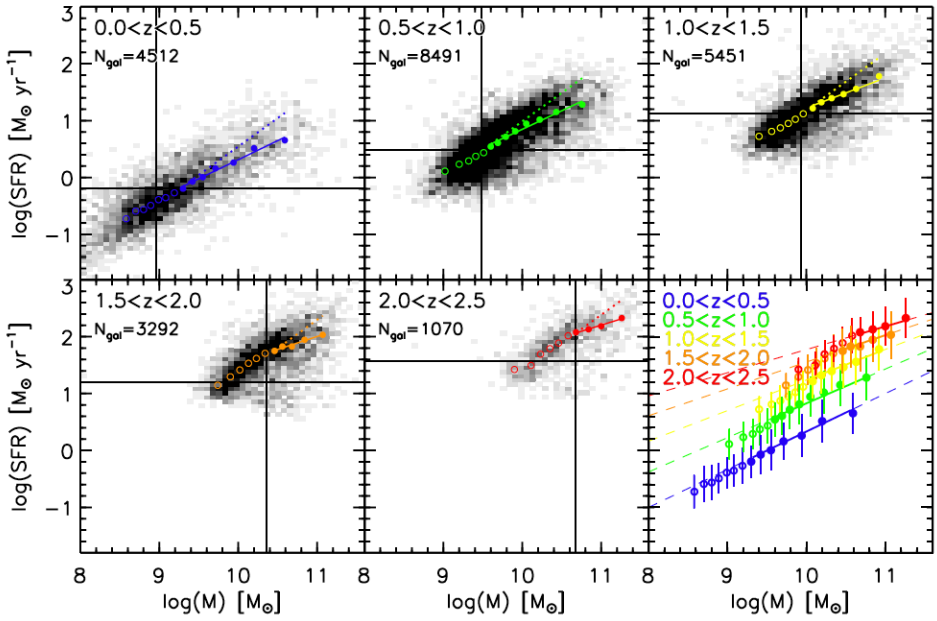

Figure 1.2: The star forming main sequence in the $0 < z < 2.5$ regime. The normalization and slope of the relation changes with some evidence of a flattening high-mass end. From: Whitaker et al. (2012).

turn into supernovae, they produce relativistic electrons that give rise to radio frequency emission. Radio is not affected by dust extinction unlike shorter wavelength emission, which requires some additional measure of dust reddening, and thus provides a direct view of star forming regions. For a more detailed description of star formation tracers see Sect. 1.2.1.

Star formation is commonly quantified through the star-formation rate (SFR), ψ,

$$\psi \equiv \frac{M_*}{t}, \tag{1.2}$$

where M_* is the total stellar mass of stars formed in t time. During the past decade, it was found that most galaxies, both in the local and the distant Universe, show a linear correlation in the log(M_*) – log(SFR) plane, known as the star forming main sequence (SF MS, see e.g. Brinchmann et al., 2004; Noeske et al., 2007; Elbaz et al., 2007, 2011; Speagle et al., 2014; Schreiber et al., 2015; Tomczak et al., 2016), as seen in Fig. 1.2. The mass and redshift independence of its scatter ($\sim$ 0.3 dex) suggests quasi-static, secular growth is the dominant mode of star formation. MS galaxies are thought to fluctuate about the ridge of the MS (Tacchella et al., 2016). In this picture, gas compaction (triggered by e.g. merger events or disc instabilities), and subsequent star formation moves galaxies upwards and right in the log(M_*) – log(SFR) plane, then once the gas is depleted, they migrate downward, and finally upturn occurs when fresh gas falls onto the disc. In a smaller fraction of galaxies, more violent, chaotic process, e.g. major mergers, lead to strong bursts of star

formation, and elevate them above the SF MS (e.g. Sargent et al., 2012, 2014). If gas supplies are not replenished, galaxies migrate below the SF MS and become quenched.

Over the past two decades, surveys probing the cosmic star formation rate density (i.e. the total star formation rate per comoving volume) found that it peaked around z ≈ 2 (when the Universe was ∼ 3.5 Gyrs old; an epoch that is now known as the "cosmic noon"), and shortly after it begun an exponential decline until the present day (for a review, see Madau and Dickinson, 2014). This implies that half of the stellar mass in the local Universe was formed before z ≈ 1.3. Interestingly, the rise and fall of cosmic star formation is coincident with the same trend in the accretion rate of central galactic black holes, hinting at a coevolution of galaxies and their super massive black holes. In the following section I will describe active galaxies, that came to be as a consequence of central black hole accretion, and by triggering energetic processes, significantly impact galaxy evolution.

1.1.2 Active galaxies

Besides star formation, another important process that regulates the growth of galaxies is the mass accretion onto their central super massive black hole (SMBH). This episodically produces electromagnetic (EM) radiation at all wavelengths from X-ray to radio, and launches energetic particles in all directions, providing heat input into its host galaxy's ISM and the surrounding IGM.

Galaxies, whose spectra show significant excess non-stellar radiation at some (or all) EM wavelengths linked to SMBH activity, are called active galaxies. Their compact, central regions around the SMBH are the Active Galactic Nuclei (AGN). Since all galaxies harbour a central SMBH, and AGN activity is tied to SMBH accretion, most galaxies experience AGN episodes at some point during their history. The AGN fraction is ∼ 10 – 20 % of the total galaxy population at a given epoch, suggesting that their lifespans are relatively short (eg. Gu et al., 2018). Historically AGN are generally split into three main classes:

- **Quasi-stellar objects** Matthews and Sandage (1963) found "starlike" objects spatially coincident with three radio sources (3C 48, 3C 196, and 3C 286). Using lunar occultation, Hazard et al. (1963) determined the accurate position of another radio source 3C 273, which in turn allowed Schmidt (1963) to associate it with a point-like optical source, whose spectra showed strong and broad emission lines. By identifying these lines as hydrogen Balmer series emission, he put the source at redshift of 0.158, which was unusually high at the time. This suggested it is ∼ 100 times brighter than an average spiral galaxy, yet due to its point-like appearance, it is very compact as well. Later, as a result of increasing radio source position accuracies, many more of these quasi-stellar radio-sources (quasars) were

found. The unusually blue colour of quasar optical spectra prompted searches at optical wavelengths as well, revealing a roughly ten times larger population of radio quiet quasars, also known as quasi-stellar objects (QSOs). These also have strong emission lines, generally high redshifts, and higher than average, time varying luminosities that outshine their host galaxies. Since later faint radio emission associated with them was detected, the previous distinction of quasars and QSOs are not valid any more, nowadays they are typically used interchangeably.

- **Seyfert galaxies** The earliest detected AGN type (Seyfert, 1943). They are spiral galaxies with extremely bright cores, whose spectra exhibits strong, broad emission lines. There are two main subclasses – Type 1 and 2. Seyfert 1 galaxies have both narrow (i.e. several hundred km/s – already larger than typical galactic rational velocities) and broad (up to 10^4 km/s) lines, while Seyfert 2 only has narrow lines. Osterbrock (1981) introduced intermediate classes (e.g. Seyfert 1.5 or 1.9), where broad-line emission is present, but less prominent than in Seyfert 1 objects. Seyfert galaxies in general are fainter in optical than QSOs, but show very similar spectral properties.

- **Radio galaxies** These AGN reside in elliptical galaxies. Similar to Seyferts, they can also be classified into broad-line and narrow-line radio galaxies (BLRGs and NLRGs, respectively). In fact, they can be considered as radio-loud Seyfert 1 and 2 sources with a different optical morphology.

Extended radio emission associated with AGN often observed to have a double structure – two radio lobes roughly symmetrically around a central core. The lobes usually can be connected to the centre via linear emission structures, jets. These extended radio sources can be typically divided into Fanaroff-Riley Type I and II (FR I and FR II, respectively; Fanaroff and Riley, 1974). FR I sources are brighter near the core and gradually become fainter with increasing angular distance from it, and thus sometimes are referred to as core-brightened objects. They tend to be fainter than $L_{1.4\mathrm{GHz}} \leqslant 10^{24}$ W Hz^{-1}. Meanwhile, FR II sources' surface brightness increases outwards (i.e. are edge-brightened), and have $L_{1.4\mathrm{GHz}} \geqslant 10^{24}$ W Hz^{-1}. Fig. 1.3 shows examples for both types. FR I and II sources are also distinct in host optical luminosity – radio luminosity plane (e.g. Ledlow and Owen, 1996), suggesting that radio morphologies are linked to host properties.

The broadly accepted unification scheme attempts to link these various types of AGN together from a theoretical perspective (see e.g. Rowan-Robinson, 1977; Urry and Padovani, 1995). According to this, the AGN classes are a consequence of varying viewing angles of the AGN host galaxy.

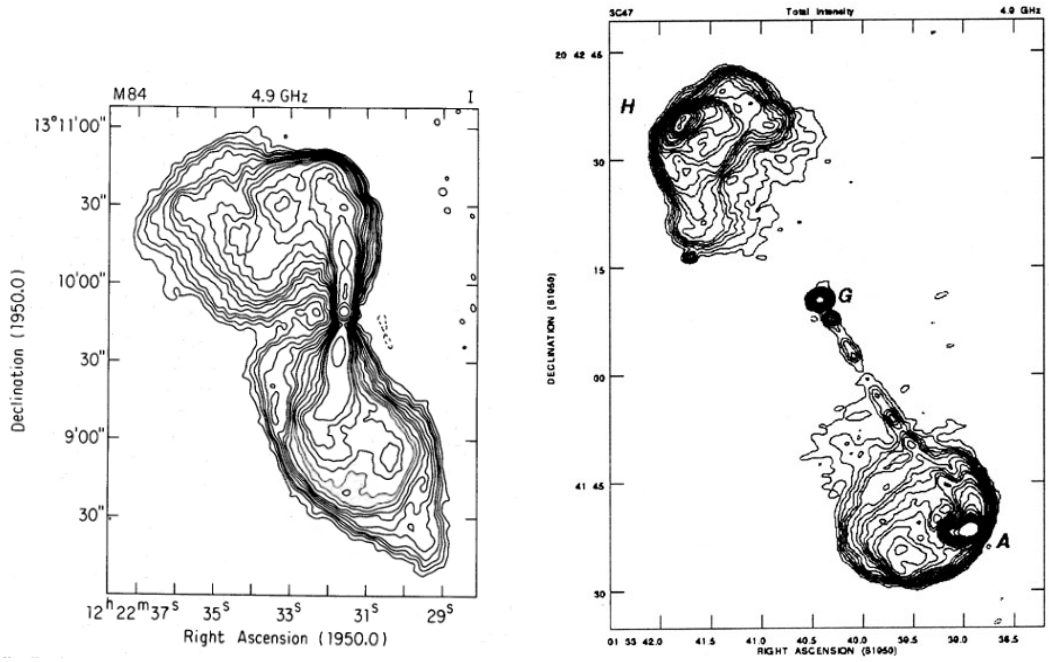

Figure 1.3: Examples of an FR I (**left**) and FR II (**right**) radio source at 4.9 GHz. From: Laing and Bridle (1987) and Bridle et al. (1994).

In this unification picture, the central engine of the AGN is the SMBH. It accretes material, which due to its finite angular momentum, assembles into a disk, whose plane is perpendicular to the rotation's angular momentum vector. Through internal friction, gas in the disk slowly decelerates, moves towards the centre, and as a result converts its potential energy into kinetic energy and heat, which then powers AGN processes. Due to the temperature gradient in the disk, its spectrum is a stretched black body radiation curve that peaks at UV and optical wavelengths. Gas clouds outside of the accretion disks' plane, but close to the SMBH have high velocities due to the SMBH's high gravitational potential, while clouds further from it move slower, thus giving rise to the observed broad and narrow lines, respectively. Jet material is pushed out towards the poles, likely due to complex magneto-hydrodynamic processes. In the jet, synchrotron radiation and inverse Compton scattering result in emission at radio and X-ray wavelengths, respectively. A dust torus surrounds the accretion disk further away from the SMBH. At large viewing angles, it obscures emission from the broad line region and the disk. Then subsequently re-emits them usually at mid-IR (MIR) wavelengths. The brightest QSOs can heat dust even further out, and thus produce significant far-IR (FIR) emission (Symeonidis et al., 2016). Fig. 1.4 presents a sketch that summarises the main ideas. It has been mentioned, that all of these processes are powered by material accretion onto the SMBH. Thus, in Sect. 1.1.3 I will inspect in more detail the ISM of galaxies.

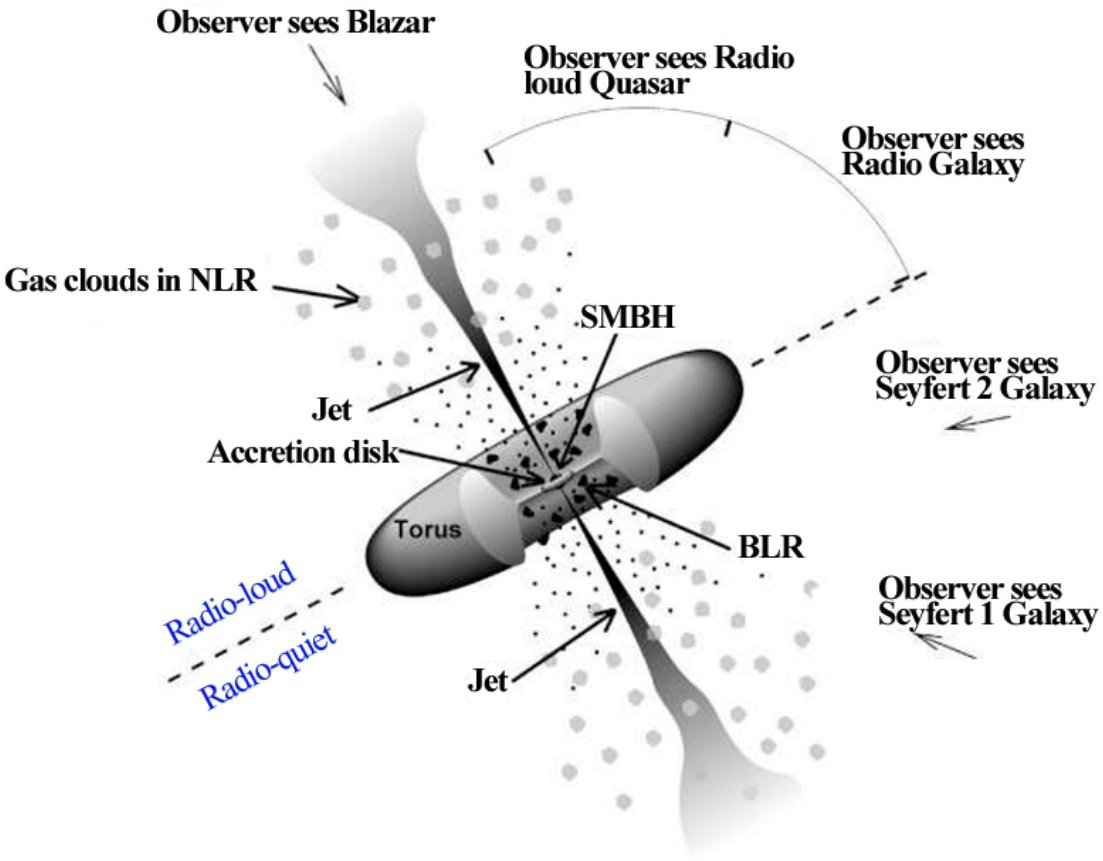

Figure 1.4: Illustration of the AGN unification scheme. Whether a source is classified as one of the various of types of AGN discussed in Sect. 1.1.2 mainly depends on the viewing angle, represented by arrows in this figure. Dashed line shows the divide between radio-loud and -quiet sources – similar inclinations can result in a galaxy being Seyfert or a radio galaxy depending on its radio luminosity. Credit: Fermi and NASA: https://fermi.gsfc.nasa.gov/science/eteu/agn/.

Table 1.1: Main physical properties of the various ISM phases, as measured in the Milky Way. Adopted from Table I of Ferrière (2001).

Gas phase	Temperature [K]	Density [cm^{-3}]	Ionization rate
Molecular	10 – 20	10^2 – 10^6	$<10^{-6}$
Cold atomic	50 – 100	20 – 50	$\sim 10^{-4}$
Warm atomic	6,000 – 10,000	0.2 – 0.5	~ 0.1
Warm ionized	$\sim$ 8,000	0.2 – 0.5	1
Hot ionized	$\sim 10^6$	$\sim 10^{-2}$	1

1.1.3 Cosmic gas and dust

The fuel for star formation and black hole accretion is interstellar gas. Its main component at low densities is neutral hydrogen (Kalberla and Kerp, 2009). It has a multi-phase structure coupled to the stellar content of the galaxy – stars form in the coldest, densest regions, then through their ultraviolet (UV) radiation they ionize large volumes of the ISM. Table 1.1 shows a summary of the main physical parameters of the different ISM phases (for more details see Ferrière, 2001, and references therein). The outermost layer is the hot ionized phase. It is mainly heated by supernovae, and thus forms structures resembling bubbles and fountains. Its scale height is of order $\sim$ kpc, hence it is also referred to as coronal gas. The warm ionized medium is mainly ionized by photons, and occasionally through collisions. In disk galaxies it is more confined to the disk, than the coronal gas. The bulk of the galactic ionized hydrogen is in this phase, a smaller fraction in HII regions near hot stars. Warm neutral medium gives around one third of the ISM volume in the Milky Way. It mainly appears in photodissociation regions, in the interface of HII regions and molecular clouds, thus it is sometimes called the warm intercloud region as well. The cold atomic or neutral phase is structured into sheets and filaments. It is spatially more concentrated than the previously described phases, as it gives only $\sim 1 - 5$ % of the ISM volume. It is roughly in pressure equilibrium with its environment.

Individual stars are almost exclusively formed in giant molecular clouds (GMCs), loosely bound assemblies of gas and dust in the ISM, that are nestled into the previously discussed warmer gas phases. Typically GMCs have masses of 10^3 – $10^7 M_\odot$, densities of 10^2 – $10^6 cm^3$, temperatures of 10 – 20 K and linear sizes up to a $\sim$ 100 pc. They give $\sim$ 30 % of the total ISM mass but only ≤ 1 % of its volume. These conditions ensure that the inner regions of GMCs are effectively self-shielded from the ionizing radiation of massive stars in their host galaxy, and as a result molecules can form and survive in them. This in turn allows efficient cooling through molecular line emission, and thus

the densest parts of the cloud, the so-called cloud cores, can reach densities where gravitational collapse can form stars. The lifespan of a typical Milky Way GMC is $\sim 10^7$ years and converts ~ 2 % of its mass into stars (Murray, 2011). Their most common molecule is H_2. At low temperatures, due to its lack of electromagnetic dipole, H_2 cannot be observed, hence GMCs are usually mapped using their second most abundant molecule, carbon dioxide (CO). Especially dense regions, such as GMC cloud cores are traced well by e.g. hydrogen-cyanide (HCN) and ammonia emission (NH_3). The work presented in Chapter 5, investigating the physical properties of two GMC cores, was thus based on ammonia spectral line measurements.

Mixed with gas, the ISM also contains solid particles, dust. It plays a crucial role in interstellar molecule formation, because it accelerates atomic hydrogen combination to H_2 on its surface, and shields dense regions of ISM from ionizing radiation, which protects molecules from photodissociation.

A traditional way to estimate the critical mass of a cloud core, above which the gas becomes unstable and gravitational collapse begins, is to calculate its thermal Jeans mass, M_J, as

$$M_J = 4.79 M_\odot \left(\frac{T}{10K}\right)^{3/2} \left(\frac{n}{10^4 cm^{-3}}\right)^{-1/2}, \tag{1.3}$$

where T is the kinetic temperature and n is the gas volume density (Jeans, 1902). This formula neglects any additional terms for e.g. magnetic fields, external pressure and rotation, some of which stabilises against the collapse. These forces generally keep the core in equilibrium, while it accretes material from its vicinity. In Chapter 5 I used another equation from MacLaren et al. (1988) to calculate the virial mass, $M_{\rm vir}$, of the core as

$$M_{\rm vir} = k_2 R \Delta v^2, \tag{1.4}$$

where R is the radius of the clump, Δv is the total velocity dispersion and k_2 is a factor that depends on assumptions such as the shape of the velocity distribution and the density profile of the clump. The total velocity dispersion contains the turbulent and thermal velocity components, hence it is more sophisticated than Eq. 1.3.

Once the cloud core's mass has exceeded its Jeans or virial mass, either by accretion driven growth or due to an external trigger, e.g. a supernova induced shock, gravitational collapse begins. It starts to contract and often breaks into smaller fragments. Central densities and temperatures rise until deuterium fusion starts in the centre, and thus a protostar is born. Having briefly established star formation and AGN characteristics in previous sections, as well as the ISM that feeds both, I will now combine these and outline main feedback processes, a channel through which these components interact.

1.1.4 Feedback processes

From the naive picture of star formation briefly discussed in Sect. 1.1.1, one could expect that galaxy masses are roughly proportional to the masses of their host dark matter haloes, since more massive haloes can simply accrete larger amounts of baryons. However, comparing observed galaxy luminosity distributions, best fitted by a Schechter (1976) function, to theoretical predictions from numerically simulated halo mass functions (such as the Millennium simulation; Springel et al., 2005) rescaled using a mass-to-light ratio that creates an overlap in between them at L_*[1], shows a shortage of galaxies at high and low masses (see Fig. 1.5 that illustrates this tension). This suggests that a key ingredient is missing from the so far discussed, simplistic star formation and galaxy evolution model – energy input from stellar and AGN feedback, and other processes that remove or heat the gas content of galaxies, and as a result slow down or quench star formation.

In dwarf galaxies it is typically in the form of supernova driven winds and shocks, that can expel their gas. This is only effective in these low mass systems, since their gravitational potential is lower than in more massive galaxies, and thus it requires less energy to remove their gas content. It is worth noting, however, that supernova driven gas shells can sweep material together and trigger new star formation events as well in all types of galaxies. Small galaxies are also more likely to be influenced by environmental effects. During tidal stripping, more massive, nearby galaxies acquire gas and stars from them. Ram pressure stripping is a process, whereby galaxies moving through intra-cluster medium (ICM), the hot, X-ray emitting gas that permeates galaxy clusters, experience "headwind" from the ICM moving relative to them, which can removes their cold gas reservoirs. Yet another process that quenches cluster galaxies is strangulation. When galaxies first fall into a cluster, the cluster's potential can create tidal effects that move the their gas into the ICM.

High mass galaxies strongly hold on to their gas reservoirs, hence are more resilient against the effects discussed above. However, they are also more likely to harbour AGN that inject vast amounts of energy into their ISM and the surrounding IGM/ICM, thus AGN driven feedback is the dominant process that quenches star formation in these systems. This so-called negative AGN feedback has two flavours. The radiative mode (also known as 'quasar', 'wind' or 'cold' mode) occurs in luminous QSOs when their SMBH is close to the Eddington limit. It produces such a high flux of radiation that it pushes gas out of the host galaxy, terminating on-going star formation. The other mode is the kinetic mode (or 'radio', 'jet', 'maintenance' or 'hot' mode), where the accreting SMBH drives jets, which transport energy into the surrounding IGM, and by keeping it hot, it inhibits the gas cooling and falling onto its host galaxy. Eventually the host uses up its cold gas reservoir and without replenishment, star formation ceases. This process more likely to occur

[1]Where L_* is the characteristic luminosity of the Schechter (1976) function, the "knee" of the distribution.

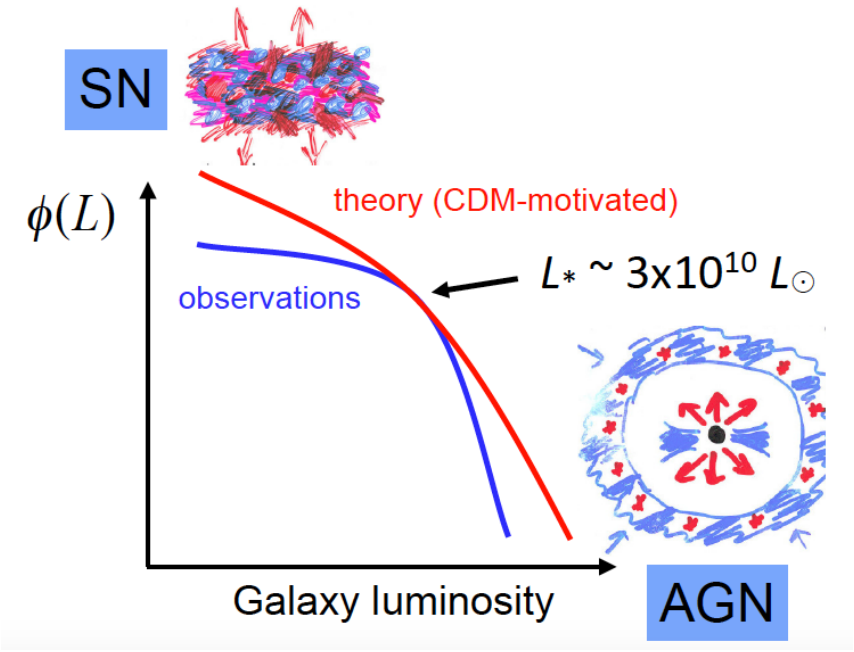

Figure 1.5: Sketch showing the impact feedback globally has on galaxy evolution. Red curve shows a galaxy luminosity function directly rescaled from simulated halo mass distribution, blue observed galaxy luminosity distribution following a Schechter (1976) function. From: Silk and Mamon (2012).

at low Eddington ratios. For more details see Fabian (2012).

There is evidence, that AGN driven winds and jets can act as triggers for star formation activity, as on-going star formation or molecular gas has been observed in the presence of powerful radio jets (Salomé et al., 2015) as well as in QSO companion galaxies (e.g. Papadopoulos et al., 2008; Decarli et al., 2017). There are only a handful sources in which a radio jet-molecular gas interaction is observationally confirmed (such as Minkowski's Object, Croft et al. 2006, and Centaurus A Schiminovich et al. 1994; Charmandaris et al. 2000), which might suggest that it is a rare phenomenon. However, most likely we do not have a complete census of these objects due to observational difficulties. At high redshifts there are hints that they could play a more prominent role in star formation (e.g. Silk, 2013).

It was found in hydrodynamic simulations that an assembly of mainly atomic gas can be converted into warm, molecular matter on $\sim 10^6$ year time scales via turbulent compression (Glover and Mac Low, 2007). Nesvadba et al. (2011) reports the detection of a highly turbulent molecular disk in the radio galaxy 3C 326, whose short dissipation time scale suggests once kinetic energy input from the jet subsides, the gas will rapidly cool, collapse and form stars. The paper presented in Chapter 2 examines a system in which this phenomenon might occur.

Another clue that AGN activity might affect host galaxy properties is the observed correlation

between mass of the central SMBH and the luminosity, velocity dispersion or stellar mass of its host galaxy in the local Universe (e.g. Magorrian et al., 1998; Ferrarese and Merritt, 2000; Ferrarese et al., 2006, respectively). Some argue that it is merely the outcome of similar stochastic effects due to hierarchical merging (Jahnke and Macciò, 2011), or the result of similar gas consumption rates for both star formation and SMBH growth (Mullaney et al., 2012). Others claim that it is feedback, that links them together (Silk and Mamon, 2012). Nevertheless, cosmic star formation rate and SMBH accretion rate appear to follow very similar trends across cosmic time, suggesting an AGN activity – star formation connection (Madau and Dickinson, 2014). With the basic concepts of galaxy formation and growth discussed, in the next section I am going to outline some theoretical approaches that are crucial in understanding the detailed physics behind it, and work in tandem with the data-driven research I have conducted.

1.1.5 Modelling approaches

This previously discussed complexity of galaxy evolution, and the interaction of physical processes on vast spatial and temporal scales mean that in order to provide a consistent physical model of galaxies, one ultimately needs to turn to numerical methods, rather than analytical techniques.

These numerical simulations have two families – semi-analytical models (SAMs) and hydrodynamical simulations. Present day computing limitations do not allow sub-pc resolution required by star formation and SMBH growth physics in large, cosmological volumes. SAMs were invented to circumvent this constraint and provide a tool to statistically study large galaxy populations. They take merger trees from dark matter only simulations, and populate them with baryons, whose physical properties are computed following analytical recipes, 'sub-grid physics' applied to small scales and by tracing them through a branch of the merger tree. Thus galaxies' secular growth follows the input physics, and undergo merger events according to the cosmology used to create the merger trees. A major advantage of SAMs is their flexibility – they are relatively fast to run, and therefore one can tune parameters in the sub-grid recipes to match observed scaling relations, abundances, redshift evolution, etc. It is also common practice to use SAMs to gauge the impact of a specific physical process (e.g. a given type of feedback) on galaxy evolution by comparing results between simulations done with and without a particular element of the sub-grid model. With increasingly good observational constraints the complexity of these models have also grown rapidly. Some widely used modern SAMs are the Munich galaxy formation model (Henriques et al., 2015), GALFORM (Lacey et al., 2016) and SAGE (Croton et al., 2016).

On the other hand, hydrodynamical simulations attempt to provide a more self-consistent framework to model baryonic physics by tracing hydrodynamical processes and gravity individually

for all particles in their model box. Their main advantage is that they provide spatial and temporal information about the distribution of gas and stars as opposed to SAMs, which assume e.g. a given analytic radial profile. As a result, hydrodynamic simulations are significantly more computationally expensive than SAMs. However, they still cannot resolve the smallest scales, such as individual stars, and thus also rely on sub-grid recipes to some degree. Depending on their resolution they either contain large number of galaxies and model their interactions or focus on the detailed processes in one galaxy (targets for these so-called 'zoom-in' simulations are often selected from larger, lower resolution runs). Due to the computational limitations, large scale hydrodynamical simulations are less common compared to SAMs, but current state-of-the-art hydrodynamic codes, such as the Illustris Project (Vogelsberger et al., 2014) and EAGLE (Schaye et al., 2015), have made significant progress in producing galaxy populations that match various observed statistical galaxy properties.

Mock observations from hydrodynamic models and population statistics from SAMs are compared to measured data to check model validity, and to make observational predictions. In the following section I will discuss various observing approaches that provide input for these theoretical studies, in particular the ones I used during my PhD work.

1.2 Observational signatures

The physical processes discussed in Sect. 1.1 give rise to EM emission at various wavelengths. In this section I will briefly describe observational signatures of star formation and AGN activity, and outline the main concepts of radio interferometry, which I used to study both.

1.2.1 Tracing star formation

Most pre-main sequence stars are deeply embedded in the gas and dust cloud in which they were formed, thus directly detecting their radiation is observationally difficult. Hot main sequence stars, on the other hand, are bright and less obscured, since they have cleared their immediate vicinity, and due to their short $\sim$ 10–100 Myr lifespans they are also good proxies of recent star formation activity (see Sect. 3.1 of Madau and Dickinson, 2014, and references therein for more details).

UV radiation

In a given stellar population with the same age, low mass stars dominate the total stellar mass, but hot, massive ($M > 8\,M_{\odot}$) ones produce the bulk of the UV radiation. As a result, the measured UV emission is proportional to the number of young stars and hence the recent massive SFR.

The scaling factor depends on the rest-frame UV wavelength observed, and to some extent the metallicity of the stellar population. With a given IMF the total SFR can be determined. Even though UV flux is a relatively straightforward indicator of SFR, it comes with some difficulties. The most reliable, rest-frame far-UV emission, which has the smallest contribution from old low mass stars, is only observable by space telescopes (such as GALEX or the Hubble Space telescope) due to Earth's atmospheric absorption, or at $z > 1.4$ with ground-based facilities. However, the biggest issue is the substantial dust attenuation at short wavelengths. Additional measurements, at optical, infrared (IR) or other UV wavelengths are required to measure reddening, and calculate corrections allowing an estimate of the intrinsic UV luminosity. This dust-correction is correlated with galaxy properties, e.g. Fig. 1.6 illustrates its dependency on galaxy position in the SFR – M_* plane.

IR emission

UV radiation absorbed by dust is re-emitted at IR wavelengths. Therefore, the total IR emission (typically taken as the integrated luminosity between 8 – 1000 μm) is a measure of the energy (primarily from UV radiation) dust absorbed. As discussed above, most of the UV flux is from young stars, thus IR luminosity is proportional to the attenuated fraction of star formation. Combined with UV fluxes, it provides a good measure of the total SFR.

IR based SFR estimates have their caveats as well. Firstly, there are other processes than star formation that deposit energy into dust – dust toruses around AGN absorb non-stellar radiation, and old stellar populations are also capable of heating it. The latter, so-called cirrus component is non-negligible in e.g. nearby galaxies with very little on-going star formation. Secondly, observing IR is also difficult. Emission at submillimetre, millimetre, and certain wavelengths in near- and mid-IR are possible to detect from the ground, but far-IR is only observable from space. Lastly, the most reliable estimate of the IR luminosity requires spectral energy distribution (SED) fitting. Since the total IR SED of a galaxy is a mix of dust components of different temperatures (warm grains near young stars, colder ambient ISM dust, and possibly AGN heated dust), and spectral features such as polycyclic aromatic hydrocarbons (PAHs, which can be star formation indicators themselves) and silicate absorption bands, a well constrained fit needs some sampling the IR emission, thus, like UV emission, IR is not a single band proxy for SFR. Furthermore, since image resolution is decreasing with increasing wavelength, IR observations are more often confused, than their optical-UV counterparts. This an especially major challenge at far-IR wavelengths.

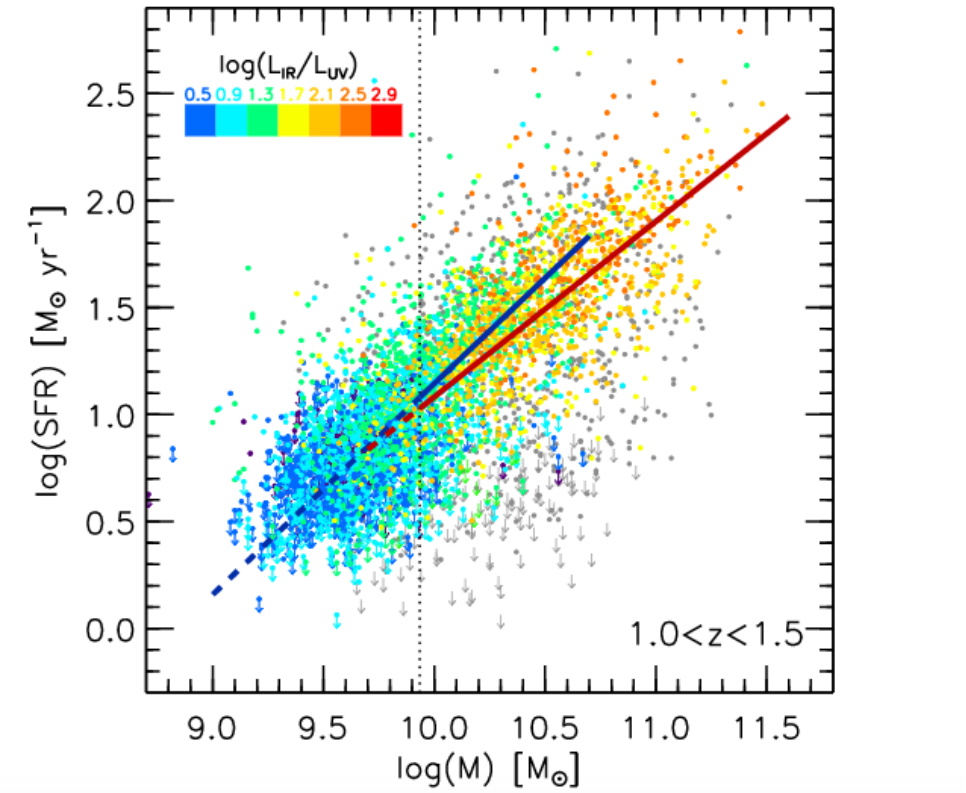

Figure 1.6: Ratio of IR and UV luminosities in the star formation rate – stellar mass plane. IR traces the bulk of the star formation towards the tip of the star forming main sequence, while its contribution to the total SFR below ~ 9.5 $\log(M/M_{\odot})$ drops to ~ 50 %. From: Whitaker et al. (2012).

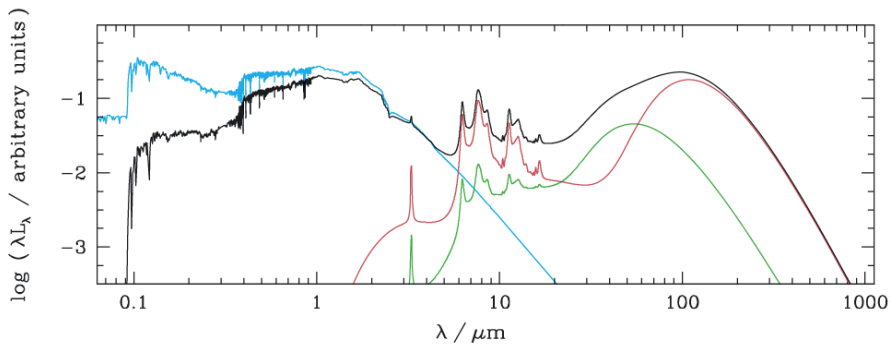

Figure 1.7: A typical star-forming galaxy's SED. The unattenuated stellar light is traced by the blue line, the emission by dust in warm stellar birth clouds is showed as a green line, the emission by dust in the ambient cold ISM is the red line. The total emission from the galaxy (black curve) is taken as the sum of the attenuated stellar spectrum and the total IR emission. This SED is computed by MAGPHYS, the SED-fitter used to derive $L_{\rm TIR}$ values in Chapter 3. From: da Cunha et al. (2008).

Nebular lines and X-ray

Nebular lines, emitted by gas mainly ionized by young, hot stars in HII zones, can also be used as proxies to UV radiation. However, these emission lines are heavily dust attenuated as well. Hydrogen recombination lines, specifically the Balmer-lines H_α and H_β are commonly observed to estimate SFR. Their ratio, i.e. the Balmer-decrement, is sensitive to the amount of absorbing dust, and hence can provide a measure of dust correction. A drawback of nebular line emission is the difficulty of detecting them, especially at high redshifts. In galaxies without an AGN X-ray emission arises from a combination of supernovae and stellar wind heated ISM gas and X-ray binaries, indicative of recent star formation activity. X-ray derived SFRs are highly sensitive to stellar population ages that affect the ratio of high- and low-mass binaries, moreover most of the cosmic X-ray flux is associated with AGN. Symeonidis et al. (2014) compared the IR and X-ray luminosities of AGN-free IR sources, and provided a new X-ray – SFR calibration.

Radio

In star-forming galaxies with no on-going AGN activity radio emission comes from two sources (see e.g. Condon, 1992). Electrons in HII regions around massive stars experience bremsstrahlung as they decelerate in the ionized medium's electric fields, which results in radio emission. The magnitude of this free-free (also called thermal) radiation is proportional to the number of young massive stars. Supernova remnants, the evolutionary endpoints of the same massive stars, accelerate cosmic ray (CR) electrons. CR electrons emit synchrotron (non-thermal) radiation as they move through galactic magnetic fields (for more details about the characteristics of synchrotron emission see Sect. 1.3.1). The total energy deposited into CR electrons by supernova events is proportional to the supernova rate, and as a result, the galactic SFR. Fig. 1.8 shows a typical radio spectrum with the free-free and synchrotron components. Synchrotron dominates the total radio flux up to $\sim$ 10 GHz, whereas free-free is more important at higher frequencies, $\sim$ 30 – 100 GHz.

In practice, it is very difficult to isolate free-free component in the observed radio flux density at any frequency due to its flat spectral distribution. One way to do it, is to measure radio luminosity at lower frequencies, where synchrotron is thought to be the sole contributor, then extrapolate this non-thermal emission to a higher frequency assuming a typical radio spectral slope[2] of ~ -0.7 – 0.8 (e.g. Kimball and Ivezić, 2008). A more sophisticated approach is to infer the number of ionizing photons from an independent tracer, such as H_α emission, and derive a thermal fraction (i.e. the ratio of thermal free-free to total radio flux) from that (Tabatabaei et al., 2007). Since

[2]The radio spectral slope or index is defined as $S_\nu \propto \nu^\alpha$, where S_ν is the flux density at frequency ν. For details on the origins of this power law, see Sect. 1.3.1.

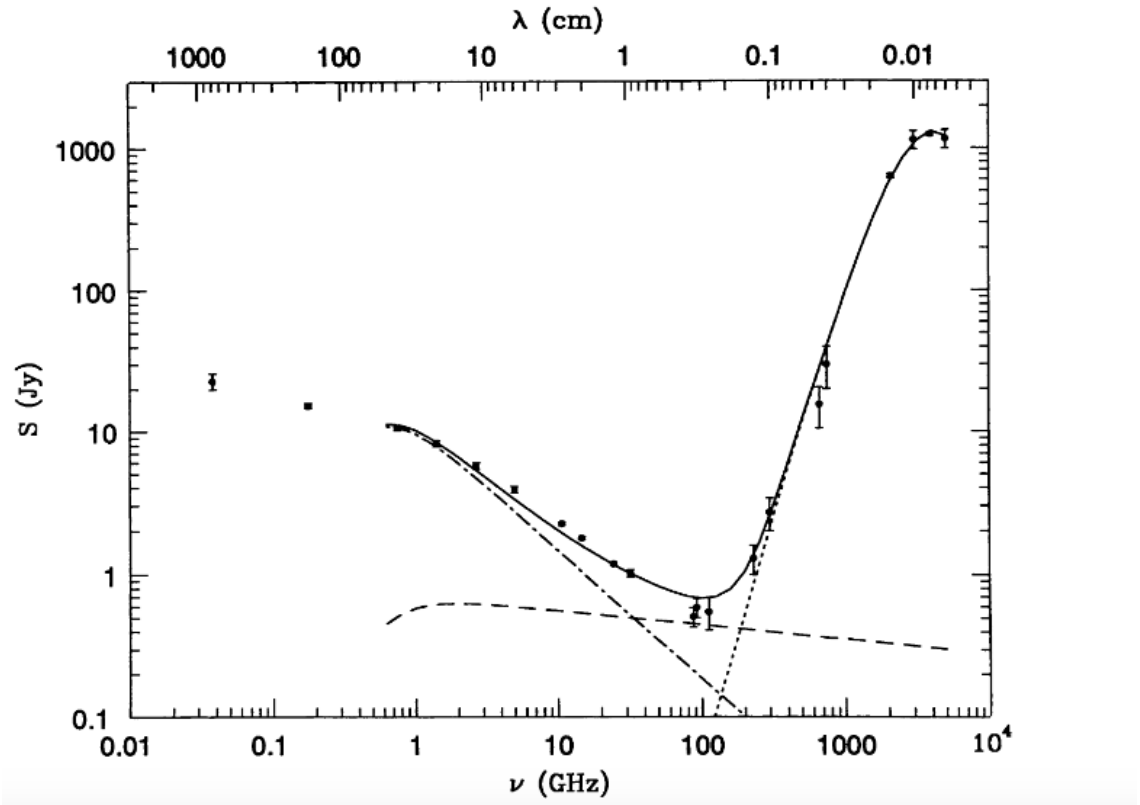

Figure 1.8: The radio, far-IR spectrum of M82. Black dots are measurements from Klein et al. (1988) and Carlstrom and Kronberg (1991). The solid line shows the total SED of the galaxy, while the synchrotron and free-free components are represented by the dot-dash and dashed lines, respectively. From: Condon (1992).

neither of these techniques are highly robust and feasible to carry out in most observations, instead of separating the two components, they are typically used together to calculate SFRs.

Historically, non-AGN related radio emission was generally possible to observe in dusty, high-mass galaxies due to relatively shallow radio (and IR) data. Thus, the observed infrared-radio correlation (IRRC; see e.g. van der Kruit, 1971, 1973; de Jong et al., 1985; Helou et al., 1985; Condon, 1992; Yun et al., 2001) provides the most commonly used radio flux – SFR calibration. The IRRC is thought to emerge due to IR and radio emission being linked to star formation, as outlined above (also known as the calorimeter theory first proposed by Voelk, 1989). However, its unity slope across several orders of magnitudes in luminosity is at odds with this naive model. For example, in low stellar mass galaxies it is expected that not all CR electrons lose their initial energy in galactic magnetic fields, a non-negligible fraction of them should escape to the IGM. Meanwhile, the fraction of UV radiation re-emitted at IR wavelengths is decreasing towards lower masses as well (see Fig. 1.6). These could lead to a deviation from the unity slope at low luminosities, but there is no strong evidence for this behaviour yet. Lacki et al. (2010) suggested that the effects cancel each other out, i.e. radio and IR fluxes underestimate star formation the same way towards lower masses.

Other techniques exist as well, that relate radio emission to star formation without the use of IR emission. High-resolution radio images can reveal radiation from supernova remnants directly, allowing supernova rate counts to be made visually (e.g. in Pérez-Torres et al., 2009). These are linked to SFR through a choice of IMF. Tabatabaei et al. (2017) calibrated the 1 – 10 GHz integrated radio luminosity as a SFR tracer. A comparison to other star formation proxies is also possible (e.g. Davies et al., 2017).

The main advantage of radio over other star formation proxies is that it is unaffected by dust attenuation, and therefore capable of consistently measuring SFRs in a wide range of different star-forming galaxies. The relative simplicity of the radio spectrum allows observationally less expensive, single band measurements to be SFR estimators. Moreover, with radio interferometry, radio observations can achieve high, sub-arcsecond resolutions routinely, matching e.g. optical data. Its drawback that it is, like many other SFR tracers, can be highly contaminated by AGN radiation, and until recently it has not been able to probe a large redshift range due to lacking depth. However, with a new generation of radio telescopes, such as the Square Kilometre Array and its precursors, MeerKAT and ASKAP, (Johnston et al., 2008), we will be able to push redshifts limits of radio surveys significantly further.

1.2.2 Tracing AGN activity

As discussed in Sect. 1.1.2, AGN produce significant amounts of non-stellar radiation at all wavelengths. In this section I will describe some approaches I used in my projects to identify AGN host galaxies.

One of the most reliable methods of finding AGN activity in a galaxy is investigating ionizing radiation properties using Baldwin–Phillips–Terlevich (BPT) diagrams (Baldwin et al., 1981). This diagnostic diagram compares certain emission line ratios (typically [N II]/H_α versus [O III]/H_β) to find the main ionizing mechanism. With better data and progress in theory, there have been new, more refined calibrations since the original work that offer a more varied classification of AGN, such as Seyferts, composite objects, etc. (such as Kewley et al., 2006, using SDSS spectra). The drawback of this technique is that it is observationally costly to detect all lines with sufficiently high signal-to-noise ratios (and indeed it can be even impossible in dust obscured AGN), and thus it is also harder to obtain at higher redshifts than some other diagnostics.

Hot gas in the accretion disk around a SMBH emits X-ray photons. In fact, most of the X-ray flux associated with galaxies is due to AGN activity, and the bulk of the individually detected X-ray galaxies harbour AGN. Therefore an X-ray luminosity selection can robustly identify AGN (e.g. Szokoly et al., 2004).

As mentioned in Sect. 1.1.2, dust torus around the SMBH can absorb large amounts of AGN-related radiation. This gas is warmer, than the galactic dust content associated with GMCs and star formation. Such radiation can be identified via SED modelling, when a good fit can only be obtained after adding a warm AGN-heated dust component. A simpler approach, which traces the same process, is selecting AGN based on mid-IR colours (Donley et al., 2012). In the most luminous QSOs significant far-IR emission can also arise due to AGN heating in more distant dust (Symeonidis et al., 2016).

Finally, synchrotron radiation at radio frequencies is produced by electrons accelerated in AGN-related magnetic fields. These radio loud AGN can be found as outlier sources with radio excess relative to the IRRC (e.g. Donley et al., 2005; Norris et al., 2006; Del Moro et al., 2013). Radio jets can extend to Mpc scales and often are visually very distinct (see e.g. Fig. 1.3), thus their morphological identification is also possible. This requires high-resolution imaging, which at radio wavelengths is only possible via interferometry, as discussed in Sect. 1.3.2.

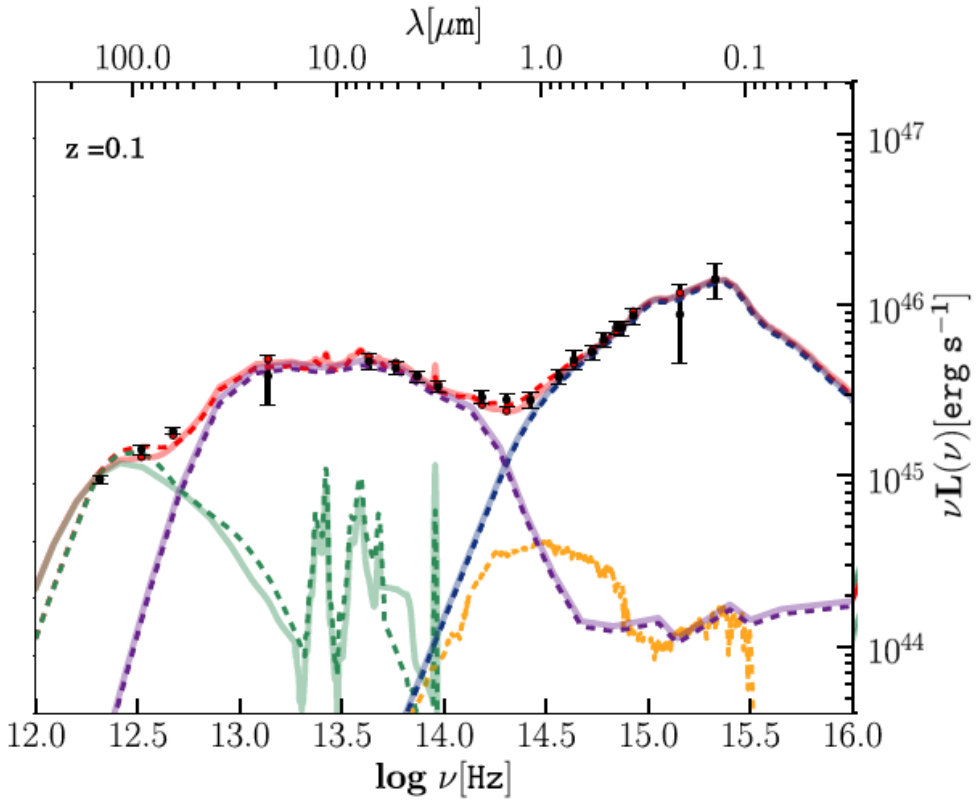

Figure 1.9: A typical AGN host galaxy's SED. Green curve shows the cold, host galaxy dust component, purple line is the warm AGN dust torus emission, yellow the stellar radiation, blue is the energetic thermal radiation from the material being accreted onto the central SMBH, while red represents the total SED. AGN-related components clearly outshines the stellar and cold dust ones below 100 μm. From: Calistro Rivera et al. (2016).

1.3 Radio astronomy

The research presented in this thesis has been underpinned by $\sim 1-6$ GHz radio continuum data. Non-thermal radio emission is the dominant radio component at this frequency range (Condon, 1992), thus, in this section, I will discuss its emission mechanism; the basics of interferometric imaging, a technique that can produce high-resolution images at these wavelengths; and finally relevant survey data. Sects. 1.3.1 and 1.3.2 are based on Wilson et al. (2009).

1.3.1 Synchrotron radiation

As mentioned in Sect. 1.2.1, the bulk of radio emission at ≤ 10 GHz originates from relativistic CR electrons. These are usually accelerated in supernova explosions or in AGN-driven jets. A relativistic electron with a velocity of $\vec{v}$ passing through a volume of space with magnetic field, $\vec{B}$, experiences the $\vec{v}\times\vec{B}$ Lorentz force. As a result, it will move in a helical orbit around the field lines and consequently emit EM radiation. It can be shown, that the spectral power of this emission, $P(\nu)$, from a single relativistic electron at the frequency of ν is

$$P(\nu) = \sqrt{3}\frac{e^3|\vec{B}|\sin(\theta)}{mc^2}\frac{\nu}{\nu_c}\int_{\nu/\nu_c}^{\infty} K_{5/3}(\eta)\mathrm{d}\eta, \tag{1.5}$$

where e is the elementary charge, θ is the electron's pitch angle, i.e. the angle between the particle's velocity vector and the local magnetic field, m is the electron's mass, c the speed of light, $K_{5/3}$ is the modified Bessel of 5/3 order. It is apparent that virtually no power is emitted above ν_c, given by

$$\nu_c = \frac{3}{4\pi}\gamma^2\omega_G\sin(\theta), \tag{1.6}$$

where $\gamma = \sqrt{1-v/c}^{-1}$ is the Lorentz factor and ω_G is the non-relativistic gyro-frequency. In a galaxy, synchrotron radiation arises from an ensemble of electrons with different energies. In general the resulting spectral emissivity, $\epsilon(\nu)$, is

$$\epsilon(\nu) = \int_E P(\nu, E)N(E)\mathrm{d}E, \tag{1.7}$$

where $P(\nu, E)$ is the total power emitted by a single electron with energy E at ν frequency (as in Eq. 1.5) and $N(E)\mathrm{d}E$ is the number of electrons per unit volume and unit solid angle moving towards the observer with energies between E and $E + \mathrm{d}E$. We can assume that their pitch angle distribution is homogeneous and isotropic. Empirically $N(E)$ is then well approximated by a power law of spectral index δ and normalization K, between energies E_1 and E_2:

$$N(E)\mathrm{d}E = KE^{-\delta}\mathrm{d}E \quad \text{for} \quad E_1 < E < E_2 \tag{1.8}$$

Let us substitute Eqs. 1.5 and 1.8 into Eq. 1.7 and integrate from E_1 to E_2. If we define

$$\alpha \equiv \frac{1}{2}(\delta - 1), \quad \mu \equiv \frac{3}{4\pi}\frac{e|\vec{B}|\sin(\theta)}{m^3c^5}, \quad x \equiv \frac{\nu}{\mu E^2} \tag{1.9}$$

the solution can be written as

$$\epsilon(\nu) \propto \nu^{-n}[Q(n, \nu/\nu_1) - Q(n, \nu/\nu_2)], \tag{1.10}$$

where

$$Q(n, \nu/\nu_c) = \int_{\nu/\nu_c}^{\infty} x^{\alpha-1}F(x)dx. \quad \text{and} \quad F(x) = x\int_x^{\infty} K_{5/3}(t)dt \tag{1.11}$$

For $\nu/\nu_2 \ll x \ll \nu/\nu_1$ (where $\nu_{1,2} = \mu E_{1,2}$) Q is frequency independent, thus

$$\epsilon \propto \nu^{-\alpha}. \tag{1.12}$$

The most important result here, is that a power law distribution of synchrotron emitting electrons gives rise to photon spectrum described by another power law, whose spectral slope is linked to the slope of electron population's energy distribution, as given in Eq. 1.9. Since more energetic electrons lose energy faster, δ, and as a consequence α steepens, thus a relatively flatter slope is the result of a younger underlying electron population. This observation will be important in interpreting synchrotron spectral slope changes in my work presented in Chapter 2.

1.3.2 Radio interferometry

The angular resolution of a telescope, θ, in units of radian is

$$\theta \approx \frac{\lambda}{D}, \tag{1.13}$$

where λ is the observed wavelength and D the telescope's diameter. This means, that in order to achieve a ~ 1 arcsecond resolution at centimetre wavelengths that matches typical optical images, we would need an order of kilometre sized dish, which is technically infeasible. To circumvent this problem, interferometry was invented (first used by Ryle and Vonberg, 1946). The basic idea of these interferometric observations is to combine signals from multiple telescopes and by doing so, mimic a larger aperture. The resulting image will have an angular resolution similar to a telescope

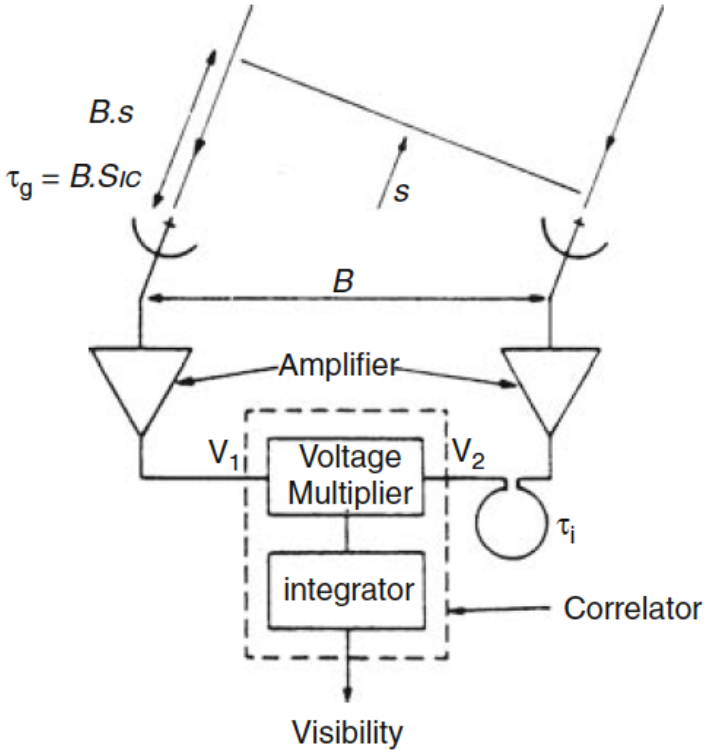

Figure 1.10: Schematics of a two-element radio interferometer. From: Wilson et al. (2009).

with a diameter that equals the distance between the two most distant elements in the telescope array. In the this section I will discuss the basic concepts of interferometric imaging.

The simplest configuration for an interferometric measurement uses two telescopes, as Fig. 1.10 schematically shows. The two antennas at a distance of $\vec{B}$ to each other (also referred to as the 'baseline') observe a source in the sky towards $\vec{s}$. Due to the geometry of the set-up, the left side receiver detects the incident EM wave from the source later than the right by a time delay, τ:

$$\tau = \frac{\vec{B} \cdot \vec{s}}{c} \tag{1.14}$$

where c is the speed of light. The two signals measured at the right and left antennas thus induce voltages proportional of the observed EM wave's amplitude

$$U_1 \propto E e^{i\omega t} \tag{1.15}$$

and

$$U_2 \propto E e^{i\omega(t-\tau)}, \tag{1.16}$$

respectively. These outputs are then amplified and correlated – the correlator device multiplies and integrates the signals over a given T time period. If $T \gg 2\pi/\omega$, the result of the integration

approximately equals an integration over one wave oscillation period. The $R(\tau)$ response is then:

$$R(\tau) \propto \frac{1}{2} E^2 e^{i\omega\tau}. \tag{1.17}$$

If the radio brightness distribution in the sky at frequency ν is $I_\nu(\vec{s})$ from source element $\mathrm{d}\Omega$ in a small bandwidth $\mathrm{d}\nu$, and both antennas have the same power pattern $A(\vec{s})$, the total response, $R(\vec{B})$, is calculated by integrating over the source:

$$R(\vec{B}) = \iint_\Omega A(\vec{s}) I_\nu(\vec{s}) \exp\left[i2\pi\nu \left(\frac{\vec{B}\cdot\vec{s}}{c} \right) \right] \mathrm{d}\Omega\mathrm{d}\nu. \tag{1.18}$$

$R(\vec{B})$ is called the visibility function. To solve Eq. 1.18 for $I_\nu(\vec{s})$, and thus reconstruct the intensity distribution from the observed visibility, it is useful to find a convenient coordinate system for $\vec{B}$ and $\vec{s}$. It can be shown that Eq. 1.18 can be transformed into

$$V(u,v) = \int_{-\infty}^{\infty}\int_{-\infty}^{\infty} A(x,y) I(x,y) e^{i2\pi(ux+vy)} \mathrm{d}x\mathrm{d}y, \tag{1.19}$$

where x and y are coordinates in a plane tangential to the celestial sphere and u and v are coordinates in wavelength units. Eq. 1.19 closely resembles a 2D Fourier-transform, and indeed, if V were known at every u and v points, the measured visibility could be easily used to calculate $I(x,y)$ by an inverse Fourier transform of $V(u,v)$. In general, methods seeking to restore $I(x,y)$ from $V(u,v)$ measurements are called aperture synthesis.

However, since realistically we have a finite number of antennas, at a fixed source elevation the number of observable baselines (i.e. $V(u,v)$ samples) are limited by our telescope array. Thanks to Earth's rotation, the orientation of the baselines with respect to the source change with time, allowing a better visibility coverage. Nevertheless, the (u,v) plane is not fully known. If we neglect $A(x,y)$ antenna response, and carry out the inverse Fourier-transform, this can be expressed as

$$I_D(x,y) = \iint S(u,v) V(u,v) e^{i2\pi(ux+vy)} \mathrm{d}u\mathrm{d}v, \tag{1.20}$$

where $I_D(x,y)$ is the "dirty image" and $S(u,v)$ is the sampling function. $S(u,v)$ is 1 in the points of the (u,v) plane where we have measurements, and 0 everywhere else. The dirty image has several shortcomings: it often contains large negative features and other imaging artefacts, and is unstable in the sense that it can change significantly with new $V(u,v)$ data added. These are results of the obviously wrong assumption that $V(u,v) = 0$ where it is not measured. With the convolution theorem we can re-write Eq. 1.20 as:

$$I_D(x,y) = I(x,y) \circledast B, \tag{1.21}$$

where B is the "dirty beam":

$$B(x, y) = \iint S(u, v) e^{2\pi i(ux+vy)} \mathrm{d}u\mathrm{d}v. \tag{1.22}$$

Thus finding the "true" image $I(x, y)$ became a deconvolution problem. It is important to note, that due to our finite number of sampling points in the (u, v) plane, emission on large spatial scales (dependent on the length of the shortest baseline, $d_{\min}$ as $\lambda/d_{\min}$) are inherently not in the visibility data, and cannot be detected in any way regardless of the imaging approach used. In interferometric jargon these flux components are "out-resolved".

In practice, I_D from Eq. 1.20 is calculated using a discrete Fourier transform:

$$I_D(x, y) = \sum_k g(u_k, v_k) V(u_k, v_k) e^{-i2\pi(u_k x + v_k y)}, \tag{1.23}$$

where $g(u, v)$ is an arbitrary weighting function. The choice of $g(u, v)$ influences the resulting image's sensitivity and resolution. Two extreme weighting functions are the natural and the uniform. Natural weighting means inverse weighting with noise variance, which increases sensitivity. However, as a result of (u, v) plane gridding, this typically favours short baselines, and thus degrades angular resolution. On the other hand, uniform weighting sets $g(u_k, v_k) = 1$, leading to a better resolution but poorer signal-to-noise. The most common weighting scheme is the robust weighting (Briggs, 1995). It uses a manually set threshold value, thus allows the user to find the desired balance of resolution and sensitivity best suited for the problem at hand.

To improve the dirty image, we have to model $V(u, v)$ outside the sampling function $S(u, v)$. The most common deconvolution technique is CLEAN, which assumes that sky intensity is built from the sum of point sources with positive amplitude (method first suggested by Högbom, 1974). It is an iterative method, that gradually builds an intensity distribution model in order to deconvolve the dirty beam from the true image. As the first step, it finds the maximum on the dirty image, subtracts a small fraction of it (typically $\sim$ 10 %) at the position of the peak as a point source convolved with the dirty beam. This point source is added to a model image. In the next step it finds the maximum on the residual of the dirty image, and moves a fraction of that flux to the model, until the residual is below a certain threshold (usually set to be the a priori expected noise level) or the cycle reaches a given number of steps. The cleaned image is then taken as the model image convolved with the synthesised or clean beam (a Gaussian with $\sim$ the full width half power of the dirty beam), plus the residual image from CLEAN. Since its first implementation, Clark (1980) and Schwab (1984) further optimised the process by shifting some computations to the (u, v) plane. Multi-scale multi-frequency CLEAN relaxes the point source assumption by allowing models spatially smoothed, larger scales and combines it with wideband modelling (Rau and Cornwell,

2011).

An alternative way of modelling $V(u, v)$ is called the Maximum Entropy Deconvolution Method (MEM; e.g. Cornwell and Evans, 1985). It assumes that the smoothest map consistent with the data is the most likely solution, and finds it by maximizing a quantity called entropy. MEM is considered to perform better with mosaics, and images with low surface brightness, extended features, while CLEAN is better at recovering point sources, and is generally the more widely used technique. I produced the images shown in Chapter 2 with CLEAN, and the survey data in Chapters 3 and 4 (described in more detail in the following section) were also imaged with it.

1.3.3 Current and future radio interferometric surveys

In this section I will first describe the radio survey data used in this thesis, then give an overview on upcoming radio wavelength data.

A major undertaking of the 90s at radio frequencies was the NRAO VLA Sky Survey (NVSS; Condon et al., 1998). It mapped the entire northern sky ($\delta \geq -40^{\mathrm{deg}}$) between 1993 and 1997 at 1.4 GHz. It detected $\sim$ 2 million sources across 82 % of the celestial sphere with a lower flux limit of $\sim$ 2.5 mJy. It was carried out using a compact array configuration to minimize the likelihood of resolving out extended flux components, however, at the cost of a low, 45 arcsecond angular resolution. Faint Images of the Radio Sky at Twenty-centimeters (FIRST; Helfand et al., 2015) was also observed with VLA. It surveyed an area roughly coincident with the Sloan Digital Sky Survey's (SDSS) coverage between 1993 and 2011, also at 1.4 GHz. It used a more extended array configuration, hence its lower, 5 arcsecond beam size. FIRST achieved, on average, a 1 mJy detection sensitivity, and found $\sim$ 1 million radio sources. These data were used for the work presented in Chapter 4. Finally, the project described in Chapter 3 was, in part, based on observations from the VLA-COSMOS 3 GHz Large Project (Smolčić et al., 2017b). It is a so-called pencil beam survey, which unlike the large NVSS and FIRST, only targeted the small, 2 square degree Cosmic Evolution Survey (COSMOS) field (Scoville et al., 2007), but with a very high sensitivity of $\sim$ 2.3 μJy beam^{-1} and significantly better, 0.75 arcsecond resolution. Several future radio surveys discussed below aim to do both type of observations together in order to create multi-tiered, "wedding-cake" style datasets.

Radio interferometry is on the brink of a new era. The recently upgraded Very Large Array (VLA) is currently mapping the northern sky at 2–4 GHz (VLA Sky Survey, VLASS) $\sim$ 10 times deeper than the previously deepest northern radio sky survey, FIRST. There are already plans to expand the Karl G. Jansky Very Large Array (JVLA) into the next-generation VLA (ngVLA; Murphy et al., 2017) that would rival SKA on the northern hemisphere. Such an instrument

e.g. could revolutionize our understanding of AGN feedback (Nyland et al., 2018). Meanwhile, the LOw-Frequency ARray (LOFAR; van Haarlem et al., 2013) has been increasingly successful probing the 10–240 MHz frequency regime. It provided data to measure the low frequency curvature of galactic radio SEDs (Calistro Rivera et al., 2017), gave a new SFR calibration at long wavelengths (Gürkan et al., 2018), put constraints on the early Universe HI intensity mapping signal (Patil et al., 2017), etc. With an ever expanding array across Europe, it will continue charting the low frequency radio regime for years to come. MeerKAT, a pathfinder instrument to SKA, will come on-line later this year. Its unprecedented survey speed and sensitivity will enable large volumes of the Universe to be probed both in wide fields, such as the MeerKAT Large Area Synoptic Survey (MeerKLASS; Santos et al., 2017), and deep fields with smaller area (MeerKAT International GHz Tiered Extragalactic Exploration – MIGHTEE; Jarvis et al., 2017) down to μJy levels. These will find millions of radio sources, providing a more complete census of star forming and AGN sources than ever, detect 21cm HI emission at higher redshifts than it has been possible so far, and attempt to put new constraints of cosmology. With these new multi-frequency datasets it will be possible to probe the radio SED from low frequencies to wavelengths where dust radiation suppresses the thermal and non-thermal signals. Combined with shorter wavelength ancillary data it will be possible to separate these two components more robustly, study radio SED shapes as function of galaxy properties, investigate variations within galaxies, and overall better understand the physical process that regulate radio emission in both star-forming galaxies and AGN.

1.4 Summary

This chapter briefly introduced the basic concepts of galaxy evolution – ISM properties and star formation on small and large scales, AGN activity, and their possible connections via feedback. Since my thesis work has been observationally driven, I then presented some common measurement techniques that trace these processes. In particular, I focussed on radio frequency signatures of both star formation and AGN activity, since radio observations were at the centre of all my PhD work. I finally gave an overview of radio interferometric imaging.

The paper presented in Chapter 2 studies new radio interferometric observations of a QSO – starburst galaxy pair. The nature of this system had been a topic of debate in the past, and various exotic scenarios had been proposed to describe the observations. With the use of new radio data I tested whether QSO driven jets could have triggered the starburst in the companion galaxy.

My second paper shown in Chapter 3 investigates the IRRC's redshift evolution in spheroid- and disc-dominated star forming galaxies. Their different redshift trends gave an insight into the possible causes of the declining IR-radio ratio towards high redshift found in recent works and gave

important clues towards a more accurate radio – SFR calibration.

In Chapter 4 I present my current work on the $z < 0.2$ IRRC. I measure the IR-radio ratio in the largest-to-date sample in the low-z Universe, demonstrate selection effects and attempt to provide a new reference sample for radio – SFR calibrations and for future IRRC studies.

Chapter 5 is based on a project which I contributed to mainly by implementing the Bayesian model fitting approach I used for my work in Chapter 4. I modelled the physical properties of a double cloud core in the Auriga–California molecular cloud in the Milky Way using observations of ammonia spectra.

Finally, in Chapter 6 I summarize the main findings of the research I presented in this thesis and discuss future plans.

Chapter 2

Further evidence for a quasar-driven jet impacting its neighbour galaxy: the saga of HE0450–2958 continues

This paper was published in Molnár et al., 2017, Monthly Notices of the Royal Astronomical Society, Volume 467, Issue 1, p.586-596.

Co-authors are:

M. T. Sargent, D. Elbaz, P. P. Papadopoulos, J. Silk

Abstract

HE0450–2958, an interacting quasar–starburst galaxy pair at z = 0.285, is one of the best-known examples of strong star formation activity in the presence of a quasar-driven jet. We present new multiband Karl G. Jansky Very Large Array-imaging covering 1–6 GHz and reaching an angular resolution of up to 0.6 arcsec (a sixfold improvement over existing radio data). We confirm the previous detection of a spatially extended radio component around the quasar, indicating that there is ongoing star formation activity in the quasar host galaxy. For the first time, we directly detect a jet-like bipolar outflow from the quasar aligned with its companion star-forming galaxy (SFG) and several blobs of ionized gas in its vicinity identified in previous studies. Within the companion SFG, we find evidence for a flattening of the synchrotron spectral index towards the point of intersection with the jet axis, further suggesting that the outflow may actually be impacting its interstellar medium. We discuss two possible mechanisms that could have triggered the starburst in the companion SFG: a wet–dry merger with the quasar and jet-induced star formation. While triggering through interaction-driven gas dynamics cannot be excluded with current data, our new observations make HE0450–2958 a strong candidate for jet-induced star formation, and one of the rare links between local systems (like Minkowski's Object or Centaurus A) and the high-z regime where

radio-optical alignments suggest that this phenomenon could be more common.

2.1 Introduction

Observations show that the mass of the central supermassive black hole of local galaxies correlates with their bulge luminosity (Kormendy and Richstone, 1995; Magorrian et al., 1998), bulge mass (Kormendy and Gebhardt, 2001; McLure and Dunlop, 2001, 2002; Marconi and Hunt, 2003; Ferrarese et al., 2006) and velocity dispersion (Ferrarese and Merritt, 2000; Gebhardt et al., 2000). How these scaling relations are established is not well understood. It could simply be the outcome of stochastic growth through merging in a hierarchical universe (Peng, 2007; Jahnke and Macciò, 2011, e.g.), or the joint outcome of gas consumption by similar relative proportions for star formation (SF) and black hole growth (e.g. Mullaney et al., 2012). A further possibility is a causal connection, e.g. through feedback processes: current models describing galaxy formation and evolution tend to use various prescriptions for feedback from active galactic nuclei (AGNs) to match their predictions to observations (Silk and Mamon, 2012, and references therein), especially for high-mass galaxies. Therefore, studying the effects of AGN activity on its surroundings is one of the keys to understanding galaxy formation and evolution.

2.1.1 Negative and positive feedback

Feedback due to AGN activity is often used to explain quenching of SF in galaxies via radiation and mechanical feedback interacting with the interstellar medium (ISM) of the host galaxy and the intracluster gas surrounding it. Two modes of negative AGN feedback are commonly discussed in the literature: a radiative mode ('quasar' or 'cold' mode) for very luminous, fast-accreting AGN generating a radiation pressure that is capable of expelling gas from the host galaxy, and a kinetic mode ('radio' or 'hot' mode) whereby slowly accreting AGN drive jets and cocoons that heat intracluster gas and inhibit cooling and accretion on to the host galaxy from the circumgalactic medium. For a more in-depth review of the subject, see Fabian (2012) and references therein. Negative feedback is invoked to explain the origin of red and dead galaxies in the local Universe. However, even if quasars ultimately stop SF in galaxies, they may also act as a trigger at an earlier stage of their evolution, through positive feedback due to radio jets and turbulent pressure (Begelman and Cioffi, 1989; Silk, 2005, 2013; Silk and Norman, 2009; Nesvadba et al., 2011). Elbaz et al. (2009) have proposed that quasar-driven jets can play an active role in galaxy formation through positive feedback. The compact nature of nuclear starbursts, simulated in Gaibler et al. (2012), is comparable to that now being observed with ALMA, e.g. in Oteo et al. (2016) via extreme, Arp 220-like, SF densities. While there is no direct evidence for an AGN, and associated triggering of a circumnuclear disc (Oteo et al., 2017), the case for an AGN being required in the analogous case of Arp 220 was presented by Tunnard et al. (2015) from chemical evidence.

A promising candidate for observing both positive and negative feedback in action is HE0450–2958.

2.1.2 HE0450–2958 – a peculiar object with a history

HE0450–2958 is an optically bright quasar ($M_V = -25.8$) originally classified as a Seyfert I galaxy due to its far-infrared (FIR) colours (de Grijp et al., 1987) and its optical spectra (Merritt et al., 2006) at the redshift of z=0.285. Optical images with *Hubble Space Telescope (HST)* revealed a double system with the quasar and a companion star-forming galaxy (companion SFG) ~7 kpc projected separation (Magain et al., 2005, M05 henceforth), which is located at the same redshift as the quasar (within the observational uncertainties of the spectroscopy presented, e.g. in Letawe et al., 2008). After deconvolving the *HST* image, M05 also found an emission line 'blob' at the redshift of the quasar with small projected separation. M05 proposed that it is an AGN-ionized gas cloud; however, more recently, Letawe and Magain (2010) found near-IR continuum emission towards the source, suggesting that it is an off-centre, bright and very compact host galaxy.

HE0450–2958 spurred significant interest when M05 estimated the black hole mass for the quasar and reported an upper limit for the host galaxy luminosity that was five times fainter than that expected based on the Magorrian relation between black hole mass and bulge luminosity (Magorrian et al., 1998). The finding triggered a debate about the existence of so-called naked quasars, i.e. quasars without a host galaxy. This hypothesis is no longer strongly favoured in the case of HE0450–2958 following (a) publication of a revised black hole mass estimate by Merritt et al. (2006), which is 10 times lower than the one in M05, and (b) evidence of extended radio continuum emission from SF activity in the quasar host galaxy (Feain et al., 2007). However, the quasar is still not placed firmly on the Magorrian relation and the quasar host galaxy properties remain poorly known.

The second main component of the HE0450–2958 system, the companion SFG, has attracted attention in its own right. It was initially thought to be a ring galaxy (Boyce et al., 1996), but later M05 discovered that it hosts a highly dust-obscured central region that produces the ring-like appearance at optical wavelengths. Based on low-resolution radio continuum imaging, Feain et al. (2007) proposed that the quasar and the companion SFG are bridged together by a radio jet (as seen in Fig. 2.1) that was suggested to induce the intense SF (~340 $M_\odot$ yr^{-1}; Elbaz et al., 2009) in the companion SFG and turn it into an ultraluminous infrared galaxy (ULIRG; Elbaz et al., 2009). However, due to the poor angular resolution (~ 3 arcsec or 13 kpc at the distance of HE0450–2958, see Table 2.1) of the *Australia Telescope Compact Array (ATCA)* imaging, they could provide only indirect evidence with the detection of the opposite lobe. The presumed interacting outflow component remained undetected, since it was blended with emission from the companion SFG. Following this study, Elbaz et al. (2009) suggested that HE0450–2958 may represent an early phase in a scenario of 'quasar-induced galaxy formation'. While it has been debated whether the active SF in the companion is due

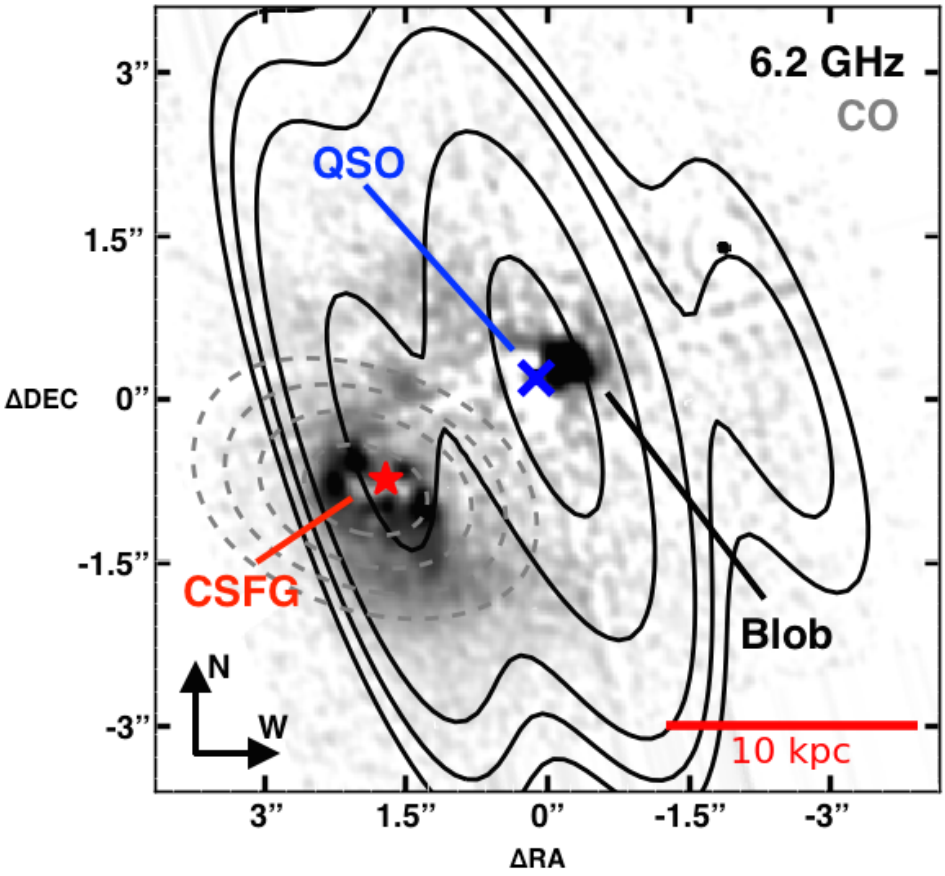

Figure 2.1: PSF-deconvolved HST optical image of HE0450–2958 from M05. The red star and the blue cross show the positions of the companion SFG (CSFG) and quasar (QSO), respectively. An emission line 'Blob' is visible directly to the west of the quasar. The black contours show the triple-component 6.2 GHz radio flux distribution measured with the ATCA (Feain et al. 2007; contour levels are 5, 7, 10, 20 and 35 σ **, where** σ = 0.04 **mJy beam**$^{-1}$**). The synthesised beam size of these 6.2 GHz ATCA continuum observations is 5.68 arcsec** $\times$ **1.95 arcsec.** Grey dashed contours represent the CO J = 1-0 line detection averaged over 570 km s^{-1}, obtained with *ATCA* by Papadopoulos et al. (2008, contour levels are 7, 9, 11 and 13 σ, where σ = 0.45 mJy beam^{-1}). The synthesised beam size of this observation is 3.21 arcsec $\times$ 2.14 arcsec. See text of Sect. 2.1.2 for further discussion.

to a merger event between the two objects or actual jet-induced SF – as found in other systems such as Minkowski's Object (Croft et al., 2006) – high excitation optical lines have been found in the companion with hints of shock-induced origins, suggesting that its gas was undergoing collision (Letawe et al., 2008). Meanwhile, Papadopoulos et al. (2008) found molecular gas associated mainly with the companion SFG, not the quasar, suggesting that the AGN could provide negative feedback for its own host galaxy. This makes HE0450–2958 an example highlighting the full diversity of AGN feedback-related phenomena in one system (similar to e.g. Cresci et al., 2015).

In these papers, various scenarios were proposed to explain the observations, e.g. a merger of the massive companion SFG and a dwarf elliptical with an AGN (Papadopoulos et al., 2008), quasar-jet-induced SF in the companion SFG (Elbaz et al., 2009) or a highly asymmetric host with an offset active nucleus (Letawe and Magain, 2010). Our new radio observations mainly aim to test the quasar-induced large-scale SF hypothesis.

Throughout this chapter, we use a flat ΛCDM cosmology with $\Omega_M = 0.31$ and $H_0 = 67.77\,\mathrm{km\,Mpc^{-1}\,s^{-1}}$ (Planck Collaboration et al., 2014). Star formation rates and stellar mass values reported assume a Salpeter initial mass function (IMF).

2.2 Observations and data reduction

2.2.1 Observations

We observed HE0450–2958 on 2011 September 3 and 2012 September 11 (project codes 10C-123 and 12B-192, respectively; PI: Sargent) with the Karl G. Jansky Very Large Array (JVLA) in the L and C bands using 26 antennas. Three setups were chosen to achieve distinct science goals.

1. Simultaneous A-array observations in two C-band spectral windows centred at 4 and 6 GHz produced high-resolution images probing the small-scale structure of the GHz radio emission from the HE0450–2958 system. With an average angular resolution of 0.37 arcsec × 0.93 arcsec, these images allow us (a) to identify the eastern lobe of a potentially bipolar outflow from the quasar by spatially separating it from the emission from the companion SFG (see Section 2.3.2) and (b) to study variations of the radio spectral index within the companion SFG (see Section 2.3.3).

2. A-array imaging at 1.8 GHz (angular resolution 0.84 arcsec × 2.64 arcsec) can, for the first time, resolve the three main radio components of the HE0450–2958 system and determine their spectral properties using our higher frequency observations. When combined with the *ATCA* X-band data from Feain et al. (2007), our L- and C-band data sample the radio spectral index of HE0450–2958 in approximately every 2 GHz between 1.8 and 8.6 GHz (i.e. a total frequency baseline of 6.8 GHz).

3. Using the full 1-GHz frequency coverage of the L-band receivers in the more compact

BnA configuration and a long integration time, we obtained lower resolution (3.52 arcsec × 2.71 arcsec) but high-sensitivity images to search for faint synchrotron emission from, e.g. ionized region produced by quasar jet wobbling or displaying SF activity triggered by the quasar jet (see discussion in Elbaz et al., 2009).

Integration times (see Table 1 2.1) were based on the total fluxes of the currently known radio components associated with HE0450–2958, as measured by Feain et al. (2007) with *ATCA*. Feain et al. (2007) achieved detections at an $8\,\sigma$ (C-band, 6.2 GHz) and $6\,\sigma$ (X-band, 8.6 GHz) significance level with ATCA. The targeted sensitivity and angular resolution of our observations were chosen to significantly improve the imaging quality by achieving S/N $\sim$ 10 in each resolution element on the faintest of the previously observed radio components associated with HE0450–2958, i.e. the western lobe (the opposite lobe of a putative bipolar outflow that has been suggested to have triggered SF in the companion SFG).

Our BnA-configuration L-band follow-up involved 72 min of on-source observations with 1 s integrations. 16 spectral windows with 64 channels each were used to cover the entire L band from 1 to 2 GHz. All data from antenna 10 had to be flagged during these wideband observations due to its L-band receiver being removed for repairs. The total available bandwidth during the L- and C-band observations in configuration A was limited due to the JVLA being in the VLA to EVLA transition phase at the time of observation. The L-band observations in configuration A used a total bandwidth of 256 MHz with 2-MHz frequency resolution centred at 1.8 GHz to avoid the regions most affected by strong radio frequency interference (RFI) and to maximize the angular resolution achievable in the L-band. The total integration time of these observations was 21 min with 1 s integration intervals. For our C-band observations, the correlator was configured to deliver two spectral windows centred at 4036 and 5936 MHz, each providing 64 × 2 MHz channels for a total bandwidth of 256 MHz. In this setup, we observed the source for 108 min also with 1 s integration intervals.

During each scheduling block (SB), we followed the same

2.2.2 Calibration

Flagging of bad data and calibration were done using standard procedures as implemented in the VLA Calibration pipeline[1] in CASA[2]. Hanning smoothing[3] was applied to all data to ensure a more effective detection and removal of RFI. For the more strongly affected L-band data, the reliability of the pipeline's automatic RFI flagging with the RFLAG task was tested in several spectral windows on phase/bandpass and flux calibrator data by comparison to manually flagged data. Thirty-eight per cent of the visibilities at 1.5 GHz, ~ 22 per cent of those at 1.8

[1] https://science.nrao.edu/facilities/vla/data-processing/pipeline

[2] Common Astronomy Software Applications: http://casa.nrao.edu

[3] Hanning smoothing is a running mean across the spectral axis with a triangle smoothing kernel. It significantly reduces the effects of ringing arising from strong spectral line sources (such as RFI), while it reduces spectral resolution by a factor of two.

Observation	Frequency (GHz)	resolution (arcsec×arcsec)	PA (deg)	σ_{rms} (μJy beam^{-1})	on-source time (min)
JVLA BnA array	1.5 GHz	3.52×2.71	-54	16	72
JVLA A array	1.8 GHz	0.84×2.64	16	32	21
JVLA A array	5 GHz	0.93×0.37	-3	11	108
ATCA	6.2 GHz	5.68×1.95	16.1	40	-
ATCA	8.6 GHz	4.07×1.25	14.9	50	-

Table 2.1: Summary of JVLA observations and image properties (lines 1–3), and of HE0450–2958 *ATCA* data obtained by Feain et al. 2007. Image noise was measured in emission-free regions near the phase centre. The resolution column provides the FWHM of the semi-major and semi-minor axis of the restoring beam. Restoring beam position angles (PA) are measured counter-clockwise from the positive y-axis.

GHz and ~ 17 per cent of the visibilities in the C-band, were flagged. After calibration, all antenna-based amplitude and phase solutions were inspected and found to be satisfactory. The flux calibrator (3C 48) was imaged in each band and its flux density measured to be within 6 per cent (1.5 GHz), 6 per cent (1.8 GHz), and 10 per cent (5 GHz) of the accepted values.

2.2.3 Imaging

Imaging was carried out in CASA using the CLEAN task in multiscale multifrequency synthesis mode (MS-MFS; Rau and Cornwell, 2011) and Briggs weighting with a robust parameter of 0.5. When combining the two spectral windows centred at 4 and 6 GHz in the C band, we were able to model the frequency dependence of visibilities (*nterms* = 2 in the MS-MFS mode), resulting in a spatially resolved spectral index map additional to the standard full Stokes intensity map at 5 GHz. The rms noise was measured using CLEAN's IMSTAT task in multiple regions close to the image centre covering several independent beams. We reach 1 σ sensitivities of 32 μJy beam^{-1} on the 1.8 GHz narrow-band image (expected[4]: 32 μJy beam^{-1}), 16 μJy beam^{-1} on the 1.5-GHz wideband image (expected: 10 μJy beam^{-1}) and 11 μJy beam^{-1} on the 5-GHz image (expected: 10 μJy beam^{-1}). Image noise and synthesized beam properties are summarized for all three of our observational setups in Table 2.1, while Fig. 2.2 shows the final images.

[4]estimated by the online VLA Exposure Calculator (https://obs.vla.nrao.edu/ect/). Note that for the low-resolution L-band image, where noise deviates most from the targeted values, phase-only self-calibration did not lead to any improvement of noise and image quality.

2.3 Results

Previous centimetre continuum observations by Feain et al. (2007) at 6.2 and 8.6 GHz found evidence of a triple radio structure around HE0450–2958. The most westerly component, called 'C3' by Feain et al. (2007), could not be matched with any known extragalactic source (down to an optical limit of $\sim$26.5 m_V in M05). It is believed to be the synchrotron lobe of an outflow emanating from the quasar, which coincides with the central of the three radio components. The easternmost is associated with the companion SFG and, based on its elongation, is thought to include a contribution from a second, quasar-driven outflow facing in the opposite direction from C3. Our observations extend the *ATCA* observations by Feain et al. (2007) to longer wavelengths and significantly improve them, both in terms of sensitivity (fourfold) and angular resolution (sixfold) in the C-band (see Table 2.1). Due to their higher angular resolution, our data permit us to map the total extent of the jet and determine the distribution of the synchrotron emission inside the companion SFG and the quasar. With increased sensitivity, we can detect faint substructure in the vicinity of the quasar and companion SFG and identify faint outflow components. Our multiband and higher sensitivity data probe the synchrotron spectrum of the components over a larger range of frequencies, leading to an improved characterization of their spectral shape/index.

Fluxes for the three main emission components were measured interactively with the 2D elliptical Gaussian fitting algorithm included in the CASA Viewer Tool.We also used the CASA task UVMODELFIT with initial estimates based on image plane fit results to fit these data with single-component 2D Gaussian model in *uv* space. Both methods yielded highly consistent fluxes and shapes for the quasar, which was later checked by visually inspecting residual images as well. The companion SFG could not be fitted in the uv plane due to the relative strength of the surrounding, blended emission, so we used only the central, uncontaminated part of the emission to fit it in the image plane. At 5 GHz (1.8 GHz), we detected the quasar with S/N = 158 (173), the SFG companion with S/N = 93 (86) and the western lobe with S/N = 41 (42). Throughout the paper, we consider sources resolved if their intrinsic source sizes after deconvolution with the restoring beam are not consistent with zero based on source size errors returned by the CASA tasks IMFIT and UVMODELFIT. Using this criterion, both the quasar and the SFG companion were resolved on both C-band images along both principle axes of the synthesized beam (for derived physical sizes, fluxes and spectral indices, see Table 2.2).

Subtracting these high-S/N sources from the 5-GHz[5] image reveals several weaker, but still significant patches of emission around the quasar and the SFG companion. The morphology is not well described by 2D elliptical Gaussians; hence, their fluxes were measured using elliptical apertures and CASA's IMSTAT task. Errors for these more irregular emission features were estimated by sampling several emission-free regions with the equally sized apertures and

[5]The overall C-band flux measurements arising from the combination of the two spectral windows at 4 & 6 GHz.

calculating the standard deviation of the fluxes measured in these empty apertures. Their S/N values range from 4 to 10.

2.3.1 Single power-law synchrotron spectra

With our imaging at 1.8, 4 and 6 GHz, we are able to characterize individually the synchrotron spectrum of the quasar and its star-forming companion SFG over a frequency baseline of 4.2 GHz (6.8 GHz including the ATCA X-band flux measurements by Feain et al. (2007) at 8.6 GHz). The JVLA images at these three frequencies have a different angular resolution (2.6 arcsec × 0.8 arcsec at 1.8 GHz, 1.2 arcsec × 0.4 arcsec at 4 GHz and 0.7 arcsec × 0.3 arcsec at 6 GHz). For a consistent measurement of the spectral index, we have re-imaged the higher frequency data with the restoring beam of the lowest resolution image at 1.8 GHz. We then remeasured integrated fluxes for the three main components of the HE0450–2958 system and calculated the spectral index α defined as

$$S_\nu \propto \nu^\alpha, \tag{2.1}$$

where S_ν is the flux density at frequency ν.

Fig. 2.3. shows the synchrotron spectrum of the three main radio components of HE0450–2958 (see Fig. 2.4) and their fitted spectral slopes. These are highly consistent with the ones derived by Feain et al. (2007, see Table 2.2); -1.0 ± 0.1 for the quasar, -0.8 ± 0.1 for the companion SFG and -0.9 ± 0.1 for the western lobe (B1). Calculating spectral indices between L- and X-bands from Feain et al. (2007), -1.0 ± 0.1 for the quasar, -0.8 ± 0.1 for the companion SFG and -1.0 ± 0.1 for the western lobe. The quoted uncertainties are the errors returned by a linear regression fit to the individual flux measurements when these are inversely weighted by their own measurement errors. The observed steep radio spectral index is typical for Seyfert galaxies (e.g. de Bruyn and Wilson, 1978; Rush et al., 1996). The spectral index of the companion SFG exactly matches the canonical value of an SFG Condon (1992). The synchrotron spectra of all three main radio sources show no signs of curvature, i.e. spectral indices calculated between 1.8 and 4 GHz, and 4 and 6 GHz are highly consistent, as is the spectral slope between the *ATCA* 8.6 GHz flux and our lower frequency data. This enables us to reliably extrapolate fluxes measured on the C-band image to 1.4 GHz to derive SFRs and to try to constrain AGN contribution to the quasar's radio emission as discussed in Section 2.4.1.

2.3.2 First evidence for a bipolar outflow in HE0450–2958

The combined, deep 5-GHz intensity map shows substantial residual emission around the two strong single-component sources (see Fig. 2.2 right). To examine these residual features in more detail, we subtracted the fitted 2D elliptical Gaussian flux model of both the quasar and the companion SFG (see introductory paragraphs of Section 2.3) from the C-band image. The

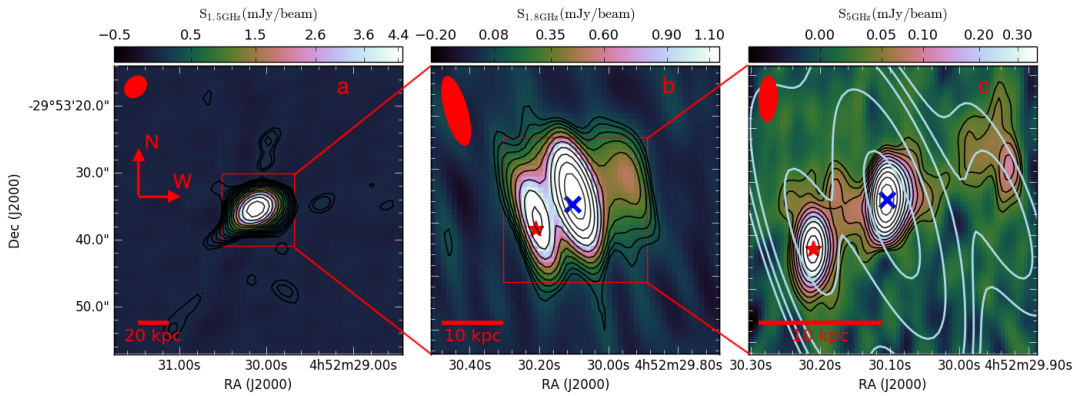

Figure 2.2: Overview of HE0450–2958 multi-frequency data described in this paper. Black flux density contours measured with the JVLA start at $3\,\sigma$ (where σ is 16, 32 and 11 μJy beam^{-1} at 1.5, 1.8 and 5 GHz, respectively, see Table 4.1), all other contours are $\sqrt{2}^n$ of these. **a)** JVLA 1.5 GHz (L-band) wideband image obtained in BnA configuration. The total cut-out size is 43.3 arcsec ×43.2 arcsec(188×188 kpc^2). Down to a rms noise level of 16 μJy beam^{-1} (corresponding to a $3\,\sigma$ upper limit on the SFR of 36 $M_\odot$ yr^{-1}) we find no evidence for synchrotron emission from extended emission line regions in the vicinity of HE0450–2958. The red square shows the region plotted in the central, b) panel of the figure. **b)** JVLA 1.8 GHz image obtained with A array configuration (cut-out size: 10.8 arcsec ×10.8 arcsec or 47×47 kpc^2). The cut-out spans the −29:53:46.32 – −29:53:24.72 declination range. The same triple structure as observed at higher frequencies is visible. The red square shows the region plotted in the right-hand figure panel. **c)** JVLA 5 GHz (C-band) image obtained in A array configuration (cut-out size: 5.4 arcsec ×5.4 arcsec or 23.5×23.5 kpc^2). Contours overlaid in light blue are from the lower resolution 6.2 GHz ATCA image in Feain et al. (2007). ATCA contour levels are 0.2 μJy beam^{-1} ($5\,\sigma$), 0.28 μJy beam^{-1} ($7\,\sigma$), 0.4 μJy beam^{-1} ($10\,\sigma$), 0.8 μJy beam^{-1} ($20\,\sigma$) and 1.4 μJy beam^{-1} ($35\,\sigma$). The cut-out spans the −29: 53:40.92 – −29:53:30.12 declination range. At the highest resolution the triple structure in the central panel is resolved into a more complex radio flux distribution. Red ellipses in all panels denote the FWHM of the JVLA restoring beam at the respective frequencies. The red star and the blue cross show the HST optical image positions of the companion SFG and quasar, respectively (see Fig. 2.1).

Object	RA (J2000)	DEC (J2000)	Size (kpc)	$L_{1.4}$ (log(W/Hz))	$S_{1.8}$ (mJy)	S_4 (mJy)	S_6 (mJy)	S_C (mJy)	α
Quasar	04:52:30.10	−29:53:35.3	1±0.1	24.23±0.07	5.52±0.29	2.51±0.15	1.77±0.02	1.74±0.08	−1.0±0.1
CSFG	04:52:30.21	−29:53:36.3	1.3±0.3	23.81±0.07	2.76±0.27	1.39±0.11	1.02±0.17	0.89±0.02	−0.8±0.1
B1	04:52:29.96	−29:53:34.5	-	23.65±0.14	1.34±0.09	0.49±0.07		0.45±0.05	−1.0±0.2
B2	04:52:30.05	−29:53:35.2	-	23.14±0.20	-	-	-	0.22±0.02	−0.7±0.3
B3	04:52:30.16	−29:53:35.5	-	23.14±0.20	-	-	-	0.22±0.03	−0.7±0.3
B4	04:52:30.25	−29:53:35.4	-	22.57±0.22	-	-	-	0.059±0.014	−0.7±0.3

Table 2.2: HE0450–2958 source properties. B1-B4 are the outflow related patches of radio emission (see their spatial distribution in Fig. 2.4b). Sizes, where given, are the deconvolved, intrinsic, circularised source size FWHMs fitted with CASA. $S_{1.8}$, S_4 and S_6 were measured on resolution-matched images (see Sect. 2.3.1.). The spectral index (α) was fitted using this resolution-matched photometry. S_C is the flux measured on the combined C-band image at 5 GHz with its native, higher resolution. In this image the flux measured for the quasar and companion SFG are least contaminated by outflow-related emission from B2-B4, hence their fluxes are lower than measured at the higher frequency resolution-matched image. Due to its lower S/N in order to achieve the best fit we measured B1's resolution-matched photometry on the combined, higher sensitivity 5 GHz image. Using less reliable 4 and 6 GHz fluxes for B1 we calculate a consistent but less accurate spectral slope. Fluxes for outflow components B2-B4 were determined on the residual image produced by subtracting the quasar and companion SFG. The spectral index reported for B2-B4 is the average spectral slope of all outflow-related emission features, measured between 4 – 6 GHz (see Sect. 2.3.1 for details).

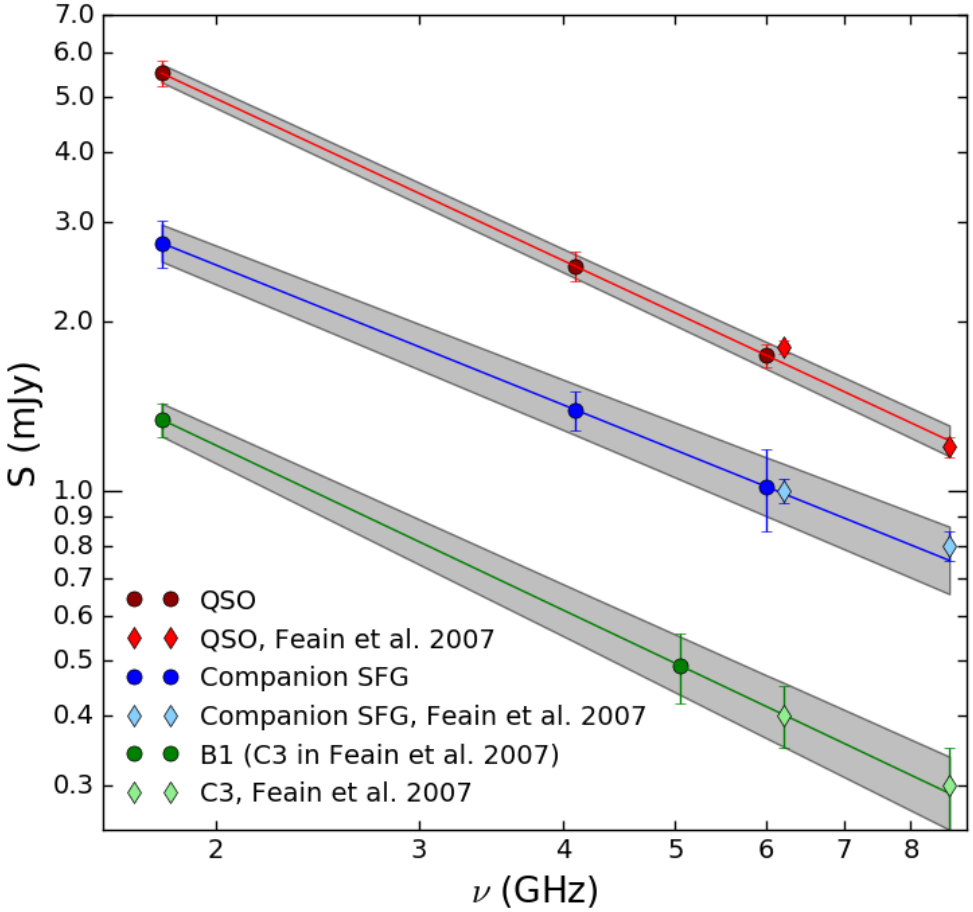

Figure 2.3: Observed radio fluxes of each object as a function of frequency with fitted radio syncrotron spectra. Fluxes were measured on resolution matched images (see Sect. 2.3.1). Dots are fluxes from this work, diamonds are measurements from Feain et al. (2007). Gray areas show 1 σ confidence intervals. All spectra are consistent with a single power law and match up with the previous flux measurements at > 6 GHz from Feain et al. (2007).

residual image contours superimposed on the HST optical image from M05 are shown in Fig. 2.4. To correct for the small astrometric inaccuracy of the optical image, we have shifted the *HST* positions by ∼ 0.2 arcsec to the south to match quasar's peak position on the JVLA image. The emission line blob found by M05 at optical wavelengths is now detected in radio emission for the first time ('B2'), and is paired with a second radio source ('B3') on the opposite side of the quasar (see Fig. 2.4). We note that 'B2' was also resolved in the mid-infrared (MIR) by Elbaz et al. (2009); see their Fig. 4(a). An imaginary line drawn through these two blobs of emission ends in an extended western radio lobe ('B1'; referred to as 'C3' in Feain et al. 2007) ∼ 10 kpc to the west of the quasar and intersects the northern quadrant of the companion SFG to the east, as well as a smaller patch of emission,'B4', on the far side of the companion SFG (∼ 8 kpc east of the quasar). They are most likely physical sources and not imaging artefacts; dirty beam pattern centred on the quasar's and companion SFG's peak positions shows that these residual emission blobs are spatially not correlated with any sidelobes.

This is the first evidence for a bipolar outflow from the HE0450–2958 quasar extending over nearly 10 kpc both westward and in the direction of the companion SFG to the east. Previous observations achieved only a tentative detection of the western lobe but not the eastern component due to blending with the companion SFG's flux in the much more poorly resolved ATCA images.

The 5-GHz radio flux density of the outflow components decreases from west to east (i.e. from B1 to B4, for the spatial distribution of these residual features see Fig. 2.4b). B4 on the eastern end of the outflow has a flux density of 59±14 μJy (S/N = 4.2), ∼13 % of the flux of 450±46 μJy (S/N = 9.8) measured for B1 on the opposite side of the outflow. Nearer the quasar B2 and B3 have very similar flux densities (220±24μJy for B2 and 220±32 μJy for B3; S/N = 9.2 and S/N = 6.9 respectively and roughly half of B1's flux).

In the individual C-band spectral windows, the noise is too high to determine the 4–6-GHz spectral slopes of the outflow components B2–B4 individually. However, it is possible to measure their summed flux at both 4 and 6 GHz with an aperture covering all three objects. The average 4–6-GHz spectral index of the outflow-related emission components B2–B4 is -0.7 ± 0.3.

Using VLT/FORS and VLT/VIMOS data, Letawe et al. (2008) found several clouds of highly ionized gas along the radio axis defined by Feain et al. (2007). With our sub-arcsecond 5-GHz imaging, we can determine a more precise angle for the radio axis, that remains aligned with these clouds. The B1–B4 patches of radio emission spatially coincide with these emission line regions. B1, ∼ 10 kpc from the quasar, is associated spatially with Em3/Em4 and R3 from Letawe et al. (2008). B2, the blob detected 1 kpc to the west of the quasar by *HST*, was found to have AGN-ionized gas according to line diagnostic diagrams. B3 lies too close to the quasar emission, so it was not observed by VLT. B4 (Gal2/Gal3 in Letawe et al., 2008) shows a mix

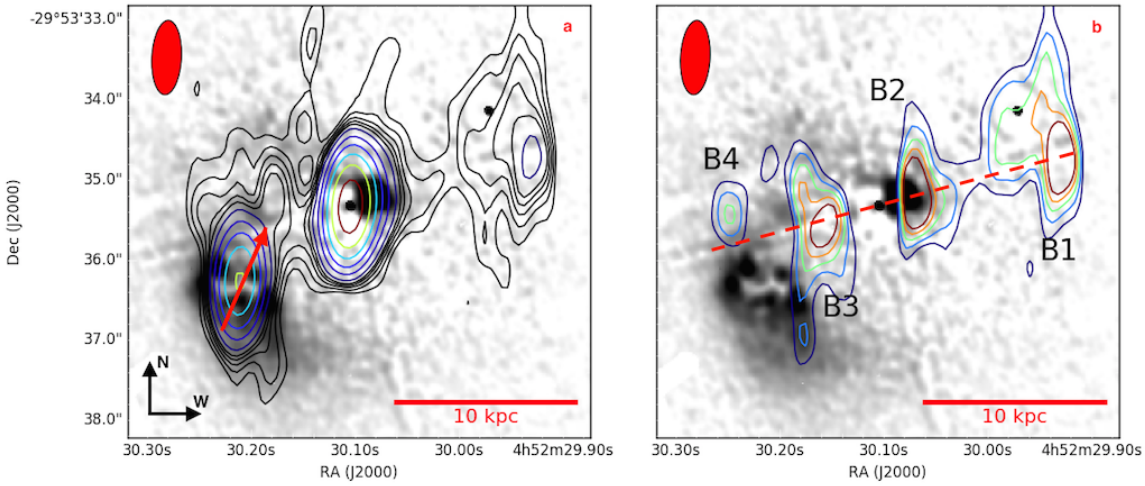

Figure 2.4: C-band emission associated with HE0450–2958, superimposed on the PSF-deconvolved, HST optical image from M05. **Left:** JVLA 5 GHz (C-band) image. Black contours range from 33 μJy beam^{-1} (3σ) to 77 μJy beam^{-1} (7σ) by 1σ steps (same as contours on the right-hand panel for direct comparison). Coloured contours start at 99 μJy beam^{-1}, all other levels are $\sqrt{2.5}^{n}$ multiples of the 9σ contour. To correct for a small astrometric inaccuracy we have shifted the positions of the radio maps by $\sim$ 0.2 arcsec to the south to match quasar's peak position on both images. The centroid of the radio emission from the companion SFG coincides with its dust obscured central region. Red arrow across the SFG points towards the flatter spectral index area, towards the projected jet axis (dashed line in panel b). **Right:** Residual 5 GHz emission after subtraction of the 2-D elliptical Gaussian flux models for the companion SFG and quasar from the overall C-band flux distribution shown in Fig. 2.2c. Emission features in the residual map (labeled B1 to B4 from west to east) follow a linear alignment reminiscent of a quasar-driven outflow. Contour levels range from 33 μJy beam^{-1} (3σ) to 77 μJy beam^{-1} (7σ) in 1σ steps. Component B2 is spatially associated with an emission line blob detected at optical wavelengths. Component B1 is the western lobe identified by Feain et al. (2007) in lower resolution imaging (see also Fig. 2.2b/c).

of stars and ionized gas. They have also observed two other emission line regions (Em1 and Em2) ∼ 10 kpc north and south of the quasar that were not detected by the JVLA at radio frequencies.

2.3.3 Companion galaxy – dust-obscured SF and spectral index variations

Our 5-GHz imaging reveals that the radio emission from the companion SFG peaks in its central, strongly dust-obscured region. This is shown in Fig. 2.4(a) where radio flux contours are superimposed on the HST F606W image of M05 that, at z = 0.285, samples a restframe wavelength of 433 nm. The 5-GHz emission associated with the companion SFG is well fit by a single 2D elliptical Gaussian (< 30 μJy) with integrated flux $S_C = 0.89 \pm 0.02$ mJy. The galaxy's apparent source size on the combined 5-GHz image is 0.99 arcsec × 0.44 arcsec. Its emission is resolved on both beam axes with a deconvolved, physical source size (FWHM) of (1.6±0.2) × (1.0±0.1) kpc. After conversion to a 1.4-GHz flux S1.4 with equation 2.1 (where we are able to use our directly measured spectral index $\alpha = -0.8 \pm 0.1$, see Section 2.3.1), we can estimate the rest-frame 1.4-GHz luminosity of the companion SFG,

$$\left(\frac{L_{1.4}}{\mathrm{W\,Hz^{-1}}}\right) = 9.51 \times 10^{15} \, \frac{4\pi}{(1+z)^{(1+\alpha)}} \left(\frac{D_L}{\mathrm{Mpc}}\right)^2 \left(\frac{S_{1.4}}{\mathrm{mJy}}\right), \tag{2.2}$$

where D_L is the luminosity distance and z its redshift. Following Bell 2003, the 1.4 GHz luminosity $L_{1.4} = (6.52 \pm 0.20) \times 10^{23}$ W/Hz of the companion SFG translates to a SFR of 360±11 $M_\odot$ yr^{-1}. This is consistent with the SFR derived from infrared spectral energy distribution (IR SED) fitting in Elbaz et al. (2009) (∼340 $M_\odot$ yr^{-1}), who resolved the companion SFG at 11.3 μm using the VLT-VISIR camera (see their fig. 4a). This agreement, in combination with the fact that both radio and MIR emission are resolved on physical scales larger than expected from AGN activity, suggests that the radio synchrotron flux from the companion SFG is dominated by centrally concentrated starburst activity. This makes the presence of a strong AGN in the companion SFG as suggested by Letawe et al. (2009) and Letawe and Magain (2010) unlikely. In Sect. 2.4.2 we attempt to find an upper limit to a possibly weaker AGN activity.

In Section 2.3.2, we showed that outflow-related radio emission features are linearly aligned along an axis that crosses the northern part of the companion SFG. We lack information on the 3D orientation of the outflow to unambiguously tell whether it actually interacts with the companion SFG. However, the marked flux difference between the two most distant outflow components, B1 and B4 (which is in contrast with the very similar brightness of components B2 and B3, that are located closer to the quasar), indicates that the density of the medium the eastern and western lobes traverse through is not the same. This could be interpreted as evidence that the eastern outflow does impinge on the companion SFG and interact with its ISM. If this is the case, we might expect a different synchrotron spectral index in the northern sector of the companion SFG due to the acceleration of charged particles in shocks in the

jet–ISM interaction region. We will discuss the implications of this for the jet-induced SF hypothesis in Section 2.4.2.

Given that we have spatially resolved the companion SFG in our C-band image, we made a first attempt to search for internal, coherent spectral index variations across the galaxy. We consider all pixels where flux is detected at S/N > 5 in both the spectral window centred at 4 and at 6 GHz, an area equivalent to 3–4 independent resolution elements (referenced to the average synthesized beam size of the two spectral windows). It is possible to define up to three independent, beam-sized regions on the image to sample spectral slope variations between the resolution-matched 4- and 6-GHz images (common resolution: 1.16 arcsec × 0.41 arcsec). The first of these beam-sized regions was centred on the peak of the 2D Gaussian model for the companion SFG. The other two regions were offset 0.8 arcsec (3.5 kpc) from the galaxy centre, along an axis running approximately north–south across the galaxy. (This axis links the regions nearest and farthest in projection from the quasar outflow axis and is indicated with a red arrow in Fig. 2.4(a). The head (tail) of the arrow coincides with the centre of the southern (northern) resolution element used in our spectral index analysis.) The northernmost resolution element may contain some emission from the quasar outflow component B3. We thus also used a two-region configuration (where independently resolved regions were centred on the southern and the northern half of the galaxy along the same axis as before, see red arrow on Fig. 2.4a) as a second, more conservative test of spectral index variations out to maximally 1.8 kpc from the centre. The average spectral indices measured pixel-to-pixel in the three-beam configuration are $-1.35^{+0.81}_{-0.38}$, $-0.93^{+0.10}_{-0.11}$ and $-0.49^{+0.58}_{-0.95}$, in the two-beam configuration $-1.07^{+0.37}_{-0.14}$ and $-0.79^{+0.15}_{-0.26}$ (measurements always ordered from south to north, see in Fig. 2.4 the red arrow). These uncertainties span the $1\,\sigma$ confidence region and were estimated using a resampling approach to generate a million realizations of the individual pixel fluxes in each spectral window based on the noise measured at 4 and 6 GHz. While these values suggest a consistent trend towards a flatter synchrotron spectrum in northern part of the companion SFG, the associated uncertainties imply that the spectral index in the northern- and southern-most resolution elements is still consistent within their errors. To test at which significance level we are able to constrain the spatial spectral index gradient from north to south, we derived the best-fitting parameters of the following linear relation between spectral index $\alpha(r)$ and the distance $r - r_c$ from the central galaxy position (determined by the distances to the central position of each of the regions used):

$$\alpha(r) = \alpha(r_c) + d\alpha/dr * (r - r_c)\,. \tag{2.3}$$

Here $\alpha_{(r=r_c)}$, the spectral index at r_c, and $d\alpha/dr$, the spatial spectral index gradient, are the two free parameters. The results are shown in Fig. 2.5. The best-fit central spectral index values $\alpha_{(r=r_c)}$ are $-0.9^{+0.2}_{-0.2}$ (two-beam sampling) and $-1.1^{+0.2}_{-0.4}$ (three-beam sampling). Offsets from the measured -0.8 ± 0.1 (reported in Sect. 2.3.1) are the consequence of the different resolutions used to extract the fluxes, and that these spectral indices were measured

over a shorter frequency baseline (1.8-GHz data could not be used in the present analysis due to its poorer resolution). We find a median value of $d\alpha/dr = 0.11^{+0.10}_{-0.08}$ kpc^{-1} (two-beam configuration) and $0.13^{+0.12}_{-0.11}$ kpc^{-1} (three-beam configuration) for the gradient of the spatial spectral index variations. (The 1σ errors quoted are the result of selecting one of our resampled spectral index values in each of the three/two resolution elements and fitting equation 2.3 for all our Monte Carlo realizations.) 91 per cent (two-beam configuration) and 85 per cent (three-beam configuration) of the values lie above 0, i.e. imply a flattening of the spectral index in the companion SFG's northern sector. With the present data, we have only been able to detect these spatial spectral index variations within the companion SFG at a low-significance level. Taken at face value, however, the flatter spectral index in the northern part of the galaxy could be interpreted as a younger synchrotron-emitting electron population in this region. This observation is broadly consistent with the jet-induced SF hypothesis of (Elbaz et al., 2009, see further discussion in Section 2.4.2) and may hence be taken as tentative evidence that the outflow identified in Section 2.3.2 not only overlaps with the companion SFG in projection, but is actually interacting with its ISM.

2.3.4 Quasar – evidence for a star-forming host galaxy and classification as a compact steep spectrum source

The measured flux of the quasar at the native 5-GHz resolution is 1.74±0.08 mJy, corresponding to $\log(L_{1.4}[W/Hz]) = 24.23 \pm 0.07$ at the quasar redshift. The deconvolved, physical source size of the radio emission associated with the quasar derived from the 5-GHz image is (1.2±0.3)×(0.8±0.3) kpc. This is consistent with the 600 pc lower limit of Feain et al. 2007. The extent of the emission suggests that not all of it is due to the central engine; it has at least some contribution from star formation activity as well. The large-scale environment (> 20 kpc) shows no sign of extended emission line regions (see Fig. 2.2.a) down to the 3σ level of 48 μJy beam^{-1}.

Based on its steep radio spectrum (see Sect. 2.3.1.) and compact linear projected size of its outflow (∼ 20 kpc across, see Sect. 2.3.2.) the quasar can be classified as a compact steep spectrum source O'Dea (1998) which may imply that it is a recently activated, nascent AGN (see e.g. Fanti et al., 1995). The absence of far-field ionized regions support this interpretation as well.

2.4 Discussion

2.4.1 Disentangling SF and AGN activity in the quasar

The physical extent of the emission towards the quasar suggests that the putative quasar host contains at least some SF activity (see Section 2.3.4). To gauge its relative importance

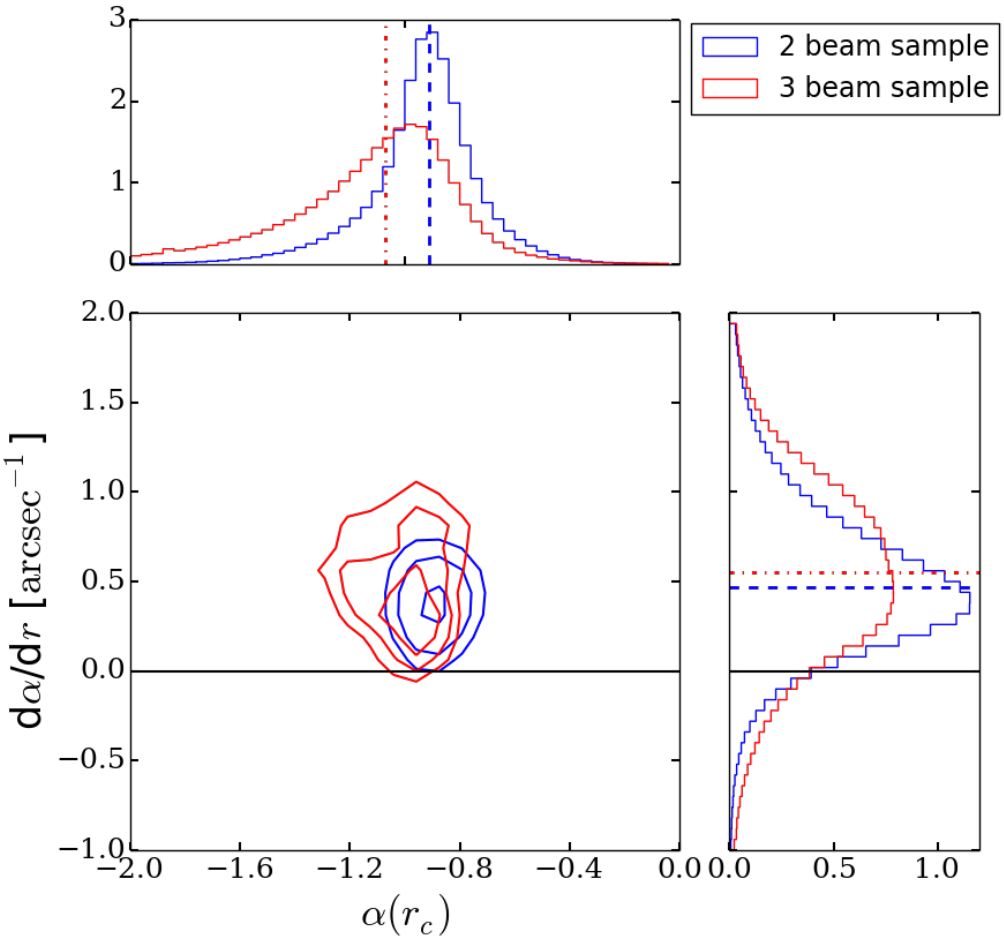

Figure 2.5: 2D histogram of measured central spectral indices ($\alpha(r_c)$) and spectral index gradients ($\mathrm{d}\alpha/\mathrm{d}r$) across the star-forming companion SFG using two (blue) and three (red) beam sized regions to sample fluxes and measure spectral indices (for details see Sect. 2.3.3). Contours are at 50 per cent, 68 per cent and 98 per cent of the maxima of each distribution. Dotted lines show the medians of the distributions. Both spatial sampling approaches yield consistent results, the two beam sampling has lower variance. 91 per cent (two-beam configuration) and 85 per cent (three-beam configuration) of the spectral slope gradients are consistent with a flatter spectral index in the northern part of the galaxy ($d\alpha/dr > 0$) which overlaps with the (projected) outflow axis.

compared to the AGN component, we use archival VLBI data. We will follow a similar line of argument as Feain et al. (2007) but can now base our statements on the more accurately determined radio spectral indices of the quasar and surrounding emission line regions (see Section 2.3.1). HE0450–2958 was observed in 1990 and 1991 (Roy et al., 1994) with the decommissioned Parkes-Tidbinbilla real-time interferometer (PTI; Norris et al., 1988) at 2.3 GHz. At this frequency, the interferometer was only sensitive to emission from scales smaller than 0.1 arcsec ($\sim$ 400 pc at the redshift of HE0450–2958), e.g. compact emission from AGN. HE0450–2958 was not detected down to a 3σ limit of 2 mJy.

This upper limit can be used as a constraint on the radio flux from the central AGN, and hence to calculate a lower limit on the spatially more extended SF activity of the host galaxy. Our best estimate of the combined flux due to AGN and SF activity in the quasar comes from our sub-arcsecond C-band image. To derive a constraint on the host galaxy SFR, we thus have to extrapolate from the PTI 2.3 GHz upper detection limit to a flux constraint at 5 GHz. While we do not have accurate information on the spectral index of the AGN-related emission, the overall spectral shape of the quasar, as measured in the resolution-matched 1.8-, 4- and 6-GHz images (see Section 2.3.1), provides some clues. The total quasar flux on these images at each frequency has contributions from AGN-related emission, SF activity and the quasar-driven outflow components B2 and B3 with unknown proportions, but none of them are negligible. As shown in Section 2.3.1, components B2 and B3 display a similarly steep spectral index $\alpha_{\mathrm{B2/B3}} = -0.7 \pm 0.3$, which is similar to that expected for the host galaxy SF contribution. Consequently, the AGN-related emission most likely has a spectrum comparable to all other components in order for the simple power-law shape of the overall quasar spectrum ($\alpha_{\mathrm{quasar}} - 1 \pm 0.1$, see Table 2.2) to be preserved. In this case, extrapolation of the PTI non-detection at 2.3–5 GHz and subsequent subtraction from the 2D Gaussian flux distribution centred on the quasar formally suggests that the quasar host galaxy could be undergoing SF activity approaching the level of a ULIRG (SFR $\geq 100 M_{\odot}$ yr^{-1}) and hence similar in intensity to the companion SFG.

It is worth noting that, according to Papadopoulos et al. (2008), the quasar host displays approximately fivefold weaker molecular emission than the companion SFG; for a common velocity range and CO-to-H_2 conversion factor ($\alpha_{CO} \approx 0.8\,\mathrm{M}_{\odot}\,[\mathrm{K\,km/spc^2}]^{-1}$) they estimated a 3σ upper limit on the molecular gas mass of $3.6{\times}10^9 M_{\odot}$. The halo of ionized gas surrounding the quasar (Letawe et al., 2008) is evidence of significant energy input from the AGN, in the form of radiative feedback, that may also have contributed to depleting the gas reservoir of the quasar host galaxy. At least two parallel lines of evidence (signatures of strong AGN feedback, plus matching SFR estimates for the companion SFG from spatially resolved radio data and unresolved FIR, see Section 2.4.2) hence suggest that ULIRG-like activity should be regarded as an upper limit to the host galaxy SFR. We also note that the PTI constraint from a single baseline snapshot observation might be sub-optimal due to its poor *uv* coverage.

In conclusion, due to our inability to robustly separate AGN and SF activity in the quasar

host galaxy, its properties remain poorly known. To directly determine these, new high-resolution observations are needed. A more sensitive VLBI follow-up could determine the amount of nuclear emission in the quasar. With ALMA, one could obtain more sensitive CO observations to place a more stringent limit on the gas content and a measurement of the dust continuum to see if there is evidence for cool dust heated only by SF in the quasar host. Moreover, high-resolution ALMA imaging also has the potential to clarify whether the blob B2 contains dust-obscured SF activity as traced by our radio detection and by MIR in Elbaz et al. (2009) or if it represents AGN-heated dust by an outflow component we have detected at radio wavelengths, as suggested by Letawe et al. (2008).

2.4.2 The companion galaxy – type and origin of activity

In previous work on HE0450–2958, two distinct triggering mechanisms for the strong SF activity in the companion SFG have been proposed: (a) interaction/merging between the companion and the quasar host galaxy (Letawe et al., 2008; Papadopoulos et al., 2008; Letawe and Magain, 2010), and (b) jet-induced SF (Feain et al., 2007; Elbaz et al., 2009). We will now discuss whether our new JVLA observations provide evidence in favour of either of these scenarios. In the preceding section, we showed that the quasar host, in addition to the AGN activity, is most likely undergoing SF as well. Our spatially resolved JVLA imaging allows us to address whether AGN and SF activity might be occurring simultaneously also in the companion SFG.

The relative importance of SF and AGN activity in the companion SFG

Based on its 5 GHz flux, we infer an SFR of 360±11 $M_{\odot}$ yr^{-1} for the companion SFG. This agrees well with the previously reported values of ~370 $M_{\odot}$ yr^{-1} (Papadopoulos et al., 2008) and ~340 $M_{\odot}$ yr^{-1} (Elbaz et al., 2009), which were derived with SED fits predominantly based on MIR and FIR flux densities measured with IRAS and VLT-VISIR. Since the companion SFG resides squarely on the IR–radio relation (q =2.5, i.e. offset by a mere 0.02 dex from the local IR–radio relation in Yun et al. (2001) and Bell (2003)), there is no clear evidence of AGN activity contributing to the radio or IR flux densities of the companion SFG. However, given our detection of spatially extended SF in the quasar host galaxy (see Section 2.4.1), it is plausible that it could potentially contribute to the IRAS FIR photometry at levels comparable to the contribution from the companion SFG. In the simultaneous, joint IR SED fitting of the companion SFG and the quasar, the companion galaxy was previously assumed by both Papadopoulos et al. (2008) and Elbaz et al. (2009) to strongly dominate the IRAS photometry[6] at rest-frame wavelengths > 40 μm. With a more even split of dust-obscured SF activity between quasar host and companion SFG (see Section 2.4.1), the SFR values reported for

[6]Due to the relatively poor angular resolution of IRAS the emission from the quasar and companion SFG are entirely blended in the IRAS maps.

the companion SFG by Papadopoulos et al. (2008) and Elbaz et al. (2009) would effectively represent upper limits, implying that its radio-based SFR exceeds that inferred from the FIR. While this could be interpreted as due to contamination from AGN-related radio emission, it is not clear that the effect would be large enough to move the companion SFG significantly beyond the scatter of the IR-radio correlation (~0.3 dex; e.g. Yun et al., 2001; Sargent et al., 2010) such that the companion SFG would enter the regime of radio-loud AGN. Furthermore, we have shown in Section 2.3.3 that the radio continuum emission from the companion SFG is distributed on a scale of ~1.5 kpc. We note that on the 11.3-μm VLT-VISIR image, the companion SFG was also found to be extended (i.e. there is no evidence for a dominant near-IR power-law AGN component; Elbaz et al., 2009), which further implies that the emission is mostly due to SF activity in companion SFG. For the remainder of the discussion, we will hence assume that the SFR of the companion SFG is not changed significantly by assigning some FIR flux to the quasar host galaxy and adopt 360 $M_{\odot}$ yr^{-1} for its SFR.

This estimate on the SFR allows us to reassess the companion SFG's specific SFR and depletion time-scale.[7] The stellar mass of the companion SFG is estimated at $5-6\times10^{10}\,M_{\odot}$ by Elbaz et al. (2009). Its specific SFR (~ 6.5 Gyr^{-1}) makes it a strong starburst galaxy with a factor 40 offset from the main sequence (MS; using the evolutionary fit to compiled literature data) of star-forming galaxies (Sargent et al., 2014) at z ~ 0.3. Elbaz et al. (2009) also found that it has a young (40–200 Myr) stellar population.

The gas mass of the companion SFG was estimated[8] by Papadopoulos et al. (2008) to be $1.3-2.3\times10^{10}\,M_{\odot}$. In combination with the radio-based SFR, these gas masses translate to a gas depletion time-scale of $t_{dep} \equiv \mathrm{M_{H_2}/SFR}$ = 12-50 Myr, assuming a constant gas consumption rate and no in- or outflows. Together with the young stellar population and the large offset from the star-forming MS, these short depletion times indicate that the companion SFG is currently undergoing a short-lived, high-efficiency SF phase, which might provide further clues towards the nature of the triggering mechanisms, as discussed in the following

[7] We note that even for a ULIRG-like SFR for the quasar host (SFR $\geq 100 M_{\odot}$ yr^{-1}), which would lead to a commensurate reduction of SFR of the companion SFG, our subsequent conclusions on depletion time and excess specific SFR remain qualitatively correct. (That is, the statement that the companion SFG lies well above the star forming MS and has a short depletion time compared to MS galaxies is robust to such changes.)

[8] Papadopoulos et al. (2008) adopt a CO-to-H_2 conversion factor in the range $\alpha_{\mathrm{CO}} = 0.55-1\,[M_{\odot}\,K\,km/s\,pc^2]^{-1}$ where the lower limit is for optically thin CO[1-0]-emission and the upper bound reflects dynamical constraints derived by Downes and Solomon (1998) for local starburst ULIRGs. Following the scaling relations calibrated in the 2-Star Formation Mode (2-SFM) framework of Sargent et al. (2014), a similar value of $\alpha_{\mathrm{CO}} = 0.8-1\,[M_{\odot}\,K\,km/s\,pc^2]^{-1}$ is on average expected on statistical grounds for a z ~ 0.3 galaxy with the stellar mass and SFR measured for the companion SFG. Note that larger α_{CO}-values we found in two-phase modeling of local starbursts (Papadopoulos et al., 2012) implying depletion times of ~ 100 Myr for the companion SFG. This figure remains significantly shorter than the depletion times of normal low-z galaxies (Leroy et al., 2008; Saintonge et al., 2011). Since both quasar and the companion SFG are ULIRGs this alternative technique for deriving CO-to-H_2 conversion factors is unlikely to significantly change the relative amount of molecular gas in the two systems.

section.

Starburst in the companion SFG – merger- or jet-induced origins?

In summary, the observations we have are: (i) projected outflow axis intersecting companion SFG's northern half (Section 2.3.2), (ii) possible spectral index variation across the star-forming region in the companion SFG towards the point of intersection (Section 3.3 2.3.3), (iii) a short, very intense starburst phase in companion SFG (Section 2.4.2) and (iv) a small projected linear size for the outflow from the quasar, indicative of recently started AGN activity (Section 2.3.4).

Merger-induced star formation Should the evidence for (ii) not be corroborated by future, higher quality observations and (i) be purely due to projection or if the jet–ISM interaction does not trigger SF in the companion SFG, then an interaction-induced starburst is the most plausible mechanism for generating SF with the intensity observed in this galaxy. Specifically, Papadopoulos et al. (2008) referred to this process in HE0450–2958 as a wet–dry merger due to the strongly asymmetric distribution of gas between the quasar host (which remained undetected in their CO follow-up observations) and its neighbouring galaxy. Merger-driven accumulation and compression of the dissipative gas phase in the central region of merger remnants is a well-established and widespread triggering mechanism in low-redshift, dust-obscured starbursts (Sanders and Mirabel, 1996, and references therein). However, in local (U)LIRGs, starburst activity is predominantly observed in the nuclei of fully coalesced galaxies (Sanders et al., 2003), while in the case of HE0450–2958, the ULIRG phase already occurs when the interacting galaxies are still separated by ~ 7 kpc.We also note that wet–dry interactions of $0 < z < 1.2$ galaxies on average do not enhance SF activity (Hwang et al., 2011). A possible explanation for this is the removal of gas from the late-type galaxy involved in wet–dry mergers through stripping in the hot halo of the early-type merging partner. Leroy et al. (2008) suggest that such a hot, ionized gas halo also surrounds HE0450–2958, probably due to radiative feedback from the AGN. There are hence at least two atypical features of HE0450–2958 if a wet–dry merger is indeed the main cause for the SF activity in the companion SFG.

Jet-induced star formation hypothesis Evidence for jet-induced SF has so far been reported for a fairly small number of galaxies: Minkowski's Object, a peculiar star-forming dwarf galaxy lying in the cone of the jet from the powerful radio source NGC 541 (Croft et al., 2006); Centaurus A (Schiminovich et al., 1994; Charmandaris et al., 2000) and 3C 285 (van Breugel and Dey, 1993), both nearby radio galaxies with complex, star-forming filamentary structures along their radio lobes; and 4C 41.17, a radio source at $z = 3.8$ (**?**De Breuck et al., 2005; Papadopoulos et al., 2005). Their rarity and the low redshift of most of these objects reflects the fact that high-resolution and detailed multifrequency data are required to identify

such systems. However, jet-induced SF may be more common, especially among high-redshift galaxies (as suggested by, e.g. radio-optical alignments, see McCarthy et al., 1987).

In the case of HE0450–2958, the analysis of the spatial distribution of emission line ratios in Letawe et al. (2008) revealed the presence of shocked gas in the northern half of the companion SFG consistent with a jet–ISM interaction in the companion SFG as evidenced by (i) and (ii). It is possible for such an interaction to accelerate the conversion of HI to H_2 as discussed by, e.g. Nesvadba et al. (2011). For this H_2 reservoir to be able to actually produce new stars, it needs to cool and reach sufficiently high densities. Cooling may only be possible where turbulent energy input by the jet does not dominate the ISM energetics (e.g. after the jet has subsided or at a sufficient distance from the interaction region). For high-efficiency starburst activity as observed in the companion SFG, a significant fraction of the gas must, furthermore, be in a dense phase (Renaud et al., 2012). It is possible that these conditions are met in its central region, i.e. >1 kpc from the jet axis and where the gas density would have been highest to begin with. Alternatively, the central parts of the companion SFG might have been impacted more directly by the jet in the past due to either the relative motion of the companion with respect to the quasar (which, for purely tangential motion of the order of 100 km s^{-1}, could have caused the jet axis to wander from the galaxy centre to its present location on a time-scale of $\sim 10^7$ years) or quasar jet wobbling.

With the currently available data, it is not possible to draw a definitive conclusion on whether an interaction-induced starburst, or SF related to a jet–ISM interaction, is the primary trigger of the activity in the companion SFG. It is even conceivable that a combination of these two phenomena might be occurring in HE0450–2958. It should be mentioned, however, that the probability of two extremely short-lived and rare events such as (iii) and (iv) happening simultaneously in the same system without any causal connection seems small. Intriguingly, the SF efficiency we have re-estimated based on our new JLVA continuum data is also comparable to that found for Minkowski's Object (depletion time <20 Myr; Salomé et al., 2015).

The continued ambiguity of the SF process in the companion SFG illustrates how complex (combinations of) feedback processes are in practice and how important in-depth observations are for their implementation in galaxy evolution models. For an improved understanding of this gas-rich and dusty system, further study of the gas kinematics and energetics is indispensable. Specifically, a spatially resolved imaging of the CO spectral line excitation diagram would permit a separate mapping of the excitation, density, and kinematics of both the warm and cool molecular reservoirs. Moreover, follow-up of a dense gas tracer such as hydrogen cyanide (HCN) could reveal whether or not the HCN/CO ratio of the companion SFG is comparable to that of local, merger-driven starburst ULIRGs.

2.5 Summary

We have observed HE0450–2958, a $z = 0.285$ galaxy pair consisting of a quasar with an elusive host galaxy and an actively star-forming companion SFG, at 1.8, 4 and 6 GHz using the JVLA.

We find that radio emission towards the quasar is resolved. The intrinsic physical size of the radio-emitting region is ∼1 kpc. The presence of this extended emission suggests that the AGN host galaxy is still forming stars and might be doing so at a rate of $\geq 100\,M_{\odot}\,\mathrm{yr}^{-1}$.

In previous literature, both a galaxy–galaxy interaction and a jet-induced SF have been proposed as triggering mechanisms for the starburst in the companion galaxy. We revisit the evidence for both of these in the light of our new JVLA observations in Section 2.4.1. These observations were designed to test the jet-induced SF hypothesis and the spatial alignment of the quasar jet axis and the companion galaxy, combined with the tentative evidence for radio spectral index variations within it, implies that a jet–ISM interaction remains a valid scenario. HI to H_2 conversion via turbulent compression could then have led to SF in regions where energy input from the jet has subsided enough to allow cooling. With the currently available data, it is not possible to exclude interaction-driven gas dynamics as the prime trigger of the starburst. It is, however, one of the best-known examples of strong SF activity in the presence of a quasar-driven jet. Our new observations make HE0450–2958 a strong candidate for jet-induced SF and one of the rare links between local systems (like Minkowski's Object or Centaurus A) and the high-z regime where radio-optical alignments suggest that this phenomenon could be more common. HE0450–2958 is also an excellent illustration of the complex interplay between different astrophysical processes: simultaneous AGN and SF activity within individual galaxies and a combination of both negative (quasar host) and positive feedback (companion SFG). Further study of systems like this will provide important clues for understanding all facets of AGN feedback processes.

Contributions

MTS carried out the spectral index spatial variation analysis presented in Sect. 2.3.3, and wrote part of the text describing it. All co-authors contributed comments and advice.

Chapter 3

The infrared-radio correlation of spheroid- and disc-dominated star-forming galaxies to z ∼ 1.5 in the COSMOS field

This paper was published in Molnár et al., 2018, Monthly Notices of the Royal Astronomical Society, Volume 475, Issue 1, p.827-838.

Co-authors are:

Mark T. Sargent, Jacinta Delhaize, Ivan Delvecchio, Vernesa Smolčić, Mladen Novak, Eva Schinnerer, Giovanni Zamorani, Marco Bondi, Noelia Herrera-Ruiz, Eric J. Murphy, Eleni Vardoulaki, Alexander Karim, Sarah Leslie, Benjamin Magnelli, C. Marcella Carollo, Enno Middelberg

Abstract

Using infrared data from the Herschel Space Observatory and Karl G. Jansky Very Large Array (VLA) 3 GHz observations in the COSMOS field, we investigate the redshift evolution of the infrared-radio correlation (IRRC) for star-forming galaxies (SFGs) we classify as either spheroid- or disc-dominated based on their morphology. The sample predominantly consists of disc galaxies with stellar mass $\geq 10^{10}\,M_{\odot}$, and residing on the star-forming main sequence (MS). After the removal of AGN using standard approaches, we observe a significant difference between the redshift-evolution of the median IR/radio ratio $\overline{q}_{\rm TIR}$ of (i) a sample of ellipticals, plus discs with a substantial bulge component ('spheroid-dominated' SFGs) and, (ii) virtually pure discs and irregular systems ('disc-dominated' SFGs). The spheroid-dominated population follows a declining $\overline{q}_{\rm TIR}$ vs. z trend similar

to that measured in recent evolutionary studies of the IRRC. However, for disc-dominated galaxies, where radio and IR emission should be linked to star formation in the most straightforward way, we measure very little change in $\overline{q}_{\rm TIR}$. This suggests that low-redshift calibrations of radio emission as an SFR-tracer may remain valid out to at least $z \simeq 1-1.5$ for pure star-forming systems. We find that the different redshift-evolution of $q_{\rm TIR}$ for the spheroid- and disc-dominated sample is mainly due to an increasing radio excess for spheroid-dominated galaxies at $z \geq 0.8$, hinting at some residual AGN activity in these systems. This finding demonstrates that in the absence of AGN the IRRC is independent of redshift, and that radio observations can therefore be used to estimate SFRs at all redshifts for genuinely star-forming galaxies.

3.1 Introduction

Observations show that the total infrared and 1.4 GHz radio continuum luminosities of local galaxies are tightly correlated (van der Kruit, 1971, 1973; de Jong et al., 1985; Helou et al., 1985; Condon, 1992; Yun et al., 2001). This so-called infrared-radio correlation (IRRC) was found to be linear over at least three order of magnitudes in luminosity since the peak epoch of star formation (e.g. Sajina et al., 2008; Murphy, 2009). Thus it has been used to e.g. identify radio-loud AGN (e.g. Donley et al., 2005; Norris et al., 2006; Park et al., 2008; Del Moro et al., 2013), and to estimate the distances and temperatures of high-redshift submillimetre galaxies (e.g. Carilli and Yun, 1999; Chapman et al., 2005). It also enables the calibration of radio luminosities as dust-unbiased, high angular resolution star formation rate (SFR) tracers (e.g. Condon, 1992; Bell, 2003; Murphy et al., 2011, 2012; Delhaize et al., 2017; Davies et al., 2017). Future deep radio continuum surveys aiming to obtain a full census of dust-obscured star formation across cosmic time, even in crowded environments such as groups and clusters, will thus heavily rely on the measured IRRC to achieve their science goals. With the advent of new, high-sensitivity radio instruments (such as LOFAR, MeerKAT, ASKAP and the Square Kilometre Array) it is timely to study the redshift evolution and higher order dependencies of the IRRC, which contribute to, e.g., the scatter of the relation, in more detail.

Observationally it has been challenging to refine existing work on the IRRC due to the lack of sufficiently sensitive radio and infrared data. Sargent et al. (2010) showed that solely radio or infrared selected flux-limited surveys introduce a bias that artificially produces an evolution in the IRRC. To overcome this, they used flux limits for non-detections at either of these wavelength, and constrained the median infrared radio ratio with double censored survival analysis. They found no significant evolution in the IRRC out to $z \sim 1.5$ using VLA imaging of the Cosmological Evolution Survey (COSMOS; Scoville et al., 2007) field at 1.4 GHz (Schinnerer et al., 2007, 2010). Many other authors (e.g. Garrett, 2002; Appleton et al., 2004; Ibar et al., 2008; Garn et al., 2009; Jarvis et al., 2010; Mao et al., 2011; Smith et al., 2014)

have also found no significant evidence for evolution of the IRRC up to $z \sim 3.5$. However, a series of recent studies relying on the full far-IR coverage provided by the Herschel Space Observatory (Pilbratt et al., 2010), have found evidence for a changing IRRC across cosmic times (but see also Pannella et al., 2015). Magnelli et al. (2015) performed a stacking analysis of Herschel, VLA and Giant Metre-wave Radio Telescope (GMRT) radio continuum data to study the variation of the IRRC out to z < 2.3. They found a moderate, but statistically-significant evolution with $(1 + z)^{-(0.12\pm0.04)}$. Matching the depth of Herschel data with the sensitivity of LOFAR (van Haarlem et al., 2013) Calistro Rivera et al. (2017) measured a consistent redshift dependency of $(1 + z)^{-(0.15\pm0.03)}$ for star forming galaxies out to z ∼ 2.5. Most recently, Delhaize et al. (2017, D17 henceforth) presented new evidence for a similar declining trend in the infrared/radio ratio out to z < 5 using new, deep 3 GHz VLA images and Herschel FIR fluxes in the COSMOS field.

From a theoretical perspective, star-formation (SF) is thought to be the link between infrared and radio emission. Young, massive (>8 $M_\odot$) stars produce UV photons, that are mostly absorbed and re-emitted by the surrounding dust at far-infrared (FIR) wavelengths. Radio emission at low rest-frame GHz frequencies predominantly represents non-thermal synchrotron radiation emitted by relativistic cosmic ray (CR) electrons that move through galactic magnetic fields as they are accelerated by supernovae remnants (e.g. Condon, 1992). The IRRC thus arises if CR electrons radiate away all their energy before escaping the galaxy and if the interstellar medium (ISM) is optically thick in UV, reprocessing all the UV starlight into FIR emission. This so-called calorimetry theory was first proposed by Voelk (1989). Since then several studies have pointed out its shortcomings and provided alternative, more complex explanations (e.g. Helou and Bicay, 1993; Bell, 2003; Lacki et al., 2010; Schleicher and Beck, 2013), however the exact physical processes driving the relation remain unclear. Predictions for the redshift evolution of the IRRC are also often conflicting. On the one hand, an increase of infrared/radio flux ratios is expected (e.g. Murphy, 2009, and references therein); rather than undergoing synchrotron cooling, at higher redshift CR electrons should lose more and more energy through inverse Compton (IC) scattering off photons of the cosmic microwave background (CMB) as the CMB energy density increases with redshift, thereby violating electron calorimetry. On the other hand, Lacki and Thompson (2010) argues that this effect can be compensated by other IC loss effects (e.g. ionization, bremsstrahlung) preserving radio luminosity, especially in starbursts, hence keeping the relation constant up to at least $z \sim 1.5$.

An approach to observationally determine which physical processes regulate the IRRC is to identify what factors contribute to its ∼ 0.26 dex scatter (Bell, 2003). One would expect that, e.g., a non-SF related warm cirrus component at IR wavelengths or excess radio emission due to low level AGN activity, both phenomena more common in “red and dead” early-type galaxies, would cause deviations from the median IR/radio ratio. Finding such differences motivated this work, which is a direct follow-up of D17. Utilising the wealth of ancillary

data available in the COSMOS field, here we will study the IRRC's evolution in disc- and spheroid-dominated SFGs.

Throughout this chapter, we use a flat ΛCDM cosmology with $\Omega_M = 0.3$ and $H_0 = 70\,\mathrm{km\,Mpc^{-1}\,s^{-1}}$. Star formation rates and stellar mass values reported assume a Chabrier initial mass function (IMF).

3.2 Data

In order to investigate the dependence of the IRRC on galaxy morphology, we used a combination of Herschel and VLA 1.4 and 3 GHz data with added structural information from the Zurich Structure & Morphology Catalog[1]. Sargent et al. (2010) showed that considering only IR- or radio-selected samples of star-forming galaxies (SFGs) tends to, respectively, over- or underestimate average IR/radio ratios, with the typical offset between such samples being ∼0.3 dex. This is approximately the same as the intrinsic scatter of the IRRC itself (e.g. Yun et al., 2001), hence an accurate analysis of the relation should account for flux limits in both wavelength regimes. To overcome this bias we use a jointly-selected (i.e. both radio and IR) sample of galaxies. The following section briefly outlines the sample construction process. More details on all aspects of the summary provided in Sect. 3.2.1 can be found in D17.

3.2.1 Jointly-selected parent catalogue

We use the jointly-selected sample of D17 as our parent catalogue. It is the union of radio- and IR-selected samples in the 2 $\mathrm{deg^2}$ COSMOS field.

The IR-selected galaxy sample was constructed from a prior-based catalogue of Herschel flux measurements in the COSMOS field. 100 and 160 μm Herschel Photodetector Array Camera (PACS; Poglitsch et al., 2010) data are from the PACS Evolutionary Probe (PEP; Lutz et al., 2011). 250, 350 and 500 μm maps are provided by the Herschel Multi-tiered Extragalactic Survey (HerMES; Oliver et al., 2012). Their prior positions from the 24 μm Spitzer (Le Floc'h et al., 2009) MIPS catalogue were matched to the COSMOS2015 photometric catalogue (Laigle et al., 2016) containing both photometric and spectroscopic redshift information. D17 selected sources with $\geq 5\,\sigma$ detections in at least one Herschel band, in order to obtain an IR-selected catalogue that is comparable to the radio-selected sample (see below) in terms of SFR-sensitivity. This IR-selected catalogue contains 8,458 sources.

Our radio-selected catalogue is based on the imaging from the 3 GHz VLA-COSMOS Large Project. The VLA-COSMOS 3 GHz catalogue (Smolčić et al., 2017b) contains ∼11,000 sources down to $S/N = 5$ (the typical sensitivity is 2.3 $\mu\mathrm{Jy\,beam^{-1}}$ over most of the 2 $\mathrm{deg^2}$ area). In order to obtain rest-frame spectral energy distributions (SEDs) and calculate luminosities, reliable redshifts are required. Smolčić et al. (2017a) thus assigned optical/near-IR (NIR)

[1]Full catalogue with description is available at http://irsa.ipac.caltech.edu/data/COSMOS/tables/morphology/cosmos_morph_zurich_colDescriptions.html.

counterparts in unmasked regions (i.e. avoiding bright, saturated stars) of the COSMOS field where high-quality photometric data were available from the COSMOS2015 photometry catalogue (presented in Laigle et al., 2016). The sample of radio-selected sources with optical counterparts and known photometric or spectroscopic redshifts initially contains 7,729 objects. However, due to the 3 GHz mosaic's high angular resolution, some low surface brightness sources were below the 5 σ detection limit of this radio catalogue. To correct for this resolution bias, D17 searched for additional detections in 3 GHz maps convolved to lower resolutions of up to 3 arcsec and at the positions of IR-selected sources with no 3 GHz counterparts in the 0.75 arcsec mosaic. This yielded an additional 428 sources. We also added 1.4 GHz radio fluxes from the VLA-COSMOS catalogue (Schinnerer et al., 2007) to 27 IR-selected sources with no 3 GHz counterpart. Thus the final radio-selected sample consists of 8,184 sources.

The resulting jointly-selected sample contains 4,309 objects that were detected at both radio and IR wavelengths, 3,875 sources that have only radio detections and 4,149 sources with only IR fluxes measured. In the latter two cases we used 5 σ upper flux limits for the non-detections to help constrain the median infrared radio ratio. 37 % of the galaxies have spectroscopic redshifts in both the radio- and the IR-selected samples.

3.2.2 Morphologically-selected sub-samples

To add morphological information to the jointly-selected sample of D17, we cross-matched it with the Zurich Structure & Morphology Catalog. This catalog provides a classification of galaxies into different categories based on the ZEST (Zurich Estimator of Structural Types) algorithm (Scarlata et al., 2007). ZEST uses five nonparametric structural diagnostics (asymmetry, concentration index, Gini coefficient, second-order moment of the brightest 20 % of galaxy pixels, and ellipticity) measured on Hubble Space Telescope (HST) Advanced Camera for Surveys (ACS) I-band (F814W) images (Koekemoer et al., 2007) to morphologically classify sources. After carrying out a principal component (PC) analysis to reduce the number of parameters while retaining most of their information content, ZEST uses a 3D classification grid to define three main galaxy types: elliptical (type 1), disc (type 2) and irregular (type 3) objects. Type 2 was then further divided into four bins (i.e. 2.3, 2.2, 2.1 and 2.0), guided by the Sérsic index n of galaxies in the 'disc' class (Sargent et al., 2007). These sub-classes reflect an increasing prominence of the bulge component from type 2.3 to 2.0, i.e. type 2.3 are pure disc galaxies, type 2.0 are strongly bulge-dominated discs, while types 2.1 and 2.2 have intermediate bulge-to-disc ratios. The application of ZEST to a sample of low-redshift galaxies from Frei et al. (1996) with RC3 classifications (de Vaucouleurs et al., 1991), showed that type 1 objects are mostly classified as Hubble type E, type 2.0 corresponds to S0 - Sab galaxies, type 2.1 mainly consists of Sb - Scd systems, type 2.2 sources are split between Sb-Scd and Sd and later types, and type 2.3 maps into Sd discs or even later RC3 types (for detailed distributions see Fig. 6 in Scarlata et al., 2007).

The Zurich Structure & Morphology Catalog was position-matched to the optical positions

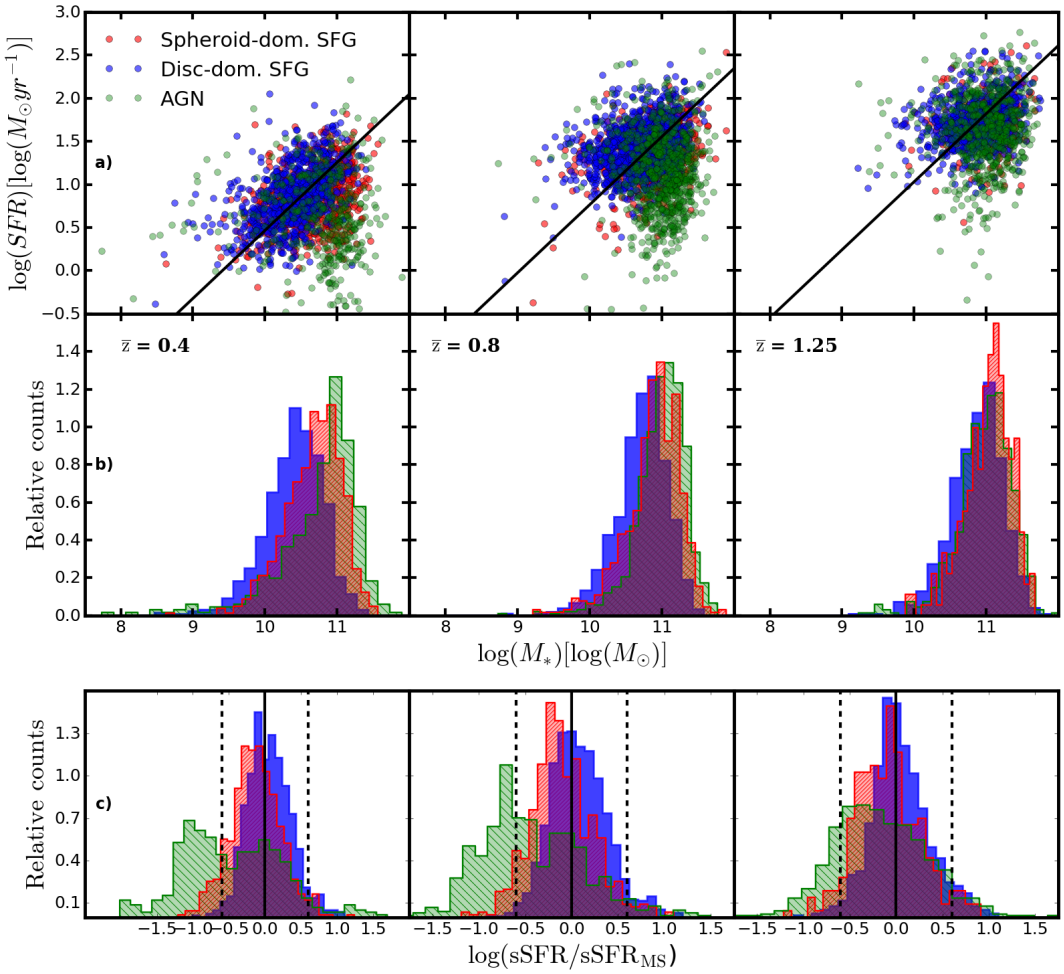

Figure 3.1: **a)** Spheroid- and disc-dominated SFGs and AGN in the stellar mass – SFR plane in three redshift slices. The mean redshift $\overline{z}$ is given for each redshift bin. Black lines represent the average locus of the star-forming main sequence (parametrised as in the appendix of Sargent et al., 2014) at the $\overline{z}$ of each panel. **b)** Normalised (equal area) stellar mass distributions of spheroid- and disc-dominated SFGs and AGN. Spheroid-dominated SFGs are systematically more massive across the whole studied redshift range. **c)** Normalised distribution of sSFR-offsets from the star-forming main sequence for spheroid- and disc-dominated SFGs. Vertical dashed lines show 0.6 dex offsets above and below the SF MS. The mean sSFR of disc-dominated (spheroid-dominated) SFGs tends to lie above (below) the average MS locus at all redshifts. AGN mainly occupy the quiescent regime below $z \sim 1$.

Table 3.1: Morphological distribution of galaxies before (top) and after (bottom) the exclusion of AGN (see Sect. 3.2.3) from the radio- and infrared-selected samples. Morphological categories are: ellipticals (ZEST type 1); bulge-dominated discs discs (ZEST type 2.0/2.1); disc-dominated discs (ZEST type 2.2/2.3); irregulars (ZEST type 3).

Full sample					
	spheroid-dominated		disc-dominated		Total
	ellipticals	bulge-dominated discs	disc-dominated discs	irregulars	
radio-selected	503	1461	1420	595	3979
IR-selected	157	1305	2098	802	4362
jointly-selected	545	2010	2544	941	6040
Star-forming sample					
	spheroid-dominated		disc-dominated		Total
	ellipticals	bulge-dominated discs	disc-dominated discs	irregulars	
radio-selected	130	905	1248	514	2797
IR-selected	125	1142	1971	727	3965
jointly-selected	168	1409	2323	836	4736

of the jointly-selected sample with a search radius of 0.6 arcsec. 7,973 (65%) sources in the jointly-selected sample (see Sect. 3.2.1) were covered by HST/ACS and satisfy the $i_{AB} = 24$ mag selection limit of the Zurich Structure & Morphology Catalog. 6,723 of these had a counterpart with morphological classification in the morphology catalogue, resulting in an 84 % matching rate. At redshifts $z > 1.5$ the F814W filter starts to sample rest-frame UV (<325 nm) emission, and image signal-to-noise and galaxy angular sizes in general become too small to ensure a robust morphological classification. We thus apply an upper redshift cut of $z = 1.5$ to our sample. Due to the small volume sampled locally by the $\sim$1.6 deg^2 field observed with HST/ACS, we excluded sources with $z < 0.2$. Our final sample contains 6,072 galaxies with morphological distribution as summarized in Table 3.1. Our 'spheroid-dominated' sample includes ZEST types 1 (i.e. predominantly elliptical galaxies) and types 2.0/2.1 (i.e. disc galaxies with a prominent bulge component). Our 'disc-dominated' galaxy sample includes ZEST types 2.2/2.3 (i.e. disc-dominated) spiral/disc galaxies and type 3 (irregular galaxies). We note that both morphological groups contain mainly disc galaxies (see Table 3.1). After the exclusion of AGN (see Sect. 3.2.3), the remaining star-forming sample predominantly lies on the main sequence (MS) of star-forming galaxies (see Fig. 3.1a), consistently with previous studies (e.g. Wuyts et al., 2011), as illustrated by the specific star formation rate (sSFR) distributions in Fig. 3.1c. The stellar masses used here are from multi-band SED modelling with MAGPHYS, and SFR values were derived from the fitted IR

luminosities (see Sect. 3.3.2 for details). We will henceforth qualitatively refer to these morphological categories as '*disc-dominated star-forming galaxies*' and '*spheroid-dominated star-forming galaxies*', respectively. We also note that disc- and spheroid-dominated SFGs have a tendency to lie slightly above and below the main sequence locus, with mean offsets from the MS of 0.06 and −0.10, respectively. Furthermore, spheroid-dominated galaxies on average have higher stellar masses at all redshifts considered here (see Fig. 3.1b). Assuming that the radio and far-IR data used to select our sample are due to star formation alone, our sample is SFR-selected, and in deriving all results reported in the following we also include galaxies that lie below the mass-completeness threshold at $10^{10.4}\,M_{\odot}$ (Laigle et al., 2016). We have ascertained that all our results remain unchanged within $1\,\sigma$ if we restrict the analysis to the mass-complete regime.

Fig. 3.2a shows the relative abundance of spheroid- to disc-dominated SFGs as a function of redshift. Over the redshift range $0.2 < z < 1.5$ the overall disc galaxy population transitions from consisting mainly of disc-dominated objects at high-z to a more even split between morphological types at low redshift (see Fig. 3.2a). Our sample is hence representative of the COSMOS disc galaxy population as a whole for which this trend was already discussed in, e.g., Scarlata et al. (2007) and Oesch et al. (2010).

3.2.3 AGN identification

Our aim is to test the relation between radio synchrotron emission and SFR for different galaxy populations. Identifying and removing potential AGN host galaxies from our sample is hence crucial as both their IR and radio fluxes could include AGN-related contributions. Sources in the jointly-selected catalogue were flagged in D17 as likely AGN hosts if at least one of the following criteria was met:

1. the source shows a power-law like emission in the mid-IR, i.e. its IRAC colours satisfy the criteria of Donley et al. (2012, their eqs. (1) & (2)),
2. an X-ray detection in the combined maps of the Chandra-COSMOS and COSMOS Legacy surveys (Elvis et al., 2009; Civano et al., 2012, 2016; Marchesi et al., 2016) with [0.5-8] keV X-ray luminosity $L_X > 10^{42}$ erg s^{-1} (as in Smolčić et al., 2017a),
3. SED fitting reveals the presence of a statistically significant AGN component based on a χ^2 comparison between fits without and with an AGN contribution of freely variable amplitude (Delvecchio et al., 2014),[2]
4. the source is not detected in any Herschel bands with a signal-to-noise ratio of at least 5, and has red optical rest-frame colours ($M_{NUV} - M_r$) > 3.5 (Smolčić et al., 2017a).

For further details see D17 and Delvecchio et al. (2017). 1,304 galaxies in our sample are flagged as AGN (~38% of spheroid-dominated and ~9% of disc-dominated galaxies) based

[2]A multi-component SED fit was performed using SED3FIT (Berta et al., 2013), publicly available at http://cosmos.astro.caltech.edu/page/other-tools.

on these criteria. The final sample of jointly IR- and radio-selected star-forming galaxies with a morphological classification from the Zurich Structure & Morphology Catalog consists of 4,736 sources. Table 3.1 summarizes how these star-forming galaxies split into distinct morphological classes. We will consider only the star-forming population for the rest of our analysis, unless stated otherwise.

3.3 Results

3.3.1 Derivation of radio luminosities

Radio luminosities were derived using

$$\left(\frac{L_{1.4}}{\mathrm{W\,Hz^{-1}}}\right) = C\,\frac{4\pi}{(1+z)^{(1+\alpha)}}\left(\frac{D_L}{\mathrm{Mpc}}\right)^2\left(\frac{1.4}{3}\right)^{\alpha}\left(\frac{S_3}{\mathrm{mJy}}\right), \tag{3.1}$$

where $L_{1.4}$ is the 1.4 GHz K-corrected radio continuum luminosity, $C = 9.52 \times 10^{15}$ is the conversion factor from $\mathrm{Mpc^2}$ mJy to $\mathrm{W\,Hz^{-1}}$, α is the radio spectral index[3], z is redshift, D_L is the luminosity distance and S_3 is the measured 3 GHz flux. We note that for 45 % of the sources α was directly measured since they had a 1.4 GHz counterpart in the VLA-COSMOS joint catalogue of Schinnerer et al. (2010). For the remaining sources we adopt the average spectral index, $\alpha = -0.7$, measured for galaxies in the VLA-COSMOS 3 GHz survey (Smolčić et al., 2017a). Choosing a steeper average spectral index (e.g. $\alpha = -0.8$) would result in slightly lower IR/radio ratios and a marginally steeper redshift evolution. It would, however, still be consistent with the results presented below within 1 σ and affects both morphological subsamples in the same way. For a full discussion of the systematics arising from a different choice of spectral index see Sect. 4.4.1 in D17.

For IR sources that remain undetected in the 3 GHz map we derive an upper limit on the radio luminosity based on 5 times the local RMS noise level in the map (see D17 for details).

3.3.2 Derivation of IR luminosities, SFRs and stellar masses with SED fitting

Stellar masses provided by the MAGPHYS code were used to physically characterise our samples (see Fig. 3.1), together with star-formation rates based on the IR-luminosity of the best-fit MAGPHYS SED models. In this section we discuss the derivation and robustness of our IR luminosity constraints. When converting IR luminosity to SFR we apply the Kennicutt (1998) scaling factor for a Chabrier (2003) IMF, which is particularly suitable for star-forming galaxies and enables direct comparisons with the previous literature. SFRs calculated with this method are, on average, ~0.2 dex higher than the SFR values returned by MAGPHYS, however, this does not impact qualitatively any of our statements based on SFRs. We further decided to adopt

[3]The radio spectral index is defined as $S_\nu \propto \nu^\alpha$, where S_ν is the flux density at frequency ν.

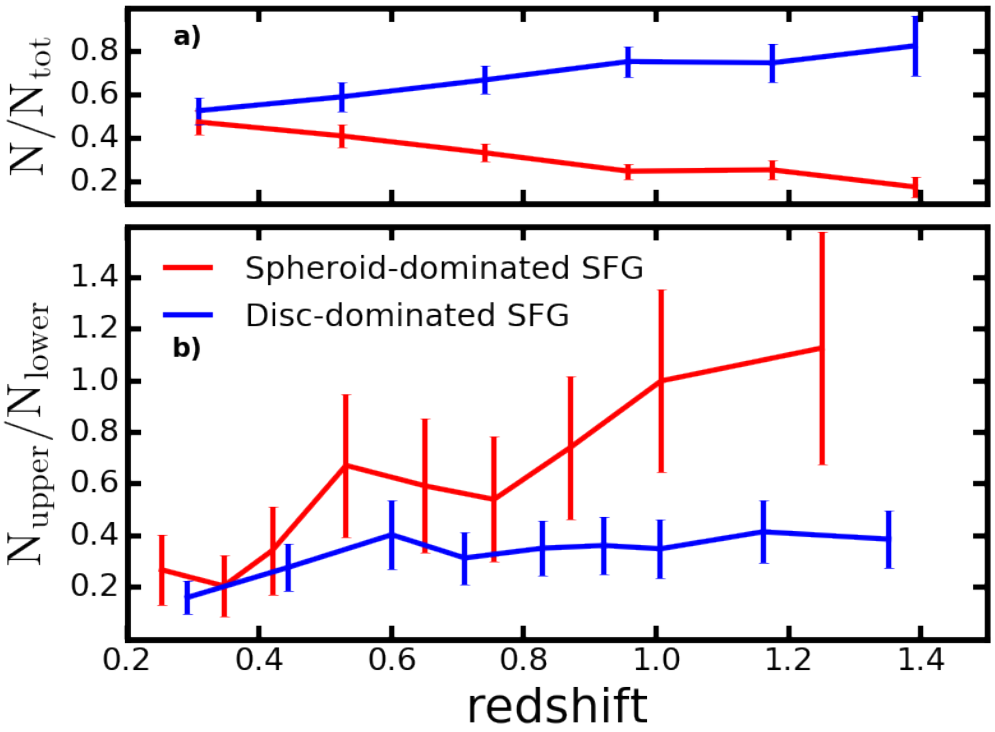

Figure 3.2: **a)** Fractions of spheroid- (red) and disc-dominated (blue) SFGs in our star-forming sample as a function of redshift. **b)** Ratio of the number of IR-undetected ($N_{\rm upper}$) and radio-undetected ($N_{\rm lower}$) galaxies for the spheroid- and disc-dominated SFG samples in the redshift bins used in Sect. 3.3.3. These $N_{\rm upper}$ ($N_{\rm lower}$) objects enter the calculation of the $\overline{q}_{\rm TIR}$ values with upper (lower) limits on the IR/radio ratio, respectively. All error bars reflect 1 σ uncertainties from Poissonian counting statistics. Spheroid-dominated SFGs show an increasing upper limit ratio trend with redshift, whereas disc-dominated systems remain constant out to z $\sim$ 1.5.

$L_{\rm TIR}$ derived SFR values to be consistent with the X-ray stacking analysis outlined in Sect. 3.4.2.

$L_{\rm TIR}$ measurements for IR-selected galaxies

Total IR luminosities ($L_{\rm TIR}$) were derived by integrating the best-fit SED model identified with MAGPHYS (da Cunha et al., 2008) between rest-frame 8 and 1000 μm. Model SEDs were fitted to photometry from the COSMOS2015 catalogue (for details on the data see Laigle et al., 2016). In particular, in the MIR-FIR regime we used the combination of Spitzer MIPS 24 μm, plus Herschel PACS (100 and 160 μm) and SPIRE (250, 350 and 500 μm) flux measurements. For 3 (4) spheroid-dominated (disc-dominated) SFGs we were also able to use 450 and 850 μm JCMT/SCUBA-2 data (Casey et al., 2013).

As described in Sect. 3.2.1, sources with at least one $\geq 5\sigma$ detection in any Herschel band are included in the IR-selected sample. In the jointly-selected sample of star-forming, spheroid-dominated (disc-dominated) sources 85% (80%) are IR-detected (see Table 3.1). Within this IR-selected sample 94% of the galaxies in both morphological sub-samples are detected at 24 μm with $S/N \geq 3$. 67% (69%) of the spheroid-dominated (disc-dominated) galaxies have only one $\geq 5\,\sigma$ Herschel measurement, 18% (13%) have $\geq 5\sigma$ FIR detections in three bands, and only 1% (1%) have $\geq 5\,\sigma$ fluxes across the whole FIR wavelength range. Additionally, 3–5 σ measurements were also included in the fitting process, where available. If, in a given band, no $\geq 3\,\sigma$ photometry was available, we used nominal 3 σ PACS and SPIRE upper limits[4] to constrain the SED fitting, and allowed the fitting algorithm to probe fluxes below these limits via a modified χ^2 calculation[5] following Rowlands et al. (2014). While we could in principle include $\leq 3\,\sigma$ flux measurements in the SED fitting process, we chose the more conservative upper limit approach outlined above as low-S/N fluxes extracted from the map are more susceptible to flux boosting due to source blending. For more details about the fitting technique and its robustness see Sect. 3 of Delvecchio et al. (2017).

$L_{\rm TIR}$ constraints for radio-selected galaxies

We also estimated the total IR luminosity of radio-detected sources with no $\geq 5\,\sigma$ counterparts in the IR-selected sample using shorter wavelength photometry and 3–5 σ measurements or 3 σ upper flux limits from Herschel, as outlined above. While MAGPHYS employs an energy-balance approach – such that one could regard its $L_{\rm TIR}$ estimates as a good proxy for actual measurements – D17 decided to allow also for significantly lower $L_{\rm TIR}$ in these objects, and treated these modelled IR luminosities as upper limits in their analysis. Alternatively, one could consider the best-fit MAGPHYS estimate for $L_{\rm TIR}$ as a direct measurement, even if in cases

[4]These upper limits include both instrumental and confusion noise and are set to 5.0 (100μm), 10.2 (160μm), 8.1 (250μm), 10.7 (350μm), and 15.4 mJy (500μm).

[5]Bands with upper limits contribute zero to the χ^2 if the model SED falls below the upper limit. When the model SED lies above the limiting flux value(s), the excess is included as an additional term in the χ^2 calculation.

with no FIR detection this value is usually quite uncertain. Regarding all these estimates as upper limits or as direct detections are conceptually two end points of a continuum of possible treatments. In Sect. 3.3.3 we therefore present the results from both statistical approaches. To ease comparison with the D17 results, in Fig. 3.3 we only show data from the D17 method, but the fits for the scenario where all $L_{\rm TIR}$ values are considered direct measurements are plotted as well. For now, we only note that this somewhat subjective choice has no qualitative, and only a minimal quantitative impact on our results, due to the fact that generally sources which were not selected at IR wavelengths have $L_{\rm TIR}$-values that lie below the median luminosities in their respective redshift bins. The applied statistical approach thus does not introduce any systematics that could give rise to the differences between disc- and spheroid-dominated SFGs reported below.

As a final test of the robustness of our results, we assessed the impact of poorly fitting SED models by flagging low-quality fits in both the IR- and radio-selected samples. Following the method presented in Appendix B of Smith et al. (2012), we computed the probability of the best-fit model being consistent with our data (p), and identified sources with $p < 1\%$. We found that 15% (17%) of disc-dominated (spheroid-dominated) SFGs have formally poor SED fits, possibly due to e.g. blended FIR photometry, or spurious multi-wavelength source associations. However, excluding these objects from the analysis detailed in Sect. 3.3.3 did not change our results compared to our findings based on the full sample. We hence decided to retain them in order to (a) increase the overall quality of our statistics, (b) not introduce an arbitrary threshold to "clean" our sample and (c) follow the methodology of D17 as closely as possible, in order to enable further insight into the causes of the redshift-evolution of the IRRC found in their study.

3.3.3 Measuring the infrared-radio correlation

The IRRC is usually characterized by the logarithmic ratio, $q_{\rm TIR}$, of the total infrared (8 - 1000 μm; $L_{\rm TIR}$) and 1.4 GHz radio ($L_{1.4}$) luminosities:

$$q_{\rm TIR} \equiv \log\left(\frac{L_{TIR}}{3.75{\times}10^{12}\,{\rm W}}\right) - \log\left(\frac{L_{1.4}}{{\rm W\,Hz^{-1}}}\right). \tag{3.2}$$

We split both the disc- and spheroid-dominated SFG samples into nine redshift bins, each bin containing an equal number of objects. We then carried out double-censored survival analysis (following Schmitt et al., 1993) to calculate the median $q_{\rm TIR}$ ($\overline{q}_{\rm TIR}$) values (and associated 95% confidence intervals) for our two samples in all redshift bins.

Survival analysis reconstructs the underlying distribution assuming that all measurements (i.e. both well-defined values and upper/lower limits) are drawn from the same distribution. If, besides direct detections, only either upper or lower limits occur (i.e. the data are singly censored), the cumulative distribution function (CDF) can be constrained analytically with the Kaplan–Meier product limit estimator (Kaplan and Meier, 1958). However, if both upper

and lower limits are present (i.e. the data are doubly censored), the CDF is computed by an iterative method (as described in Schmitt et al. 1993 and Appendix C of Sargent et al. 2010). Our implementation of the algorithm was considered to have converged once all values of the updated CDF changed by less than 1/1000 of their value in the previous step. The estimated median $\overline{q}_{\rm TIR}$ and its error in each redshift bin was then extracted from these CDFs. We find that propagating the errors of the individual radio and IR luminosities through the analysis by resampling them a hundred times, and recalculating the CDFs, only results in a small additional uncertainty (∼22%) compared to that associated with the CDF estimating method, consistent with the assessment in D17. Thus, the errors from survival analysis dominate the error budget of $\overline{q}_{\rm TIR}$ values.

The $\overline{q}_{\rm TIR}$ values calculated with survival analysis as a function of redshift are shown in Fig. 3.3a. At a qualitative level, the different redshift trends of the relative fraction of upper and lower limits observed for spheroid- and disc-dominated SFGs (see Fig. 3.2b) is already a clear indication of systematically different evolution of these two morphologically distinct populations. For a quantitative confirmation, we fit the following evolutionary function to the $\overline{q}_{\rm TIR}$ measurements in all redshift bins:

$$\overline{q}_{\rm TIR} = a(1+z)^k, \tag{3.3}$$

where a and k are free parameters. Errors on a and k were estimated by resampling the $\overline{q}_{\rm TIR}$ values using their uncertainties derived by survival analysis and refitting the newly generated datasets 10,000 times, allowing a measurement of the $1\,\sigma$ confidence intervals. To anchor the fit, we included a $z = 0$ data point based on the sample of Bell (2003) containing structural information, which we split into spheroid- and disc-dominated SFGs following the correspondence between morphological types in the Zurich Structure & Morphology Catalog and Hubble type described previously in Sect. 3.2.2. Thus, 33 galaxies in the Bell, 2003 sample with RC3 classification S0, S0a, Sa, Sab and Sb were assigned to the category 'spheroid-dominated SFGs', and 80 RC3 types Sbc, Sc, Scd, Sd and Irr are considered disc-dominated. Omitting the local $q_{\rm TIR}$ measurements does not qualitatively change our results (see Fig. 3.3b).

We find that the median IR/radio ratios of spheroid-dominated SFGs follow a declining trend with a power law index of $k = -0.186\pm0.015$ (or $k = -0.160\pm0.014$ when all $L_{\rm TIR}$ values are treated as direct measurements[6]), while for disc-dominated SFGs the redshift-evolution is minimal out to $z = 1.5$ with $k = -0.037\pm0.012$ (or $k = -0.044\pm0.010$ for our alternative $L_{\rm TIR}$ treatment), as shown in Fig. 3.3a. The difference between these two evolutionary trends is

[6]In practice, considering all $L_{\rm TIR}$ estimates as direct detections only increases $\overline{q}_{\rm TIR}$ values minimally. This is due to the fact that the majority of the sources which are not IR-selected have IR/radio ratio constraints that lie below the $\overline{q}_{\rm TIR}$ of their redshift bins. However, since these sources constitute a larger fraction of the population at higher redshifts (see Fig. 3.2b), the consequently slightly larger $\overline{q}_{\rm TIR}$ values lead to a $1.3\,\sigma$ ($0.5\,\sigma$) shallower $\overline{q}_{\rm TIR}$(z) relation for spheroid-dominated (disc-dominated) SFGs.

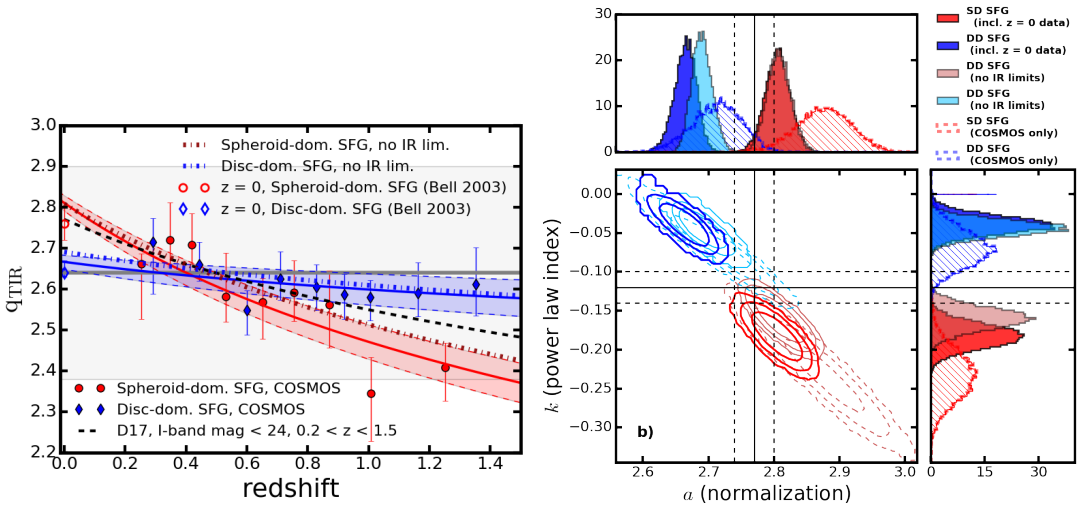

Figure 3.3: **a)** Redshift evolution of the infrared-radio correlation, parametrized by the median IR/radio ratio $q_{\rm TIR}$, for disc- and spheroid-dominated star-forming galaxies (blue and red symbols, respectively). The $\overline{q}_{\rm TIR}$ values for COSMOS galaxies at z > 0.2 (filled data points) were calculated using double-censored survival analysis. The local $z = 0$ measurements (open symbols) are based on a morphologically-selected sub-set of the Bell (2003) sample. Shaded regions bordered by dashed lines show the upper and lower limits of the 1 σ confidence interval of the fit. Dot-dashed lines are fits to $\overline{q}_{\rm TIR}$ values derived by considering all $L_{\rm TIR}$ estimates as direct detections. The black dashed line is the evolutionary trend found for SFGs with I-band magnitude < 24 in the jointly-selected sample of D17 in the redshift range of 0.2 < z < 1.5. These cuts were imposed in order to match the selection criteria of our morphologically-selected subsamples. The dark grey horizontal line represents the local median IR/radio ratio measured by Bell (2003), the shaded grey region its $\sim$ 0.3 scatter. **b)** 2D histogram of the parameters fitted for an evolutionary trend (eq. 3.3) for star-forming late and spheroid-dominated galaxies in our sample, shown in blue and red, respectively. Light coloured contours and histograms show the outcome of our analysis when we treat all $L_{\rm TIR}$ values as direct measurements. Hatched histograms and dashed contours are the results of fits that were carried excluding the local $q_{\rm TIR}$ values from Bell (2003). Contours enclose the 3, 2 and 1 σ confidence intervals of each distribution. The solid black lines are the fitted values for the whole star-forming population in the COSMOS field from D17. Dashed black lines represent the 1 σ confidence interval of this fit.

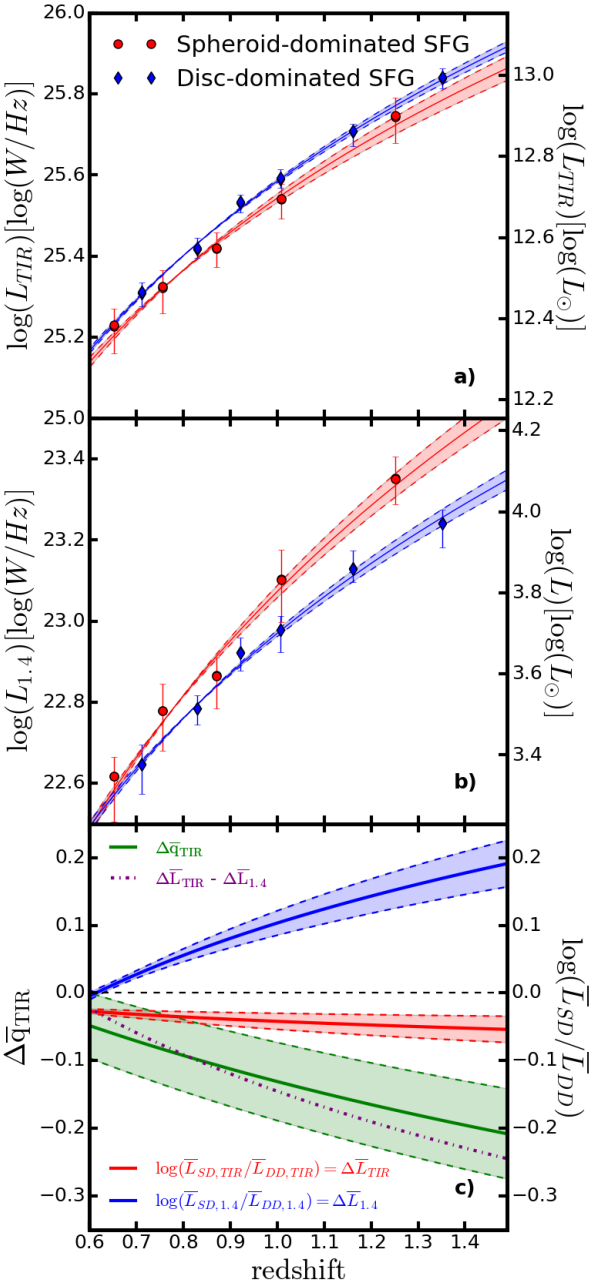

Figure 3.4: Median total infrared (**a**) and median 1.4 GHz luminosities (**b**) in the redshift range where $\overline{q}_{\rm TIR}$ values diverge for spheroid- and disc-dominated galaxies in our sample shown in blue and red, respectively. **c)** Decomposition of the measured $\overline{q}_{\rm TIR}(z)$ difference between spheroid- and disc dominated SFGs. The green line represents the directly measured $q_{\rm TIR}(z)$ offset between spheroid- and disc-dominated SFGs from the fitted $\overline{q}_{\rm TIR}(z)$ curves in Fig. 3.3 as calculated by Eq. 3.5. Blue and red lines are the differences in radio- and total IR-luminosities, respectively, derived from single censored survival analyses, as seen on the top two panels and Eq. 3.6. The purple line is the difference of these two trends, which also gives $\Delta\overline{q}_{\rm TIR}(z)$ (see Eq. 3.7.). The shaded 1 σ confidence intervals (in appropriate colours for their corresponding lines) are calculated by propagating the errors on the previously fitted trends. It is clear that the main contributor to the different $\overline{q}_{\rm TIR}(z)$ evolution is the increasing relative radio excess of spheroid-dominated SFGs towards high redshifts.

significant at the 7.7 σ level (5.0 σ if we exclude the $z = 0$ measurements; 6.6 σ with all $L_{\rm TIR}$ estimates as direct detections and including the local $\overline{q}_{\rm TIR}$ values) as shown in Fig. 3.3b). In Fig. 3.3a we also show with a dashed line the best-fit evolution of $\overline{q}_{\rm TIR}$ for all star-forming galaxies (i.e. including all morphological types) that satisfy our selection criteria $i_{\rm AB} \leq 24$ and $0.2 < z < 1.5$. With an evolutionary power-law index $k = -0.12 \pm 0.02$ it lies between the best fit relations for the spheroid and disc-dominated SFGs, as expected, and is slightly shallower than the evolutionary trend ($k = -0.19 \pm 0.01$) reported by D17 for the full parent sample. The main reason for difference to the measurement in D17 is that we have restricted our fit to galaxies at $0.2 < z < 1.5$, while D17 consider objects across all $z \lesssim 6$.

3.3.4 Differential evolution of average IR and radio brightness of spheroid- and disc-dominated galaxies

To determine the main cause of the observed difference between spheroid- and disc-dominated star-forming galaxies, we now attempt to express the evolution of the $\overline{q}_{\rm TIR}$ value for both populations in terms of the relative evolution of their median IR and radio luminosities. To this end, we performed single-censored survival analysis on the luminosities and luminosity upper limits to constrain the according medians for the spheroid- and disc-dominated samples in all redshift bins. The redshift-evolution of the luminosities is best fit by a

$$\log(\overline{L}) = bz^{l} \tag{3.4}$$

model, where $\overline{L}$ is either the median rest-frame 1.4 GHz radio luminosity, or the median IR luminosity for a given redshift bin and sample. b and l are free parameters. The measured luminosity evolutions and the best-fit combinations of model parameters b and l for spheroid- and disc-dominated star-forming galaxies are shown in Fig. 3.4. Radio luminosities of spheroid-dominated SFGs show an excess compared to disc-dominated SFGs above z ~ 0.8. Their total IR luminosities have a smaller, but still significant deficit starting around the same redshift.

We define the offset between the median IR/radio ratios of spheroid- and disc-dominated SFGs as:

$$\Delta\overline{q}_{\rm TIR}(z) \equiv \overline{q}_{\rm TIR,SD}(z) - \overline{q}_{\rm TIR,DD}(z), \tag{3.5}$$

where $\overline{q}_{\rm TIR,SD}(z)$ and $\overline{q}_{\rm TIR,DD}(z)$ are the $\overline{q}_{\rm TIR}(z)$ sample median trends fitted between $0 < z < 1.5$ for spheroid- and disc-dominated SFGs, respectively. We also define:

$$\Delta\overline{L}_{\{1.4,\rm TIR\}}(z) \equiv \log \overline{L}_{\{1.4,\rm TIR\},\,SD}(z) - \log \overline{L}_{\{1.4,\rm TIR\},\,DD}(z), \tag{3.6}$$

where $\overline{L}_{\{1.4,\rm TIR\},\,SD}$ is either the median 1.4 GHz or IR luminosity of spheroid-dominated SFGs and $\overline{L}_{\{1.4,\rm TIR\},\,DD}$ is the corresponding median luminosity for disc-dominated SFGs. Then from Eq. 3.2 and Eq. 3.6 we see that:

$$\Delta\overline{q}_{\rm TIR}(z) = \Delta\overline{L}_{\rm TIR}(z) - \Delta\overline{L}_{1.4}(z). \tag{3.7}$$

This decomposition of the measured $\overline{q}_{\rm TIR}(z)$ difference between spheroid- and disc dominated SFGs is shown in Fig. 3.4. It suggests that the main cause of the different observed $q_{\rm TIR}$ trends is an increasing radio excess in spheroid-dominated SFGs compared to disc-dominated SFGs above $z \sim 0.8$, with contribution from a smaller IR deficit of spheroid-dominated SFGs in the same redshift range. This hints at additional AGN-related radio emission, possibly from small-scale jet-activity at higher redshifts in bulge-dominated systems. We will explore this point further in Sect. 3.4.2.

3.4 Discussion

3.4.1 Minimal evolution of the IR-radio correlation for disc-dominated star-forming galaxies

As shown in Fig. 3.2b, spheroid- and disc-dominated SFGs show different censoring patterns (i.e. different balance of direct measurements and upper/lower limits) for their IR/radio ratios above $z \sim 0.8$. This in itself already points to a differential evolution of sample medians $\overline{q}_{\rm TIR}$ towards higher redshifts. As found by doubly-censored survival analysis, the radio-infrared ratios of the disc-dominated SFG sample show virtually no evolution out to $z = 1.5$ and are in almost all redshift bins consistent with the locally measured median $q_{\rm TIR}$ value of Bell (2003) (Fig. 3.3). The fact that the median IR/radio ratio is nearly constant for that class of galaxies which effectively represents the 'proto-typical' (i.e. disc-like) star-forming object, suggests that – when applied to purely star-forming systems/regions – radio synchrotron emission traces star formation in the same way over the entire redshift range $0 < z < 1.5$. We note that, above $z = 1$, our morphological selection may be somewhat biased towards classification into disc-dominated SFGs as resolution effects and decreasing pixel signal-to-noise in HST images can reduce the measured concentration index (and hence bulge-to-disc ratio) of the more distant galaxies. As a consequence, we expect that, if anything, the disc-dominated SFG sample presumably contains some galaxies which would be classified as spheroid-dominated SFGs in noise-free HST images, rather than the other way around. If there is indeed a systematic difference between the IR/radio ratios $q_{\rm TIR}$ of spheroid and disc-dominated systems as suggested by our analysis in Sect. 3.3.3, correcting for this morphological classification bias would further flatten the evolutionary trend for the disc-dominated population. We note that removing the $3\,\sigma$ radio excess outliers from the disc-dominated sample also flattens their $\overline{q}_{\rm TIR}(z)$ trend further ($k = -0.02 \pm 0.02$). The flagging and removal of outlier $q_{\rm TIR}$ values are described in Sect. 3.4.2. Starburst objects (i.e. $\log({\rm sSFR}/{\rm sSFR}_{\rm MS}) > 0.6$) are more abundant among disc-dominated systems (as seen in Fig. 3.1a). However, removing them from both samples does not change our results. In fact, we note that there is no significant change in $\overline{q}_{\rm TIR}$ as a function of MS offset across the entire redshift range (in agreement with the findings of Magnelli et al., 2015).

Lacki and Thompson 2010 defined a 'critical redshift' ($z_{\rm crit}$) for their models, by which the radio luminosity is suppressed by a factor of 3 compared to $z = 0$ due to increasing inverse Compton losses off the cosmic microwave background (CMB). This would lead to an increase in $q_{\rm TIR}$ of ~0.5 dex. In their model $z_{\rm crit}$ is ultimately determined by the SFR surface density ($\Sigma_{\rm SFR}$) of a galaxy. In order to compare our findings to theoretical predictions, we derived the median $\Sigma_{\rm SFR}$ of our SFG sample using optical half-light radii from the Zurich Structure & Morphology Catalog and SFRs calculated from the total IR luminosities (see Sect 3.3.2 for details). We note that it is improbable that this approach should strongly overestimate $\Sigma_{\rm SFR}$ as, e.g., Nelson et al. (2016) and Rujopakarn et al. (2016) find approximately similar sizes for SF activity and stellar mass in distant SFGs, and especially since HST/ACS F814W filter samples blue rest-frame emission at $z > 1$. Given that the bulk of our galaxies in both samples lie on the SF MS (see Fig. 3.1a), we convert $\Sigma_{\rm SFR}$ into $z_{\rm crit}$ using the formula for normal galaxies from the simplest model[7] in Lacki and Thompson (2010). The median $\Sigma_{\rm SFR}$ of ~0.08 $M_\odot$ kpc^{-2} yr^{-1} derived for our disc-dominated SFGs yields $z_{\rm crit} \sim 2.2$, i.e. Lacki and Thompson (2010) do not predict a significant change in $\overline{q}_{\rm TIR}$ for objects of this $\Sigma_{\rm SFR}$ across our redshift range, in agreement with our data. However, their model finds a very similar $z_{\rm crit}$ of 2.3 for spheroid-dominated SFGs due to their similar median $\Sigma_{\rm SFR}$ of ~0.09 $M_\odot$ kpc^{-2} yr^{-1}, which in this case is in discrepancy with the decreasing $\overline{q}_{\rm TIR}(z)$ we find. It is interesting to note that, should the sizes of star-forming regions be significantly smaller than assumed here, as suggested by the 10 GHz imaging results in Murphy et al. (2017), the correspondingly higher $\Sigma_{\rm SFR}$ would push $z_{\rm crit}$ to even higher redshifts.

3.4.2 Differential redshift-evolution of $\overline{q}_{\rm TIR}$ depending on disc galaxy type – possible explanations

If we omit disc galaxies with intermediate bulge-to-disc ratios (i.e. ZEST type 2.1 and 2.2) from the spheroid- and disc-dominated SFG samples, their $\overline{q}_{\rm TIR}(z)$ power-law indices are in even stronger contrast (k= −0.22±0.06 and k= 0.03±0.02, respectively). In the following section we will investigate possible causes of this morphology-dependent change in their evolutionary trends.

Low-level AGN contamination

The lower $\overline{q}_{\rm TIR}$ values of spheroid-dominated SFGs at redshifts $z \gtrsim 0.8$ are mainly due to their relative radio excess compared to disc-dominated SFGs at high z (Fig. 3.4). This could be the result of a radio component related to weak AGN activity in bulgy SFGs. We note that, as shown in Sect. 3.2.3, a four times higher fraction of systems were flagged and removed as

[7]Their formulae for different starburst models, SFR laws and feedback mechanisms predict higher $z_{\rm crit}$ values for the same $\Sigma_{\rm SFR}$, hence the $z_{\rm crit}$ values given in text should be considered as lower limits. However, a higher $z_{\rm crit}$ would qualitatively not change our conclusions.

AGN hosts in the spheroid-dominated sample, compared to the disc-dominated sample. If the measured radio excess of spheroid-dominated disc galaxies were entirely due to residual AGN activity (i.e. if the SF-related radio and infrared emission from these objects followed the local IRRC as is observed for the disc-dominated systems), then we would infer that at $z \sim 1.5$ on average $\sim 60\%$ of their total observed radio emission is contributed by AGN-related processes (see Fig. 3.4.), which escaped detection by the full set of standard AGN identification methods described in Sect. 3.2.3.

Alternatively, the additional average radio emission could be the consequence of a relatively small number of strong radio excess sources that appear in our data as outliers in the $q_{\rm TIR}$ distribution in each redshift bin. The CDFs in each bin derived by survival analysis allow us to select and remove such sources from each of our sub-samples. Assuming that the $q_{\rm TIR}$ distribution is well described by a Gaussian distribution, we computed the σ of the distribution, and removed $3\,\sigma$ outliers below the median in all our redshift bins. We then repeated our survival analysis on these "cleaned" samples. The resulting $\overline{q}_{\rm TIR}$ trends are consistent with the ones measured on the full sample within $1\,\sigma$. In fact, applying a more stringent $2\,\sigma$ lower $q_{\rm TIR}$ cut, where σ was derived only using $q_{\rm TIR}$ values higher than the median, yielded the same slopes for the trends. This implies that the measured evolutions of the $\overline{q}_{\rm TIR}$ values are not driven by low $q_{\rm TIR}$ outliers for both the spheroid- and disc-dominated SFG samples.

To further investigate potential residual AGN contamination of our SFG samples we searched for small scale radio emission associated with our galaxies by cross-matching the spheroid- and disc-dominated SFG samples at $z > 0.8$, where $\overline{q}_{\rm TIR}$ trends start to diverge, with the 1.4 GHz VLBA-COSMOS catalogue (Herrera-Ruiz, submitted., l0 μJy sensitivity in the central part of the field). We found 9 (1.6%) and 15 (0.9%) counterparts for spheroid- and disc-dominated SFGs, respectively. This rules out any significant contamination from sources with $L_{1.4} > 1 - 6{\times}10^{23}$ W Hz^{-1} radio cores (at $z = 0.8$ and 1.5, respectively) in both samples at this redshift range. However, if the 0.1 – 0.2 dex excess radio luminosity is due to small-scale AGN-related emission in spheroid-dominated galaxies at z > 1 (as seen on Fig. 3.4.), then such components fall below the detection limit of the VLBA sample by a factor of ~ 3. Thus the low matching fraction does not rule out the possibility of a non-SF related radio component in the bulge of spheroid-dominated galaxies.

Unobscured AGN activity could also manifest itself as centrally concentrated emission in our high-resolution, rest-frame optical HST images. If this were preferentially the case for SFGs classified as spheroid-dominated, we might expect a stronger evolution of average concentration indices (CIs) for these systems at $z \gtrsim 0.8$, compared to disc-dominated SFGs. Using the Zurich Structure & Morphology Catalog we calculated the median CIs of the spheroid- and disc-dominated SFG samples, but find that the median CI of spheroid-dominated SFGs is consistently ~20% larger than that of disc-dominated SFGs across the whole redshift range. This lack of differential evolution between the two samples provides further evidence against an increasing number of highly-concentrated spheroid-dominated systems, that could

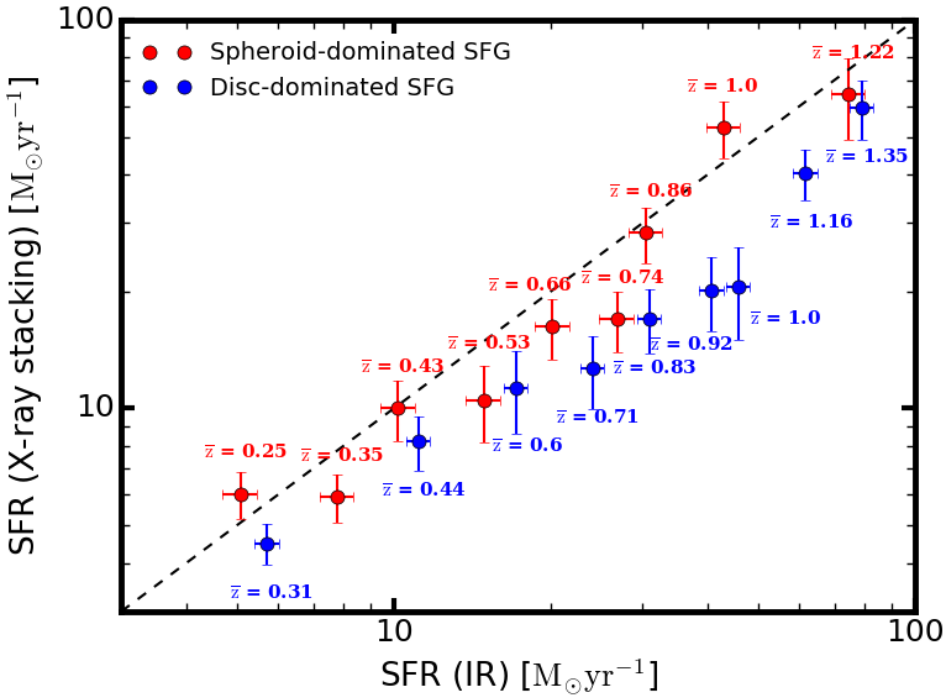

Figure 3.5: A comparison of star formation rates derived from X-ray stacking and Herschel based IR flux averaging for both SFG samples. Dashed line represents the 1:1 relation.

be linked to higher AGN contamination.

As mentioned in Sect. 3.2.3., none of our SFGs have X-ray luminosities (L_X) > 10^{42} erg s^{-1}. As a final test to gauge AGN contamination at high-redshifts, we carried out X-ray flux stacking in both the spheroid- and disc-dominated SFG samples for comparison. We used CSTACK[8], a publicly-available tool for stacking, to stack soft ([0.5 – 2] keV) and hard band ([2 – 8] keV) Chandra images of our sources in each redshift bin. The resulting stacked count rates were converted to X-ray luminosities with a 1.4 slope power law spectrum, as found for the X-ray background (e.g. Gilli et al., 2007). We then converted the X-ray luminosities to SFRs with the calibration given by Symeonidis et al. (2014). In the same redshift bins we calculated average SFRs from IR luminosities, using the simple conversion of Kennicutt (1998) with a Chabrier (2003) IMF in order to facilitate the comparison with other SFR estimates adopted in the literature (see Sect. 3.3.2). These are less sensitive to AGN related emission, thus provide a reference for finding X-ray excess in our samples. Fig. 3.5. shows the comparison between X-ray and IR-derived SFRs for both spheroid- and disc-dominated SFGs. We found a small systematic X-ray deficit in the disc-dominated SFG sample, most likely due to the fact that they are not representative of the galaxy population used for the calibration of the SFR_X - SFR_{IR} relation in Symeonidis et al. (2014). If we were to rescale it to better fit our disc-dominated SFGs, the spheroid-dominated sample above $z = 0.8$ would end up having a ~0.2 dex X-ray

[8]Written by Takamitsu Miyaji, and available at http://lambic.astrosen.unam.mx/cstack

excess. Considering that the SFR_X - SFR_{IR} calibration also has a ~0.2 dex scatter, it would still not suggest a strong X-ray excess in this redshift range.

In summary, we have found no conclusive signs of a higher AGN contamination in our spheroid-dominated SFG sample above redshift $\sim$ 1, however, with available data we cannot exclude this scenario. Should the excess radio emission of spheroid-dominated SFGs be at least partly AGN-related, it could be viewed as the indirect signature of the build-up of black hole-bulge mass correlation at small growth rates (see also Mullaney et al., 2012).

Other contributing factors

If the radio excess observed for $z > 0.8$ spheroid-dominated SFGs is not due to a significant AGN contamination, another possibility is a flattening radio spectral slope trend with redshift. A constant $\alpha = -0.7$, would overestimate the rest-frame 1.4 GHz luminosity derived from 3 GHz fluxes (see Eq. 3.1). Using the radio excess curve for spheroid-dominated systems in Fig. 3.4 we calculate that the median radio spectral index of spheroid-dominated SFGs would have to increase from $\alpha = -0.7$ at $z = 0.8$ to $\alpha = -0.45$ at $z = 1.5$ in order to cancel the radio excess and produce $\overline{q}_{TIR}$ values consistent with the locally measured one at all redshifts. This is inconsistent both with the trend for decreasing 1–3 GHz spectral index values reported by D17, as well as with the median radio spectral slopes of disc- and spheroid-dominated systems we actually measure, and which are consistent with each other across the entire redshift range. On the other hand, Murphy et al. (2017) find evidence for a flatter ($\alpha > -0.6$) average radio spectral index over the wider frequency baseline 1–10 GHz. Given the large spectral index dispersion of 0.35 dex found by Murphy et al. (2017) it is thus possible that, at least for some galaxies, spectral indices may approach values required for reducing the measured radio excess. However, we also note that, while restricted to low-redshift samples (e.g. Niklas et al., 1997 and Marvil et al., 2015), previous studies do not find evidence for differently shaped radio spectra for star-forming galaxies with different optical morphologies.

While the overall differential evolution implied by the fitted best fit relations (Eq. 3.3.) is significant at the 7.5 σ level, the actual data underpinning this trend does not display as smooth an evolution as the best-fit power law. This could be interpreted as a signature of multiple different factors being at play. At low redshifts ($z < 0.3$), using local $\overline{q}_{TIR}$ estimates from Bell (2003), we find that spheroid-dominated systems have higher $\overline{q}_{TIR}$ values than disc-dominated galaxies, in qualitative agreement with the findings of, e.g., Nyland et al. (2017). This could arise from an IR-excess related to enhanced cirrus emission in spheroid-dominated systems linked to old stellar populations rather than SF activity. As a test, we calculated median cold and warm dust component temperatures fitted with MAGPHYS in each redshift bin. During the SED fitting MAGPHYS decomposes the FIR part of the SED into a warm component, related to birth clouds where SF activity occurs, and a cold component, representing the ISM heated by an on average older stellar population. We found that the cold component of spheroid-dominated systems is marginally warmer (by 1 K or ~ 4%) than in disc-dominated SFGs below $z = 0.7$.

However, calculating median infrared/radio ratios using the cold or the warm component yields redshift evolution slopes consistent within 1 σ with $\overline{q}_{\rm TIR}$ slopes, further suggesting that the difference is mainly driven by radio emission rather than a changing balance between the cold and warm (i.e. star-formation related) dust emission in spheroid- and disc-dominated SFGs. We caution that, due to low detection rates 350 and 500 μm, detecting a cold (dust temperature 20 K as found by e.g. Bianchi et al., 2017) cirrus component is challenging with our data, in particular at $z > 1$. While it is thus possible that such a component could be missed (and IR-luminosities thus underestimated), widespread occurrence of cirrus emission strong enough to flatten the $\overline{q}_{\rm TIR}(z)$ trend for spheroid-dominated SFGs would presumably result in larger SPIRE detection fractions for this population. This is, however, not what we observe, such that it is unlikely that missed cirrus emission is responsible for the observed difference between the evolutionary trends measured for spheroid- and disc-dominated SFGs in Sect. 3.3.3.

In conclusion, one could envisage a scenario where a combination of excess IR due to cirrus emission at low redshifts and an AGN contribution at high redshifts (with a transition around $z \sim 0.8$) jointly drive the $\overline{q}_{\rm TIR}$ trend for the spheroid-dominated SFGs. Regardless of the physical processes regulating the $\overline{q}_{\rm TIR}$ evolution, from an empirical point of view, the observed differential trends found in this study highlight the importance of ancillary data, such as morphological information, for the process of converting observed radio fluxes into SFR measurements, especially for galaxies at redshifts above 1. While radio emission apparently traces SFR much in the same way at $z \sim 1$ as it does at $z \sim 0$ (as suggested by the near constancy of the median IR/radio ratios of massive, disc-dominated SFGs across this redshift range), it may nevertheless be more appropriate to adopt a recipe involving a redshift-dependent IR/radio ratio $\overline{q}_{\rm TIR}(z)$ (see, e.g., eq. 4 in D17)

$$SFR \propto 10^{\overline{q}_{\rm TIR}(z)} L_{1.4} \tag{3.8}$$

when dealing with a purely SF-selected sample, since this kind of prescription can statistically account for the average fraction of radio emission unrelated to ongoing SF activity. However, we find that this correction is preferentially needed in spheroid-dominated systems, implying that combining morphological indicators with radio data can increase the accuracy of radio-based SFR estimates when this additional information is available.

3.5 Summary

With the combination of infrared data from Herschel Space Observatory and new, high sensitivity JVLA 3 GHz observations in the COSMOS field, and morphological classification from the Zurich Structure & Morphology Catalog, we studied the redshift dependence of the infrared/radio ratio of spheroid- and disc-dominated SFGs on the star-forming main sequence out to a redshift of 1.5. We found that the median IR/radio flux ratio $\overline{q}_{\rm TIR}$ of disc-dominated galax-

ies shows virtually no evolution, in agreement with e.g. the model of Lacki and Thompson (2010). This suggests, that calibrations of radio luminosity as a SFR tracer based on local galaxies remain valid out to $z \sim 1.5$ for 'pure' star-forming systems. It also implies that disc-dominated galaxies may be the most suitable laboratories for studying the evolution and physics of the infrared-radio correlation, as in these systems radio and IR emission are linked to star formation in the most straightforward way. Spheroid-dominated SFGs, on the other hand display a decreasing trend with a slope of -0.19 ± 0.02, consistent with most recent literature on the evolution of the IRRC for star-forming galaxies in general. A comparison of total infrared and radio luminosities between these two morphologically distinct sub-samples of SFGs revealed that the low q_{TIR} values above $z \sim 0.8$ for spheroid-dominated SFGs are mainly the result of their $\sim$10–60% radio luminosity excess relative to disc-dominated systems. This could hint at AGN activity at radio frequencies that did not reveal itself clearly in standard AGN diagnostics, which were initially used to identify and remove AGNs from both samples.

The fact that morphologically distinct samples of galaxies follow different redshift trends implies that future high-resolution and high-sensitivity surveys aiming to use radio continuum observations as a star formation tracer will strongly benefit from ancillary morphological data for the final analysis step of converting radio luminosities into accurate SFR estimates. Using a more nuanced calibration of this kind will be possible for high-redshift studies building on the synergies between radio surveys with, e.g., the Square Kilometre Array and high-resolution optical information obtained with Euclid (Ciliegi and Bardelli, 2015). From a theoretical perspective it highlights the complex interplay of physical processes contributing to galaxy-integrated measurements and the need to disentangle these for a more thorough understanding of the IRRC.

Contributions

MTS supplied the survival analysis code. IRRC catalogue was assembled by JD. IR SED fits, AGN identification and X-ray stacking analysis were done by ID. Radio catalogues were constructed by MN and VS. COSMOS VLBI data were provided by NHR and EM. All co-authors contributed comments and advice.

Chapter 4

Selection effects and a new measurement of the infrared-radio correlation in the low redshift Universe

This paper is being prepared for publication in Molnár et al., 2018, Monthly Notices of Royal Astronomical Society.

Current co-authors are:

Mark T. Sargent, Sarah Leslie, Eva Schinnerer, Benjamin Magnelli

Abstract

The infrared-radio correlation (IRRC) forms the most commonly used basis for the radio flux – star formation rate (SFR) calibration. Its dependencies on various galaxy properties (such as luminosity, dust temperature, metallicity, environment, and morphology) have been investigated in order to improve the calibration and gain insights into the physical processes regulating it. The redshift dependence of the IRRC is also crucial for increasing the accuracy of SFRs from future deep radio surveys with e.g. the SKA and its precursors. However, recent studies have difficulties reconciling high-z infrared-radio ratios with locally measured values. Since the IRRC's canonical local studies by Yun et al. (2001) and Bell (2003), new, more sensitive data became available with better photometric coverage, thus it is timely to revisit local studies which future IRRC measurements use as reference points. We compiled a catalogue of local galaxies with total infrared and 1.4 GHz radio luminosities, that is five times larger and four times deeper than the previously largest one by Yun et al. (2001). We demonstrate the effect of "asymmetric" IR-

and radio flux sensitivities on the measured median IR-radio ratio. Based on this, we apply flux cuts to create an unbiased set of galaxies and measure the main IRRC properties on this sample. We find a median infrared-radio ratio, $\overline{q}_{\rm TIR}$, of 2.64 (2.61) for star-forming galaxies (AGN) with a scatter of 0.21 (0.26). We show that $\overline{q}_{\rm TIR}$ correlates with radio power in both star-forming galaxies and AGN. With further ancillary data, this publicly available catalogue provides a database for more detailed follow-up analyses of the IRRC.

4.1 Introduction

Total infrared and radio luminosities are observed to be closely related in galaxies (van der Kruit, 1971, 1973; de Jong et al., 1985; Helou et al., 1985; Condon, 1992; Yun et al., 2001). Since infrared (IR) emission dominantly arises from star formation (SF) activity, this so-called infrared-radio correlation (IRRC) implies that radio power in most galaxies is also related to SF. Due to sensitivity limitations both radio and IR surveys traditionally could only detect the same bright sources, therefore the IRRC was primarily used to set up a radio-based star formation rate (SFR) calibration instead of comparing radio fluxes to other SFR tracers.

The largest infrared–radio ratio measurement in the local Universe was carried out by Yun et al. (2001). They used Infrared Astronomical Satellite (IRAS; Neugebauer et al., 1984) data to constrain IR luminosities with two photometric points at 60 and 100 μm, and radio fluxes observed by the NRAO VLA Sky Survey (NVSS; Condon et al., 1998) at 20 cm for 1,809 60 μm selected galaxies, to derive a mean infrared–radio ratio, determine the scatter of the relation, and provide a robust radio – SFR recipe. They found some evidence for non-linearity in the low luminosity ($L_{60\mu m} \leq 10^9 L_{\odot}$) regime. Bell (2003) studied a diverse sample of 169 local galaxies with far-ultraviolet (FUV), optical, IR and radio luminosities to explore the physical processes regulating the IRRC. The overall IRRC properties proved to be broadly consistent with the findings of Yun et al. (2001). With new evidence for non-linearity at low IR luminosities, Bell (2003) provided a new, luminosity dependent radio – SFR calibration. Since then studies typically focus on the IRRC in specific types of galaxies (e.g. Qiu et al., 2017), the IR-radio ratio's redshift (e.g. Sargent et al., 2010; Ivison et al., 2010; Mao et al., 2011; Delhaize et al., 2017; Calistro Rivera et al., 2017) or stellar mass – SFR plane dependence (Magnelli et al., 2015), etc.

With the upcoming new generation of radio telescopes (such as the Low Frequency Array; Square Kilometre Array and its precursors, ASKAP and MeerKAT; the recently upgraded Very Large Array, etc.), deeper and wider than before radio surveys will provide a more complete census of star-forming radio galaxies both in the local and more distant Universe. To make full of use of the unprecedented high-quality data, a more refined understanding of the radio – SFR calibration is needed. Since the Yun et al. (2001) and Bell (2003) works were published, more sensitive radio and IR data, and better overall IR photometric coverage have become

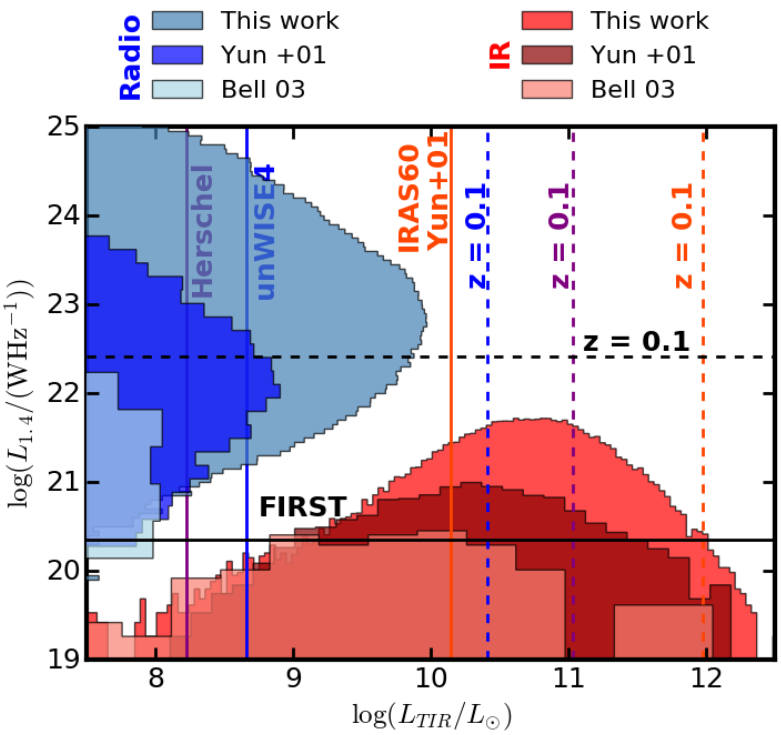

Figure 4.1: Total infrared and 1.4 GHz radio luminosity distributions of the Yun et al. (2001) and Bell (2003) samples in comparison to our catalogue presented here (for details about the calculations of radio and IR luminosities, see Sect. 4.2.2). FIR luminosities in the Yun et al. (2001) catalogue were rescaled to TIR with the average ~0.33 dex offset between FIR and TIR luminosities measured in our sample. Solid (dashed) lines show the various luminosity limits at z = 0.01 (z = 0.1) derived from Fig. 4.2. Number counts are on a logarithmic scale to ease comparison between the samples.

available. Furthermore, as discussed in Sargent et al. (2010), IR- and radio-selection effects can bias median IR-radio ratio measurements, which warrants a more careful approach than traditionally done.

This work presents a ~5 times larger and ~4 times deeper dataset than the one used in Yun et al. (2001), aiming to provide a more precise measurement of the IRRC than previously possible. Fig. 4.1 shows a comparison of infrared and radio luminosities in the catalogues of Bell (2003), Yun et al. (2001) and our work. It is apparent, that we have substantially more $\geqslant$ 21 log(W/Hz) ($\geqslant$ 9.5 log($M_{\odot}$)) radio detected (IR detected) sources, however we could not increase low luminosity number counts. The primary reason for this, is the ~ 2.6 times larger area covered by Yun et al. (2001). Our catalogue with IR and radio luminosity measurements is going to be publicly available to support follow-up studies investigating the local IRRC's dependence on various galaxy parameters and thus gaining insights into the physics regulating the correlation. In Sect. 4.2 we describe the archival data products we used, and the catalogue

construction process, Sect. 4.3 presents a discussion of selection effects, our measured IRRC properties, while in Sect. 4.4 we discuss the impact of our findings on the radio – SFR calibration.

Throughout this chapter, we use a flat ΛCDM cosmology with $\Omega_M = 0.3$ and $H_0 = 70\,\mathrm{km\,Mpc^{-1}\,s^{-1}}$. Star formation rates and stellar mass values reported assume a Chabrier (2003) initial mass function (IMF).

4.2 Data

As Sargent et al. (2010) found, purely radio- or IR-selected samples introduce a systematic bias to measured IRRC metrics. To account for this selection effect, we created a jointly-selected sample from the union of IR- and a radio-selected samples. This section provides details on this process.

We based our catalogue on the Sloan Digital Sky Survey (SDSS) Data Release 12 (Alam et al., 2015), which provides accurate positions and redshifts to which we anchored our radio and infrared measurements. We used unWISE ((Lang et al., 2014) 22 μm, IRAS 60 and 100 μm, and Herschel Space Observatory (Pilbratt et al. 2010 hereafter, Herschel) 70, 100, 160, 250, 350 and 500 μm fluxes for our IR catalogue, and FIRST and NVSS detections for the radio catalogue. Since they have a variety of depths and survey areas, as presented in Table 4.1, this results in a multi-tiered dataset, which can potentially introduce selection biases (Sargent et al., 2010). Fig. 4.2 shows a comparison of the different radio and total IR luminosity[1] limits of these surveys. This section provides a detailed overview of the data, and the methods used to derive radio and IR luminosities in order to measure the IRRC.

4.2.1 Catalogue construction

We selected SDSS galaxies with spectroscopic (58%), or if no such measurement was available, photometric (42%) redshifts below 0.2 to identify low-redshift objects. Fig. 4.3 shows the redshift distributions of our total catalogue and its different subsets. We note that applying a more stringent z = 0.1 redshift cut does not change qualitatively our results.

Infrared-selected sample

We carried out spectral energy distribution (SED) modelling of infrared data in order to estimate the total IR luminosity of our sources. Since we optimized two parameters during our fitting procedure (SED normalisation and shape parameter; for details see Sect. 4.2.2), we required at least two significant (signal-to-noise ratio $S/N > 5$) IR photometric measurements for a source to enter our IR-selected sample. More specifically, due to the depth and coverage

[1]Survey sensitivities in flux units have been converted to IR luminosities L_{TIR} by finding the best fit Chary and Elbaz (2001) SED template to the 5 σ flux limit (details in Table 4.1) of a given survey in the $0 < z < 0.2$ redshift range.

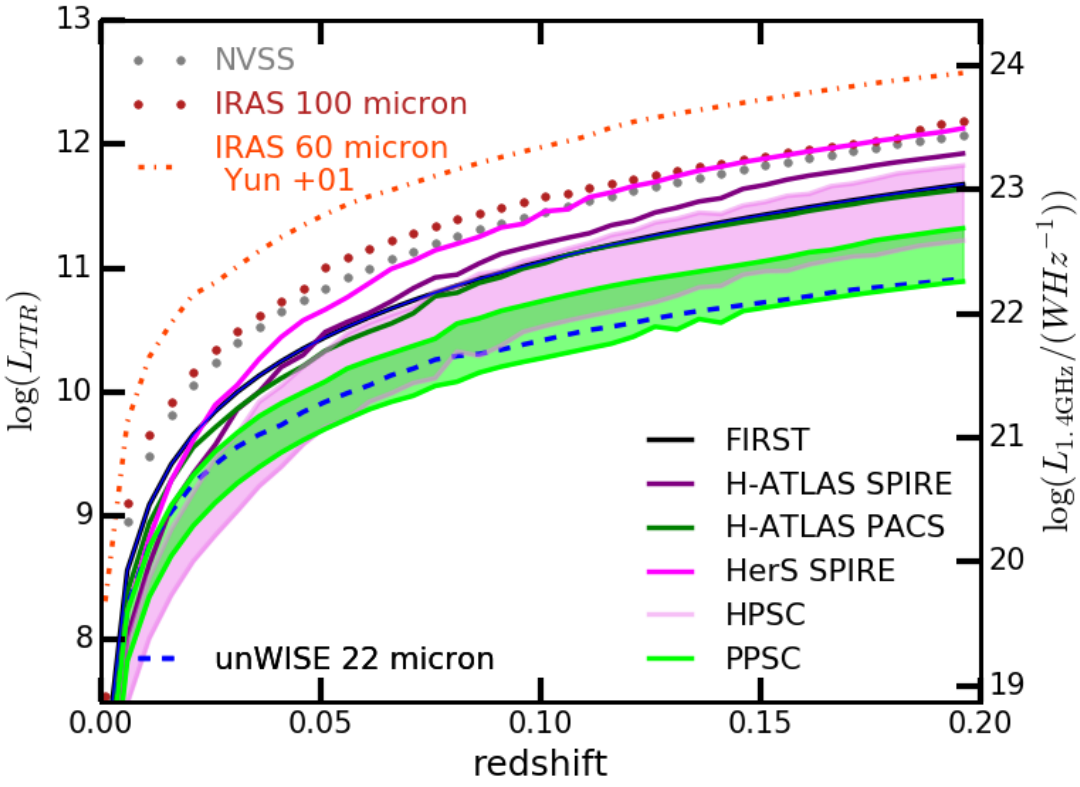

Figure 4.2: Total infrared luminosity limits derived for the surveys used in this work. Radio luminosity limits were rescaled to $L_{\rm TIR}$ with the canonical $q_{\rm TIR}$ = 2.64 of Bell (2003). Infrared limits were derived using best fit templates from the SED library of Chary and Elbaz (2001). H-ATLAS SPIRE and PACS and HerS SPIRE curves are averaged across their bands. The coloured HPSC region is derived from the 16th and 84th percentiles of the overall error distribution in order to represent the different depths of the Herschel fields present in the HPSC catalogue.

Table 4.1: Survey sensitivities and areas used to construct our catalogue.

	$5\,\sigma$ [mJy]	area
FIRST	1.0	10,575 deg^2
NVSS	2.5	37,216 deg^2
IRAS 60 μm	0.2	full sky
IRAS 100 μm	1	full sky
H-ATLAS PACS	232.5	161 deg^2
H-ATLAS SPIRE	45.0	161 deg^2
HerS SPIRE	67.8	79 deg^2
PPPSC	43.0	–
HPSC	24.5	–
WISE 22μm		full sky

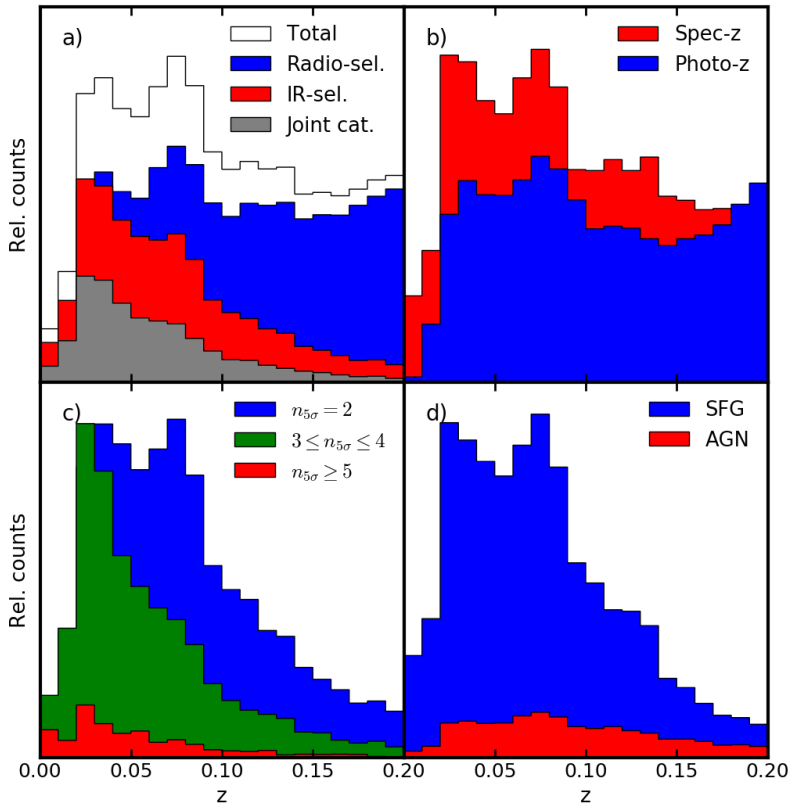

Figure 4.3: Reshift distributions of **a)** the radio-, IR-selected and joint catalogues, **b)** sources with photometric and spectroscopic redshifts, **c)** IR-selected sources with 2, 3 – 4 and more than 5 high signal-to-noise IR detections, and **d)** AGN and star-forming galaxies.

of the 22 μm data used, the selection criteria were (i) a high $S/N > 5$ flux measurement at 22 μm, and (ii) at least one high-S/N far-infrared (FIR) detection in any other of the FIR bands. We note that an advantage of anchoring our IR-catalogue to one band is that it gives us a simplified way to control selection effects in the IR data (for more details see Sect. 4.3.3). In the following we give a brief description of the archival catalogues that form the basis of our IR-selected sample.

WISE data: The Wide-field Infrared Survey (WISE) satellite carried out all-sky observations at 3.4, 4.6, 12 and 22 μm (Wright et al., 2010) with resolutions of 6.1, 6.4, 6.5 and 12.0 arcsec, respectively. Exploiting high-resolution optical data available, Lang et al. (2014) performed flux extraction with a forced photometry approach on un-blurred co-added WISE images at over 400 million SDSS source positions. Since the bulk of the total IR luminosity is emitted at FIR wavelengths, and the mid-IR regime is susceptible to AGN contamination, we only considered 22 μm fluxes. UnWISE photometry was obtained for our parent SDSS sample and we select galaxies with signal-to-noise (S/N) > 5 unWISE flux 22 μm measurements to be included in our analysis; 307,443 low-z galaxies meet this requirement.

IRAS data: The Infrared Astronomical Satellite (IRAS; Neugebauer et al., 1984) mission covered the full sky at a wavelength of 12, 25, 60 and 100 μm. We draw FIR fluxes from the Revised IRAS Faint Source Redshift Catalog (RIFSCz) of Wang et al. (2014a) which contains 60,303 galaxies selected at 60 μm covering 60% of the sky and redshifts out to $z \sim 1$. Wang et al. (2014a) matched the IRAS Faint Source Catalog (FSC) to the WISE 3.46 μm All-Sky Catalog using the likelihood ratio technique. This catalogue was then matched with SDSS DR 10 by taking the closest matching SDSS counterpart, resulting in a sample of 20,277 unique galaxies. We use RIFSCz SDSS DR10 coordinates to match the FSC flux measurements to our parent sample ($z < 0.2$). 17,829 sources in our parent sample have 60 μm fluxes with S/N>5. At 100 μm, 7,261 sources have 100 μm fluxes with S/N>5. Requiring these IRAS sources to also have good (S/N> 5) W4 unWISE detections reduces the number of IRAS 60μm sources to 15,506.

Herschel data: We draw Herschel data from two of the largest wide-area programs; the Herschel-ATLAS survey (Eales et al., 2010; Valiante et al., 2016, HATLAS) and the Herschel Stripe 82 survey (Viero et al., 2014, HerS), which we will describe below. Herschel has two cameras PACS (Photoconductor Array Camera and Spectrometer; Poglitsch et al. 2010) and SPIRE (Spectral and Photometric Imaging REceiver; Griffin et al. 2010), operating at 60-210μm and 200-670μm, respectively.

Herschel-ATLAS (H-ATLAS) Data Release 1 (Valiante et al., 2016), covers the three equatorial fields surveyed by the GAMA (Galaxy and Mass Assembly; Driver et al., 2011) spectroscopic survey. The three fields have a combined area of 161 square degrees and are located around 09h, 12h, and 14h in RA. The catalogue, described in Valiante et al. (2016),

consists of 120,230 sources in 5 photometric bands – 100, 160, 250, 350, 500 μm. It includes SPIRE sources which have a 4 σ (with confusion noise) detection in any of the 250, 350 or 500 μm maps and also provides a robust optical identification from the SDSS DR7/8 catalogue and spectroscopic redshifts from GAMA and SDSS (Bourne et al., 2016).

Our match of the H-ATLAS sources with our SDSS DR12 photometric parent catalogue, using a search radius of 5 arcseconds, resulted in 8,752 sources, mainly due to our redshift limit of z = 0.2. There are 7,001 sources that have 250μm S/N> 5, but only 1,920 of them have also good (S/N>5) unWISE 22μm fluxes.

The Herschel Stripe 82 Catalog (HerS; Viero et al., 2014, [2]) is made with DESPHOT (Roseboom et al., 2012; Wang et al., 2014b) and includes 27,885 band-merged sources with significance greater than 5 σ. Using a 5-arcsecond matching radius for HeRS gives 4,145 local galaxies, 2,512 with S/N>5 in at least one band and 1,118 that are also detected at S/N>5 in unWISE.

Recently the SPIRE Point Source Catalogue (SPSC) [3] and Herschel/PACS Point Source Catalogue (PPSC) have been released. Each Herschel band had sources extracted independently of the other.

From the SPSC catalogues, we use the TIMELINEFITTER (TML) fluxes as they are the most accurate for point sources. Source matching was performed initially with a large search radius before selecting the final search radius for the catalog selection; the radius at which random associations become the main contribution to the matches. From the SPSC catalogues, a search radius of 5 arcsec was used to match 48,115 sources at 250 μm (48,041 with S/N>5). Matching the SPSC 350 μm catalogue with 7 arcsec radius gives 19,578 sources (19,524 with S/N>5). We use a 9 arcsec matching radius for 500 μm catalogue and recover 4,957 sources (4,894 with S/N>5). Combined, there are 50,133 galaxies that have a > 5 σ detection in at least one of the SPSC bands. Requiring a good W4 flux brings the number of SPSC sources down to 18,038.

Similarly, we also draw data from the recent PPSC (PACS Point Source Catalogue). Fluxes have been measured using the ANNULARSKYAPERTUREPHOTOMETRY task and apertures out to a radius of 18 arcsec for the 70 and 100 μm bands and 22 arcsec for the 160 μm band. Fluxes were aperture corrected based on Lutz (2015). We have removed flagged (edge-flag, blend-flag, warm altitude or solar system map flag) sources keeping 78%, 64% and 69% of sources at 70, 100, and 160 μm, respectively. For the 60 μm and 100 μm catalogues, we determined 4 arcsec to be a good matching radius, finding 1,134 and 6,970 sources the respective bands. At 160 μm, we used a matching radius of 5 arcsec and found 6,413 matches. There are 6,302 sources with S/N>5 in at least one of 70 or 100 or 160 μm bands and 3,421 additionally have good W4 unWISE fluxes.

Many sources in H-ATLAS and HeRS are also in the SPSC and PPSC catalogue. When

[2]http://www.astro.caltech.edu/hers/HerS_Home.html

[3]https://www.cosmos.esa.int/web/herschel/spire-point-source-catalogue

sources are present in both catalogues, we prefer to use the H-ATLAS or HeRS fluxes over the SPSC or PPSC values.

Our final IR-selected sample contains a total of 32,644 galaxies with an S/N>5 detection in unWISE W4 and at least one FIR wavelengths.

Radio-selected sample

Radio measurements were taken from the Unified Radio Catalog (Kimball and Ivezić, 2008, 2014). It is primarily based on Faint Images of the Radio Sky at Twenty centimeters (FIRST; Becker et al., 1995) and NRAO VLA Sky Survey (NVSS; Condon et al., 1998) radio data, paired up with other lower frequency radio measurements and SDSS. Both the FIRST and NVSS surveys were conducted with VLA. FIRST focused on the SDSS footprint as established in Helfand et al. (2015), with higher resolution and sensitivity than NVSS, while NVSS surveyed the entire Northern sky. Due to its lower angular resolution, NVSS is less prone to resolving out radio flux components.

From the Unified Radio Catalog we extracted the FIRST primary sources and NVSS detections with no FIRST counterparts[4]. The latter selection adds extended objects that were not found by FIRST due to its high resolution, as well as radio sources outside of FIRST's footprint, but potentially with more recent SDSS coverage. We then cross-matched this sample with our local SDSS-based optical sample. This final radio-selected sample consists of 55,494 objects. After a comparison of FIRST and NVSS fluxes for sources where both are available in our sample, we decided to use FIRST fluxes when possible, and take NVSS where it is the only 1.4 GHz measurement. Our final radio-selected sample consists of 55,398 sources.

Joint catalogue

Combining the infrared- and radio-selected catalogues resulted in a jointly-selected catalogue of 77,039 objects. In this, 11,099 have detections at both radio and IR waveleghts, 21,545 have only IR and 44,395 only radio data.

Fig. 4.2 shows total IR and radio luminosity limits as a function of redshift estimated for the various photometric bands in the joint catalogue. For the infrared surveys, we plot the $L_{\rm TIR}$ value of the Chary and Elbaz (2001) SED template that reproduces the respective catalogue's $5\,\sigma$ flux limit at a given redshift between z = 0 to 0.2. Radio fluxes were converted into 1.4 GHz luminosities using Eq. 4.1, then subsequently rescaled to $L_{\rm TIR}$ with the local $q_{\rm TIR}$ = 2.64 of Bell (2003), in order to facilitate a direct comparison between all available data. The unWISE4 fluxes represent the deepest tier with PPSC photometry. The other Herschel data (H-ATLAS, HerS and HPSC) are well-matched with FIRST, forming the middle tier of our catalogue. Lastly, NVSS and IRAS provide a shallow but wide layer. The 2 Jy IRAS 60 μm flux cut of Yun et al. (2001) is mismatched with NVSS. To avoid selection effects biasing our

[4]We used the selection flag of *((matchflag_first = -1) or ((matchflag_nvss = -1) and (matchflag_first = 0)))*.

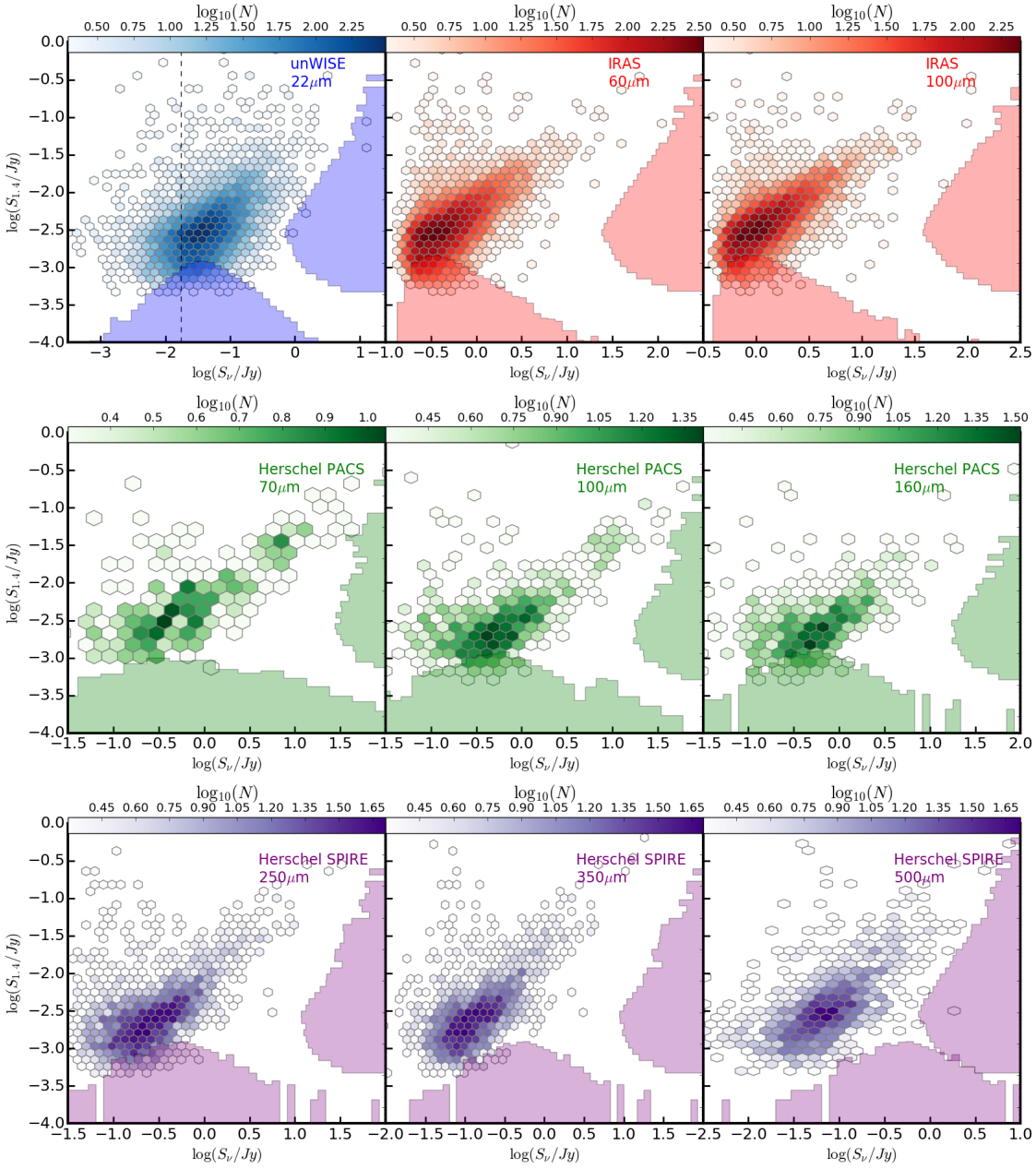

Figure 4.4: Radio (FIRST or NVSS) versus infrared fluxes from unWISE (22 μm), IRAS (60 and 100 μm) and Herschel (100, 160, 250, 350 and 500 μm). IR and radio flux distributions are shown on the sides. Dashed line in the top left panel illustrates the 1.7 mJy flux cut we applied in order to select our radio-IR sensitivity matched sample, as descried in Sect. 4.3.3.

IRRC measurement, as discussed in Sargent et al. (2010), we applied a flux cut of 1.7 mJy to unWISE 4 data. To further homogenize our selection, we require our sources to have FIRST survey coverage. This resulted in a final, sensitivity matched joint sample of 9,236 galaxies. The effects of asymmetric luminosity limits are further investigated in Sect. 4.3.3.

Fig. 4.4. shows the infrared fluxes in various bands against the 1.4 GHz radio fluxes of all the sources with both radio and respective IR measurements. The correlation is apparent before the conversion to luminosity.

4.2.2 Measuring 1.4 GHz radio and the total infrared luminosity

Radio luminosity

Radio luminosities were derived using the standard equation

$$\left(\frac{L_{1.4}}{\mathrm{W\,Hz^{-1}}}\right) = C\,\frac{4\pi}{(1+z)^{(1+\alpha)}}\left(\frac{D_L}{\mathrm{Mpc}}\right)^2\left(\frac{S_{1.4}}{\mathrm{mJy}}\right), \tag{4.1}$$

where $L_{1.4}$ is the 1.4 GHz rest-frame radio continuum luminosity, $C = 9.52 \times 10^{15}$ is the conversion factor from $\mathrm{Mpc^2\,mJy}$ to $\mathrm{W\,Hz^{-1}}$, α is the radio spectral index[5], z is redshift, D_L is the luminosity distance and $S_{1.4}$ is the measured 1.4 GHz flux. Since our catalogue only has 1.4 GHz fluxes, and thus the radio spectral slopes are not measured, we used the typical $\alpha = -0.7$ assumption (e.g. Kimball and Ivezić, 2008).

Total infrared luminosity

In order to estimate the total infrared luminosity of our IR-selected sources, we fitted their fluxes with the SED templates of Chary and Elbaz (2001). This luminosity-dependent SED library contains 105 IR spectra of different shapes, each with a different total infrared luminosity. With a cubic spline interpolation between the normalised spectra, we obtained a continuous shape parameter, γ, we can freely tune. To relax the assumption of Chary and Elbaz (2001) that the SED shape is intrinsically tied to the IR luminosity of the sources, we fitted the SED shape parameter and luminosity independently of each other.

To find the best fit SED model with realistic error estimates on the free parameters, we used an affine invariant Markov chain Monte Carlo (MCMC) sampler called EMCEE. It is a free, open-source code implemented in PYTHON. We used 100 walkers, and found that the typical MCMC chain's burn-in period is $\sim$ 200 steps, so to achieve sufficient sampling, we ran each chain for 2000 more steps and produced marginalised distributions and statistics from these. A median acceptance fraction of 0.4 with a 0.1 standard deviation indicates that the majority of our fits are sufficiently converged. Fig. 4.5 shows typical SEDs with best-fit model and additional randomly drawn models from the MCMC chains representing the 1 σ confidence interval of our fit alongside the marginalised L_{TIR} distribution from the posterior sampling, which was used to derive L_{TIR} uncertainties. We note that monochromatic

[5]The radio spectral index is defined as $S_\nu \propto \nu^\alpha$, where S_ν is the flux density at frequency ν.

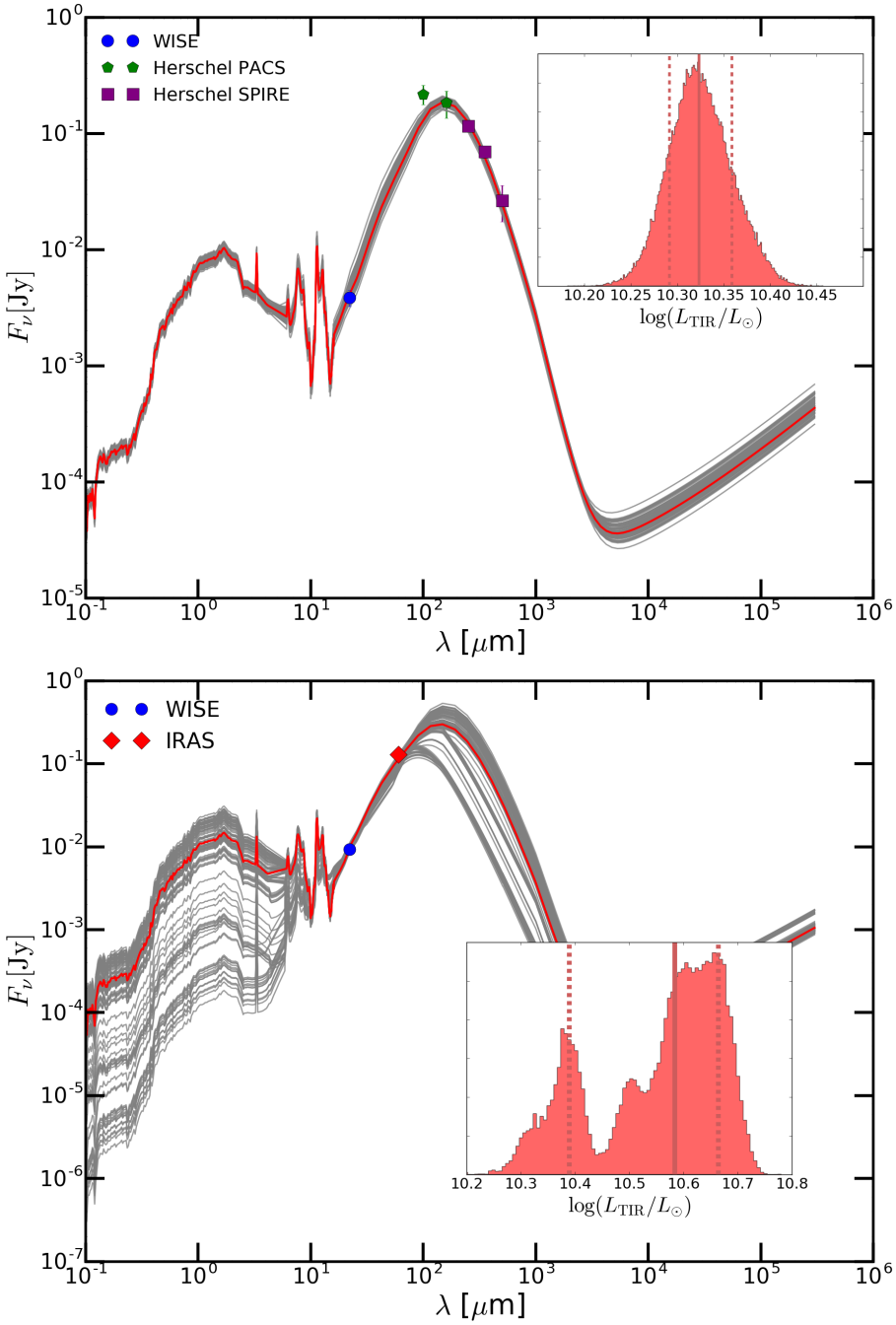

Figure 4.5: Examples of fitted spectral energy distributions with varying photometric coverages, using the templates of Chary and Elbaz (2001). Red lines are the best-fit curves, grey ones are 100 other randomly selected models from MCMC chains, representing the $1\,\sigma$ confidence intervals of each fit. The insets show the marginalized $L_{\rm TIR}$ parameter distributions. Since the Chary and Elbaz (2001) library is not completely smooth due to some discontinuities , sharp cut-offs occur in the distribution of the shape parameter, γ, at certain values, as this example demonstrates.

luminosities in some wavelength regimes do not change smoothly as a function of γ, i.e. there are some abrupt changes in SED shape between certain γ values. This occasionally leads to multi-modal marginalized $L_{\rm TIR}$ distributions (see bottom panel of Fig. 4.5), because there are different best-fit normalizations for template shapes, that are significantly different than the neighbouring templates in the library. This is a notably bigger issue with less photometric points, when the intrinsic SED shape is less well constrained by our data. Thus, typical $L_{\rm TIR}$ errors in our flux-matched catalogue are 0.12, 0.05 and 0.02 dex for sources with 2, 3 – 4, and >4 measured photometric bands, respectively.

The fitted SEDs were used to derive an empirical K-correction at various wavelengths by taking the ratio of the observed and rest-frame fluxes for each source. These corrections were applied to measured fluxes to compute the monochromatic IR luminosities presented in Fig. 4.6.

4.2.3 Identifying AGN and star-forming galaxies

It is broadly accepted, that the IRRC emerges from the correlation of IR and radio fluxes with star formation activity. Since our primary aim is to study this relation, we aim to select sources in our sample identified as dominantly star-forming. On the other hand, since the IRRC can also be used to detect excess radio emission presumably linked to AGN activity, we also investigated AGN in our sample. The parent SDSS catalogue contains such classification based on optical emission line ratios of galaxies. We used these BPT-derived classes to create star-forming and AGN subsamples. We note that we excluded "broadline" sources from the star-forming sample in order to create the purest selection of SFGs. The total jointly-selected sample contains 6,270 SFGs, 722 AGN, while the flux-selected subsample contains 4,772 SFGs and 535 AGN.

4.3 Results

4.3.1 Monochromatic infrared-radio correlations

As Fig. 4.6 shows, all observed monochromatic IR luminosities correlate with radio power. Scatter was measured as the σ of the Gaussian function fitted to the data's offset distribution relative to the linear relation. Table 4.2. contains the slopes, $m_{\rm all}$, $m_{\rm fluxlimited}$ and $m_{\rm SFG}$ and scatters ($\sigma_{\rm all}$, $\sigma_{\rm fluxlimited}$ and $\sigma_{\rm SFG}$) of each individual single-band correlations for our entire joint catalogue, the flux limited sample (see Sect. 4.3.3) and its SFG subset, respectively. Both the flux limited sample and the SFGs produce similar near-linear relations with $\sim$ 0.2–0.25 dex scatters, while the jointly-selected sources with unmatched survey sensitivities lead to systematically shallower $\rm L_{1.4GHz} - \nu L_{\nu}$ fits and larger scatter. As expected, the sensitivity matched star forming galaxy subsets are closest to a linear relation with systematically smaller scatters than the other two samples. IRAS 100 μm luminosities yield the tightest correlation,

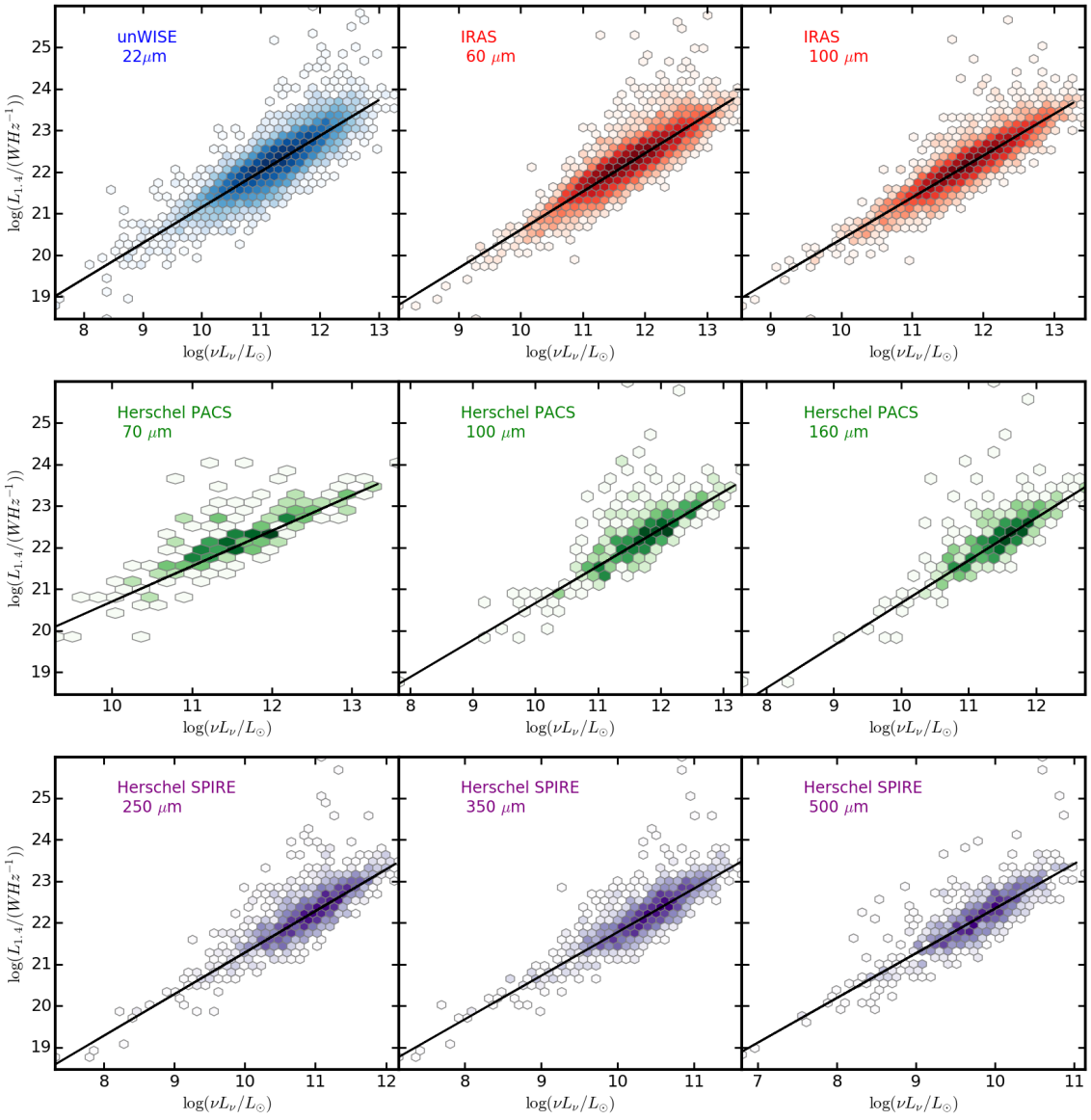

Figure 4.6: Radio luminosity at 1.4 GHz as a function of various monochromatic IR luminosities. Data are from the sensitivity matched sample (coloured hexagonal bins), while the linear relations shown (black lines) are fitted only to the SFGs in each panel. Table 4.2 presents the slope and scatter of these for all sources, the flux limited sample and its SFG subset.

and are the most robust against selection effects, i.e. the measured correlations are consistent between all three studied samples. It is likely due to the combination of highest source counts among all the samples, and the fact that typically the peak of the IR SED in our redshift regime falls closest to 100 μm in all the bands used. We note that rest-frame luminosities were derived from SED fits using at least two photometric bands, thus monochromatic IR–radio correlations measured with single band data are likely less accurate.

Fig. 4.7 presents the correlation between $L_{\rm TIR}$ and $L_{1.4\rm GHz}$. The slope and scatter measurements of the IRRC using the joint catalogue, flux-selected and flux-selected SFG samples are also presented in Table 4.2. With exception of 100 μm IRAS fluxes, this correlation proves to be the tightest compared to single band relations.

4.3.2 Measuring the infrared-radio correlation

The IRRC is quantified by the logarithmic ratio, $q_{\rm TIR}$, of the total infrared (8 - 1000 μm; $L_{\rm TIR}$) and 1.4 GHz radio ($L_{1.4}$) luminosities:

$$q_{\rm TIR} \equiv \log\left(\frac{L_{TIR}}{3.75{\times}10^{12}\,\rm W}\right) - \log\left(\frac{L_{1.4}}{\rm W\,Hz^{-1}}\right). \tag{4.2}$$

For a more direct comparison with Yun et al. (2001), we also calculated $q_{\rm FIR}$, which is computed using the FIR luminosity (42 - 122 μm; $L_{\rm FIR}$).

4.3.3 The effect of flux limits on IRRC statistics

Sargent et al. (2010) found that a mismatch in the sensitivities of IR and radio data can bias the median $q_{\rm TIR}$ value ($\overline{q}_{\rm TIR}$) of a sample. In order to demonstrate the impact of such a difference in the flux limits, we computed the $\overline{q}_{\rm TIR}$ values of various flux-limited subsamples in our jointly-selected catalogue. We quantified the mismatch between different IR and radio flux cuts as the mean difference of the L_{TIR} curves calculated for any given flux limit (see e.g. Fig. 4.2). Fig. 4.8 shows the difference between the $\overline{q}_{\rm TIR}$ of each flux selection and $q_{\rm TIR}$ = 2.64 of Bell (2003) as a function of the relative depth of the IR and 1.4 GHz radio data.

In line with the analysis of Sargent et al. (2010), we find that IR-limited (i.e. when radio data are more sensitive than IR) $\overline{q}_{\rm TIR}$ measurements are positively biased, whereas radio-limited samples lead to lower $\overline{q}_{\rm TIR}$ values. The magnitude of this bias is proportional to the mismatch between the radio and IR data. We note that this bias can be negated with either a selection based on a third, uncorrelated selection criterion, e.g. by studying a mass-matched sample, or techniques that allow probing IR and radio fluxes below their nominal limits, such as stacking or survival analysis.

Fig. 4.8 predicts that due to its asymmetric selection criteria, the median $q_{\rm FIR}$ of Yun et al. (2001) is positively biased. In order to find evidence for this in our catalogue, we compared the $\overline{q}_{\rm FIR}$ values for both the $S_{60} > 2$ Jy selection of Yun et al. (2001) ($\overline{q}_{\rm FIR,\,Yun}$ = 2.42) and our sensitivity matched ($\overline{q}_{\rm FIR,\,flux\,lim}$ = 2.31) samples. The difference between average sensitivities

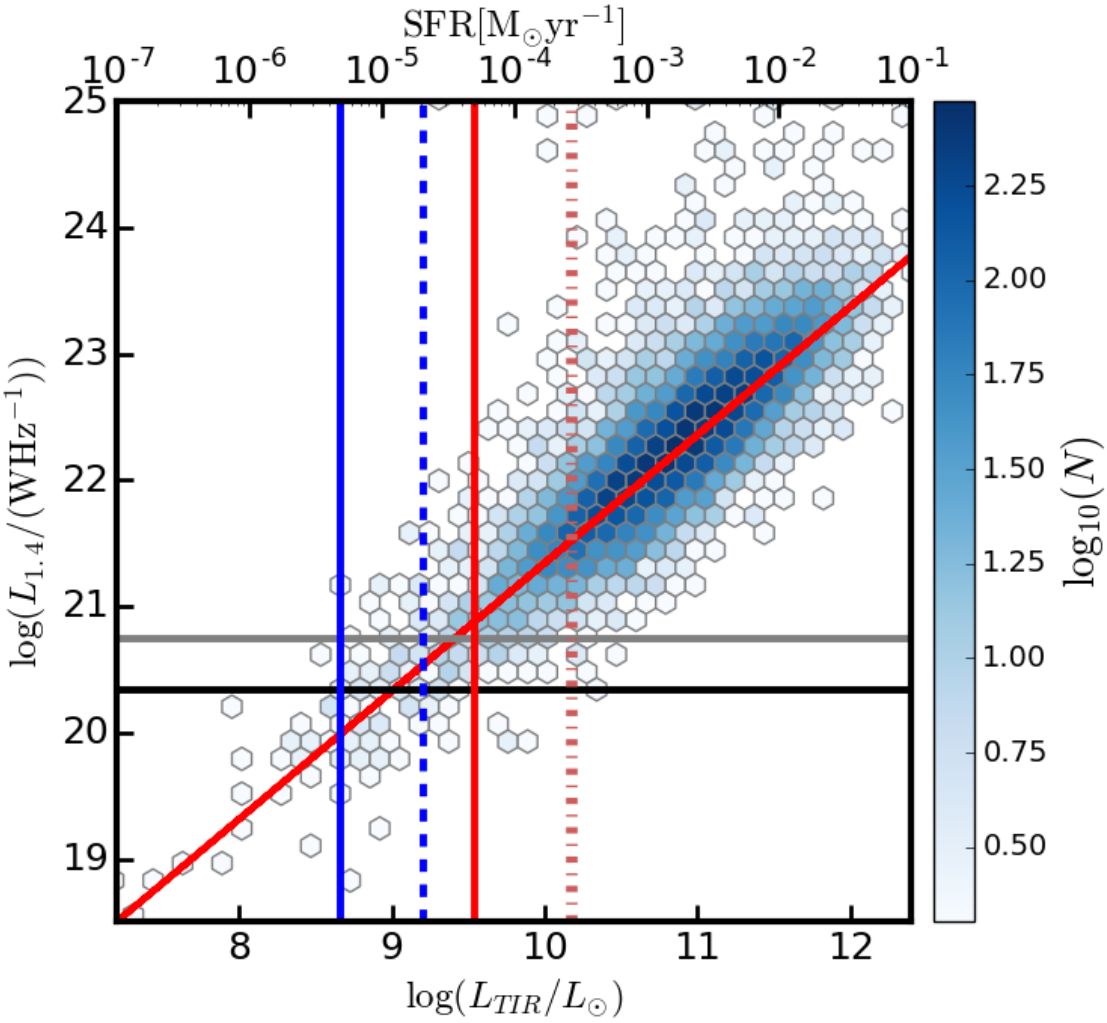

Figure 4.7: Radio luminosity at 1.4 GHz as a function of the total infrared luminosity. Data are from the sensitivity matched sample (coloured hexagonal bins), while the linear relations shown (red line) is fitted only to the SFGs in the sample. Table 4.2 presents the slope and scatter of the relation for both the flux limited, unbiased sample and its SFG subset. Star formation rate axes were calculated using the canonical $q_{\rm TIR}$ = 2.64 of Bell (2003).

Table 4.2: Slope measurements ($m_{\rm all}$, $m_{\rm fluxlim}$ and $m_{\rm SFG}$) and scatters ($\sigma_{\rm all}$, $\sigma_{\rm fluxlim}$ and $\sigma_{\rm SFG}$) of each monochromatic IR – 1.4 GHz radio luminosity correlation, and the IRRC for the joint catalogue, the flux selected, unbiased sample and SFGs.

	$L_{22\mu m}$	$L_{60\mu m}$	$L_{100\mu m,\rm IRAS}$	$L_{70\mu m}$	$L_{100\mu m,\rm Herschel}$	$L_{160\mu m}$	$L_{250\mu m}$	$L_{350\mu m}$	$L_{500\mu m}$	$L_{\rm TIR}$
$m_{\rm all}$	0.79	0.91	0.99	0.74	0.79	0.93	0.96	1.04	1.04	0.99
$\sigma_{\rm all}$	0.27	0.21	0.18	0.26	0.30	0.26	0.26	0.26	0.28	0.23
$m_{\rm fluxlim}$	0.85	0.91	1.00	0.80	0.87	0.96	0.99	1.06	1.09	1.01
$\sigma_{\rm fluxlim}$	0.25	0.21	0.18	0.26	0.25	0.24	0.25	0.25	0.27	0.20
$m_{\rm SFG}$	0.86	0.92	1.00	0.85	0.89	1.02	1.00	1.05	1.08	1.02
$\sigma_{\rm SFG}$	0.25	0.20	0.18	0.20	0.22	0.22	0.23	0.24	0.27	0.21

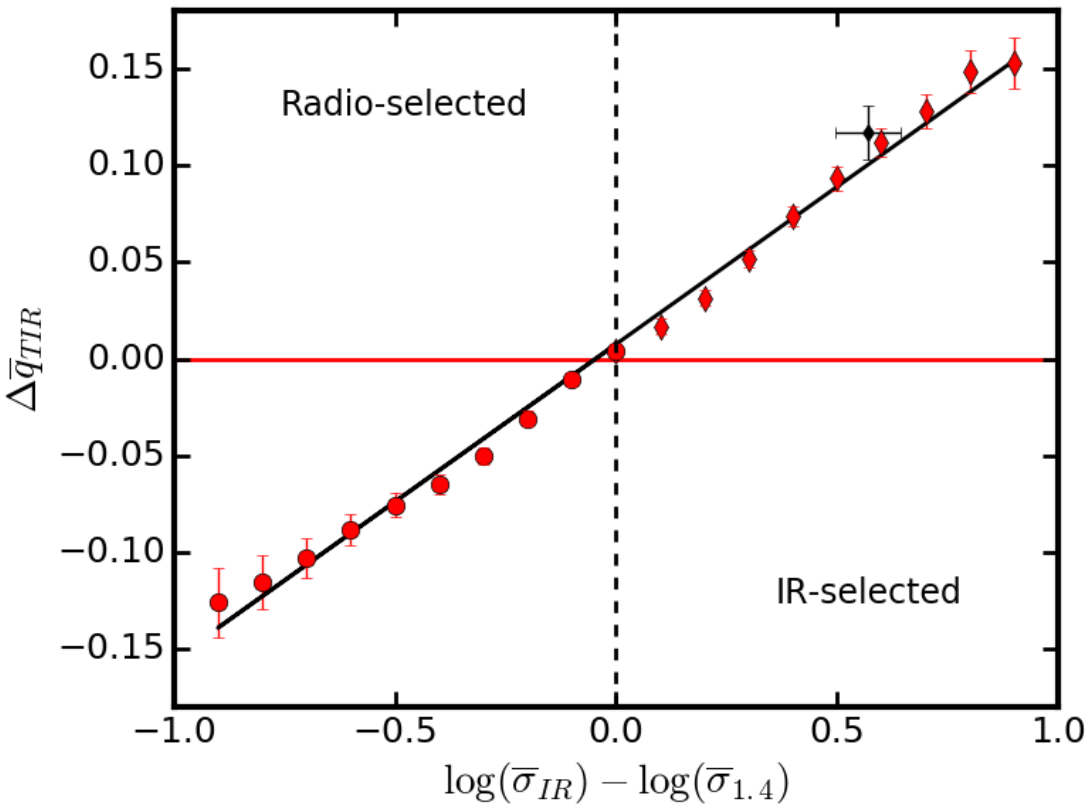

Figure 4.8: Median $q_{\rm TIR}$ difference to the local $q_{\rm TIR} = 2.64$ of Bell (2003) as a function of offset between the sensitivity of IR and radio data. The black point represents the measured difference between the $\overline{q}_{\rm FIR}$ value for IRAS 60 μm > 2 Jy sources (i.e. the selection used in Yun et al., 2001) and $\overline{q}_{\rm FIR}$ for our unbiased, sensitivity-matched sample. It is consistent with the bias predicted from our analysis.

in the Yun et al. (2001) catalogue was computed from the 2 Jy IRAS 60 μm and NVSS curves in Fig. 4.2, its uncertainty was taken as the standard deviation of the differences in the plotted redshift range. The observed $\overline{q}_{\rm FIR}$ difference falls on our prediction, suggesting that the measured $\overline{q}_{\rm FIR} = 2.42\pm0.01$ using the selection criteria of Yun et al. (2001) is slightly biased by ~ 0.1 dex, and thus local $\overline{q}_{\rm FIR}$ value is 2.307 ± 0.002.

4.3.4 Infrared-radio ratio of star-forming galaxies

In our total sample, we measure a $\overline{q}_{\rm TIR} = 2.583 \pm 0.003$[6], broadly consistent with predictions from Fig. 4.8 considering the ~ 0.6 dex sensitivity offset between unWISE 22 μm fluxes, our

[6]The error was taken as the error on the mean. However, we note that this is likely much smaller than most of the systematic uncertainties. Therefore a further exploration of other sources of error, such as error propagation from individual luminosity measurements, uncertainty stemming from a model template library choice, error when determining the flux cut to match survey sensitivities, etc., is needed.

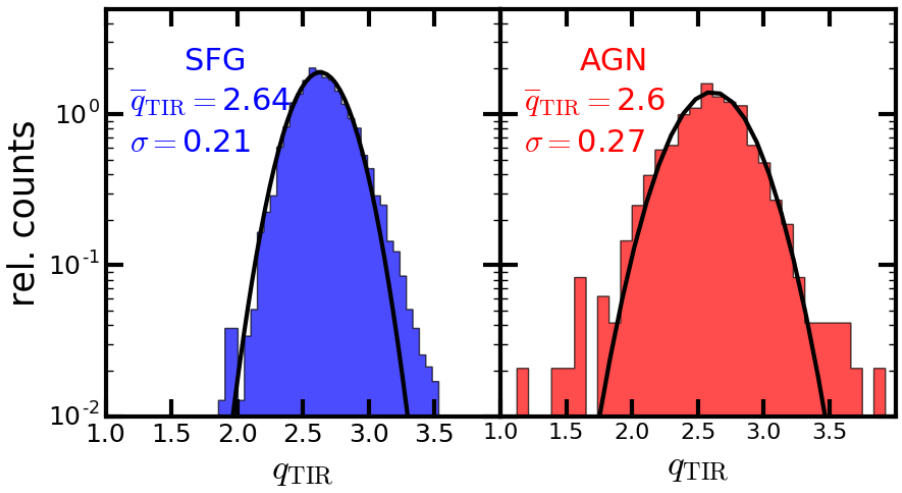

Figure 4.9: Distribution of $q_{\rm TIR}$ values for SFGs (**left**) and AGN (**right**) in the luminosity matched, unbiased samples. AGN show lower $q_{\rm TIR}$ on average, and larger scatter.

deepest and widest IR photometry and the FIRST flux limit, as seen in Fig. 4.2. Scatter is measured to be 0.23 dex. In our sensitivity matched sample we find $\overline{q}_{\rm TIR} = 2.613 \pm 0.003$, more in line with the measured median value of 2.64 ± 0.02 in Bell (2003). If we select only SFGs in the sensitivity matched sample, and thus remove most radio loud objects, we find $\overline{q}_{\rm TIR} = 2.637 \pm 0.003$ and a scatter of 0.205 dex, ~ 0.5 dex smaller than in Bell (2003) and Yun et al. (2001), likely due to our better IR photometric coverage. The $q_{\rm TIR}$ distribution of SFGs in our sensitivity matched sample is shown in Fig. 4.9.

4.3.5 Infrared-radio ratio of AGN host galaxies

AGN activity in radio loud galaxies is expected to contaminate star-formation related emission at radio frequencies, thus the infrared-radio ratio of AGN on average is usually found to be lower than for pure SFG samples (e.g. Morić et al., 2010). Indeed, the AGN fraction on the $L_{\rm TIR} - L_{1.4GHz}$ plane, shown in Fig. 4.10, is found to be higher in the radio excess regime, than on the main locus of the IRRC, with some excess AGN content among radio quiet galaxies.

We measure a $\overline{q}_{\rm TIR} = 2.60 \pm 0.02$ for AGNs in our sensitivity matched sample, with a scatter of 0.26 dex. The enhanced scatter compared to SFGs is also seen in Fig. 4.10, and is in qualitative agreement with the findings of e.g. Morić et al. (2010). $q_{\rm TIR}$ distribution of AGN host galaxies in our luminosity matched sample is shown in Fig. 4.9.

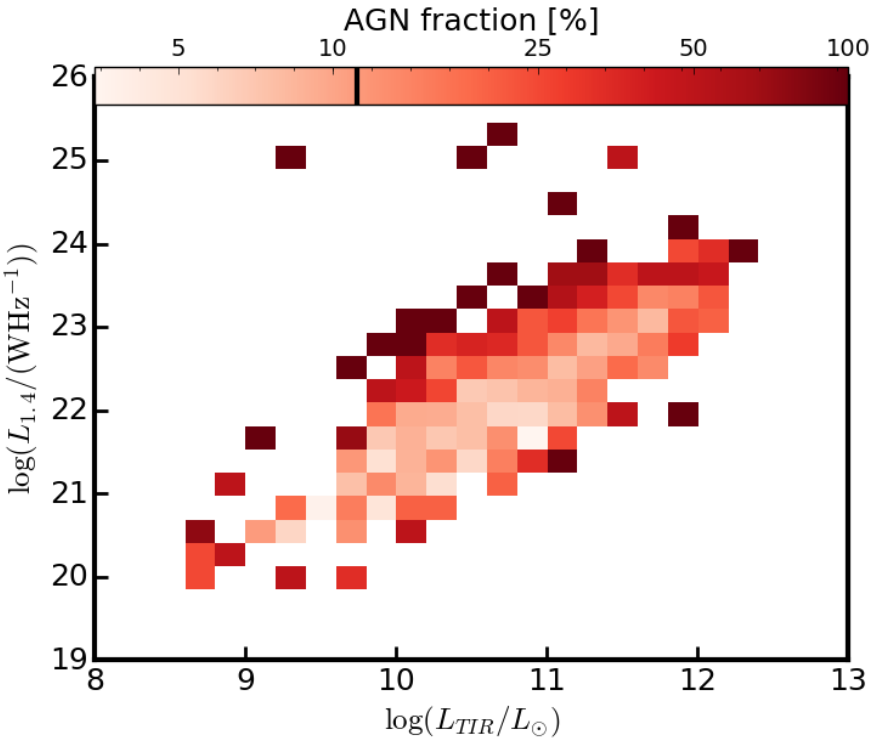

Figure 4.10: Fraction of AGN host galaxies on the L_{TIR}) – $L_{1.4}$ plane. AGN preferentially occur above the main locus of the IRRC, and have higher than average fractions below. Black line in the colour bar indicates the average, 11 %, AGN fraction of the sample.

4.4 Discussion

4.4.1 Quantifying asymmetric flux selection effects

As we demonstrated in Sect. 4.3.3, IR- or radio-selected samples can lead to systematic errors in measured IRRC statistics. Using our fit to the trend in Fig. 4.8 it is now possible to quantitatively estimate this selection bias, which is highly valuable when comparing various works in the literature (similar to the compilation in Table 2 of Sargent et al., 2010). However, we note that the relation derived here is likely not universal, but has some luminosity dependence due to different relative IR and radio number counts. Nevertheless, it is a useful tool that can reconcile inconsistent results, or point out tensions unrelated to this selection effect.

4.4.2 Anchoring high-z IRRC studies

Some recent studies have found declining $\overline{q}_{\rm TIR}(z)$ trends with a power law index of $0.12 - 0.19$. The fact that some of these works predicted higher than 2.64 $\overline{q}_{\rm TIR}$ values at z = 0 (Sargent et al., 2010; Delhaize et al., 2017), while redshift evolution from other data underestimated it (Calistro Rivera et al., 2017), raised concerns regarding the robustness of local the $\overline{q}_{\rm TIR}$. We find a value consistent with the canonical Bell (2003) result in a significantly larger, jointly-selected galaxy sample, suggesting that so far hidden systematics are at play in some high-z measurements. E.g. as a result of the well-known z $\approx$ 0.3 overdensity in the COSMOS field (Scoville et al., 2013), or the loss of some extended radio flux components in nearby galaxies due to insufficient uv-sampling in high-resolution radio surveys, affecting the the analysis of Sargent et al. (2010), Delhaize et al. (2017) and Molnár et al. (2018). Inconsistency with local measurements can also arise from flux-selections, as mentioned before, explaining e.g. lower than expected $\overline{q}_{\rm TIR}$ in radio-selected samples, such as the catalogue used by Calistro Rivera et al. (2017). We emphasize the need for reliable low-z $q_{\rm TIR}$ values in anchoring redshift evolution fits to high-z data.

4.4.3 The infrared-radio correlation's luminosity dependence

We investigated the average IR-radio ratio's luminosity dependence. Fig. 4.11 presents $q_{\rm TIR}$ values for SFGs and AGN host galaxies as a function of their radio and total IR luminosities. We find that $L_{\rm TIR}$ has very minimal impact on $q_{\rm TIR}$ for both SFGs and AGN, with a fitted linear slope of -0.02 and -0.04, respectively. However, radio bright ($L_{1.4\rm GHz} \geq 22.5$ W Hz^{-1}) sources tend to have lower than average $q_{\rm TIR}$ values, and conversely, galaxies that are faint in radio have higher $q_{\rm TIR}$. Best-fit slopes for SFG and AGN are -0.15 and -0.23, respectively. This result is in qualitative agreement with the findings of Morić et al. (2010). We note that despite the fact that AGN hosts and SFGs show similar behaviour in both cases, AGN have marginally, but systematically steeper relations.

In Fig. 4.12 and 4.13 we present the $q_{\rm TIR}$ histograms in each IR and radio luminosity

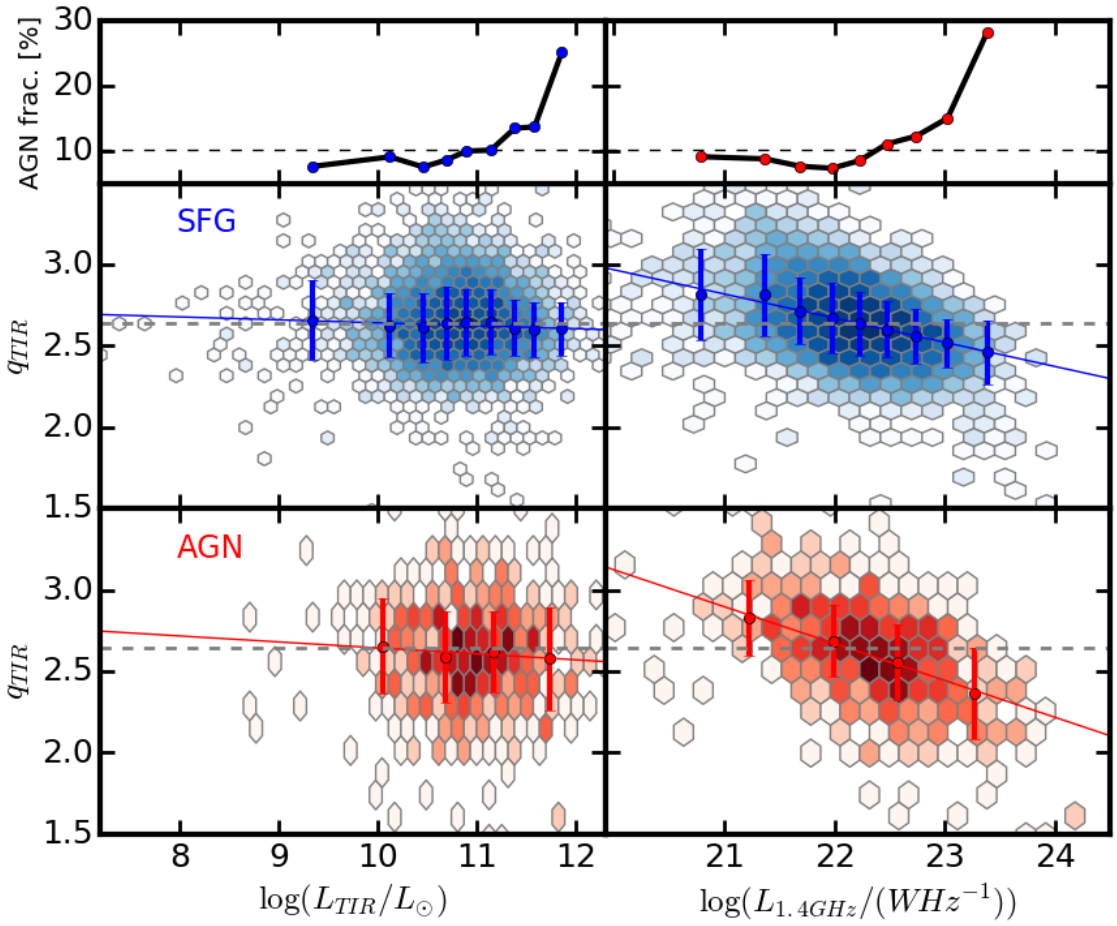

Figure 4.11: Median q_{TIR} of SFGs (middle) and AGN (bottom) as a function of IR (left) and radio (right) luminosity in the sensitivity matched, unbiased samples. Blue and red points are median q_{TIR} values of luminosity bins, errorbars represent the measured scatter of these binned q_{TIR} distributions (for details see Figs. 4.12, 4.13 and 4.14). Dashed horizontal lines in these panels show the median q_{TIR} value found in our SFG sample, as well as in Bell (2003). Top panels show the AGN fractions in each IR and radio bin of the middle figures. Dashed lines represent the $\sim$ 11 % average AGN fraction of the flux-matched sample.

bin shown in the top, SFG panels of Fig. 4.11, respectively. Fig. 4.14 shows the same for AGN hosts (bottom panels of Fig. 4.11). We measure systematically decreasing scatters for SFGs both with increasing $L_{\rm TIR}$ and $L_{\rm 1.4GHz}$. This is seemingly at odds with the findings of e.g. Yun et al. (2001), who measure a higher scatter at high radio and IR luminosities. However, the sharply increasing AGN fraction towards this luminosity range both at IR and radio wavelengths (see Fig. 4.11 and 4.10) suggest that studies that do not separate these populations will add to the measured IRRC scatter especially at the high luminosity regime, due to the slightly lower $_{\rm TIR}$ and higher spread of AGN.

It is also interesting, that the $_{\rm TIR}$ of both star-forming galaxies and AGN follow similar type trends (i.e. flat evolution as a function of $L_{\rm TIR}$, and a decrease with increasing $L_{\rm 1.4GHz}$). This could suggest that the process that gives rise to this behaviour is present in both types of galaxies, hence it is linked to star formation rather than AGN activity. If this is the case, it has an impact on IRRC models, and as a consequence, the radio – SFR calibration at $z \approx 0$.

Since this is still an on-going project, I will summarize its main findings, outline current efforts to finalize the results, and finally discuss future plans in Chapter 6.

Contributions

SL assembled the optical and IR photometry and wrote the relevant parts of Sect. 4.2.1. All co-authors contributed comments and advice.

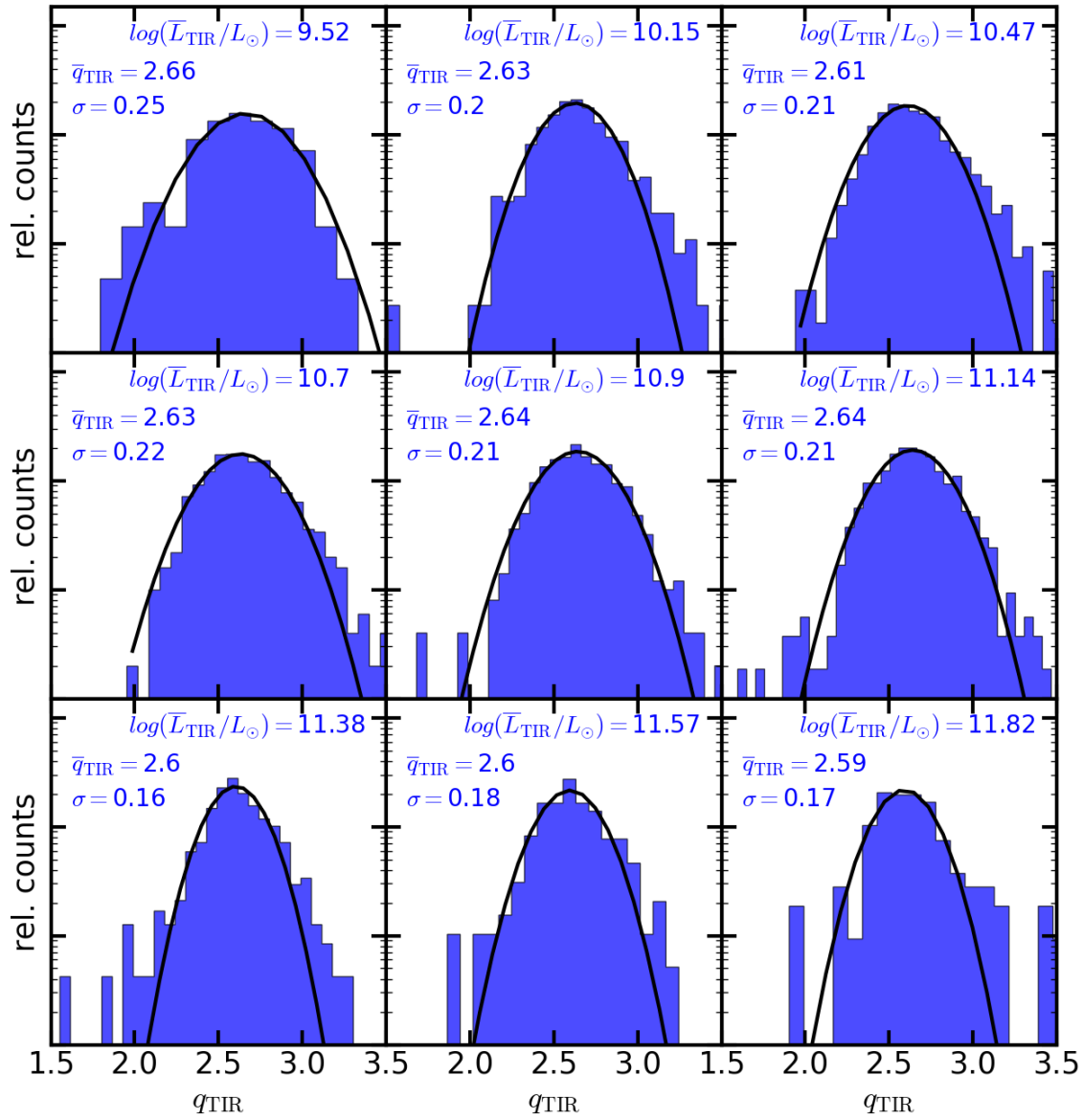

Figure 4.12: Distribution of $q_{\rm TIR}$ values for SFGs of the luminosity matched, unbiased sample in various $L_{\rm TIR}$ bins. Median IR luminosity values ($\overline{L}_{\rm TIR}$), fitted median $q_{\rm TIR}$ ($\overline{q}_{\rm TIR}$) and scatter (σ) are displayed in each panel.

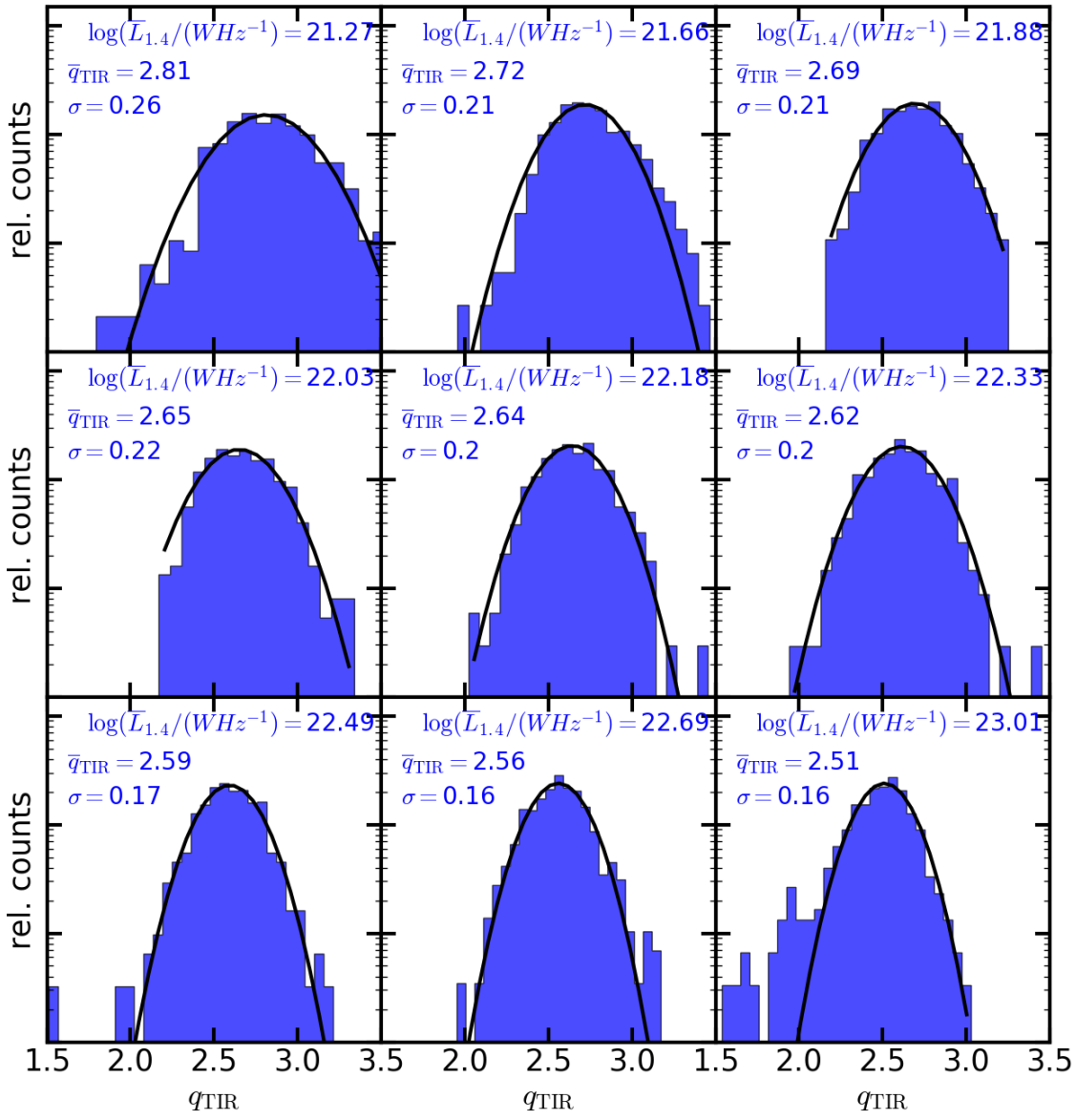

Figure 4.13: Same as Fig. 4.12, but with $L_{1.4\rm GHz}$.

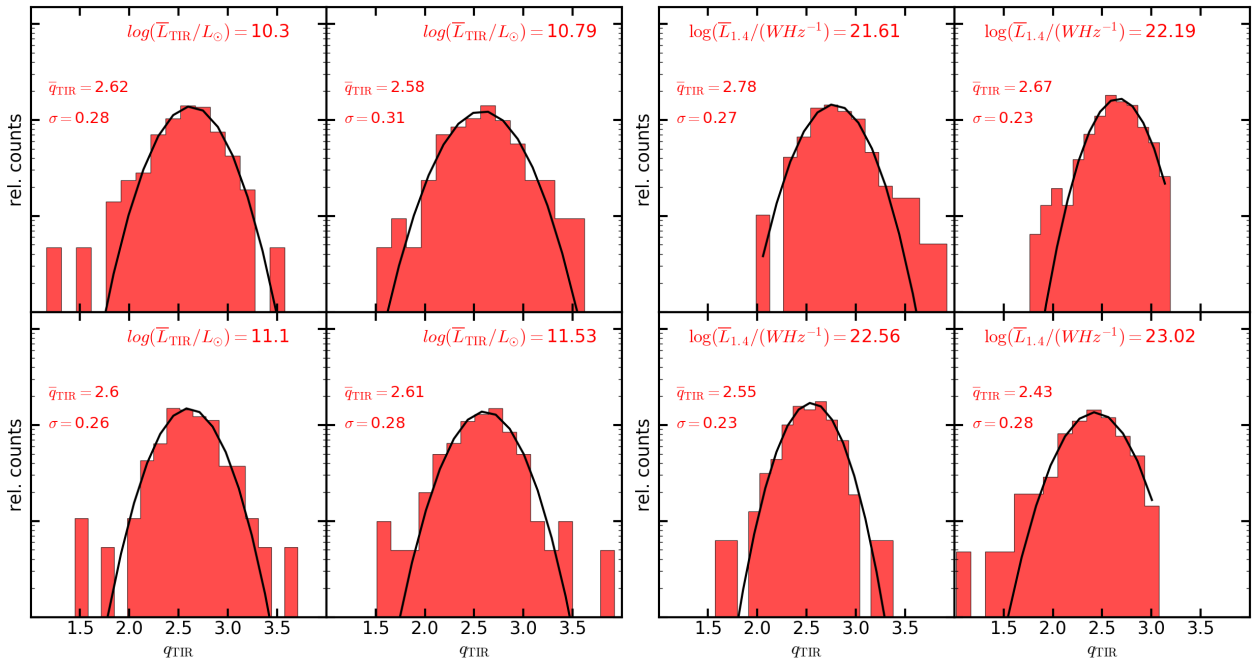

Figure 4.14: Same as Fig. 4.12 and 4.13, but with AGN host galaxies.

Chapter 5

Double core of G163.82–8.44

This paper is being prepared for publication in Zahorecz et al., 2018, Monthly Notices of Royal Astronomical Society. This chapter is based on sections of the paper to which I most significantly contributed.

Co-authors:

D. Cs. Molnár, M. Juvela, K. Dobashi, O. Fehér, J. Harju, A. Kraus, T. Onishi, S. Pintér, L. V. Tóth

Chapters 2, 3 and 4 examined star formation in various low- and high-redshift extragalactic environments with and without the presence of an AGN on large, ~ kpc size galactic scales. However, our understanding of star formation in small, ~ pc scales and individual cases is still limited. This Chapter investigates the physical properties of the dense ISM in a GMC with on-going star formation, in order to connect the state of the ISM to the in situ star foramtion. I participated in the observations and reduction of the ammonia spectra analysed in this chapter during my MSc.

5.1 Introduction

The full-sky survey performed by the Planck satellite (Tauber et al., 2010) has provided an inventory of the cold condensations of interstellar matter in the Galaxy. It covered the submm-to-mm range with unprecedented sensitivity. The first all sky catalogue of cold objects, (Cold Clump Catalogue of Planck Objects, C3PO) contains more than 10,000 objects with measured physical properties (Planck Collaboration et al., 2011). Although this is a perfect database to identify the coldest structures in the Galaxy, the lack of sufficient angular resolution of Planck (from 5 to 33 arcmin) prevents to sufficiently characterize the these clouds. The C3PO catalogue is not dominated by cores (pre-stellar or only starless cores at sub-parsec scales) but by ~1 pc sized clumps and even larger cloud structures extending to even tens of pc in size. These objects are likely to contain one or several cores, many of which will be pre-stellar or in the early stages of protostellar evolution. In addition, source confusion on the Galactic

Plane leads to significant incompleteness of the C3PO catalogue on the plane. The European Infrared Space Observatory Herschel opened a unique opportunity to establish in great detail the density and temperature structure of these objects through direct measurements of their thermal dust emission in the far infrared at high angular resolution (from 9" to 30").

The Herschel open time key programme Galactic cold cores project (PI: Mika Juvela, Isabelle Ristorcelli, Juvela et al., 2012, , hereafter Paper III) mapped selected Planck C3PO objects with the Herschel PACS and SPIRE instruments (100-500 μm). The higher spatial resolution of Herschel makes it possible to examine the structure of the sources which gave rise to the Planck detections, often resolving the individual cores. The target selection for Herschel observations was based on a binning of the C3PO objects. The parameter boundaries were the following: l = 0, 60, 120, and 180 degrees, |b| = 1, 5, 10, and 90 degrees, T_{dust} = 6, 9, 11, and 14 K, and M = 0, 0.01, 2.0, 500, 10^6 $M_\odot$. The binning was used to ensure a full coverage of the respective parameter ranges. The final selection of 116 fields covers some 390 cold clumps from the C3PO catalogue. The general properties of a subset of 71 fields were presented by Juvela et al. (2012). This dataset is ideal for statistical analyses – Montillaud et al. (2015, herafter Paper IV) extracted ~4,000 compact sources and published their basic parameters in a catalogue; Rivera-Ingraham et al. (2016, 2017) studied the properties of filaments in a range of environments and star forming conditions; Juvela et al. (2015) analysed the dust properties and Juvela et al. (2018) investigated the column density structures. Fehér et al. (2017) performed a CO follow-up survey and Tóth et al. (in prep) observed a subset of these cores in ammonia with the Effelsberg-100m telescope. In conclusion, there has been considerable effort to chart the physical characteristics of this representative sample of cold clumps, in order to uncover the link between the properties of inter-stellar medium (ISM) and in-situ star-formation.

5.1.1 Selected source – G163.82-8.44

G163.82-8.44 is part of the Auriga-California Molecular Cloud (AMC). Juvela et al. (2012) observed G163.82-8.44 with Herschel PACS and SPIRE instruments within the Herschel open time key programme Galactic Cold Cores. The field contains 17 C3PO objects – see in Panel (a) of Fig. 5.1.

In Paper III G163.82-8.44 was categorized as a filamentary cloud. Most observed fields in the Galactic Cold Core project contain some filamentary structure, but only half of them are dominated by one or a few filaments. G163.82-8.44 is one of the longest (hence likely perpendicular to the line-of-sight) and most striking filaments in this sample. Very clear striations are visible on the Herschel images. Recent studies (e.g. André et al., 2014) suggest that it could be a possible sign of continued accretion.

Rivera-Ingraham et al. (2016) performed a detailed analysis of the filaments of the GCC objects. Linear structures were extracted with the GETFILAMENTS algorithm and characterized according to their radial column density profiles and intrinsic properties (such as N_{H_2} distribution, linear masses, width, stability, local environment and compact source associations).

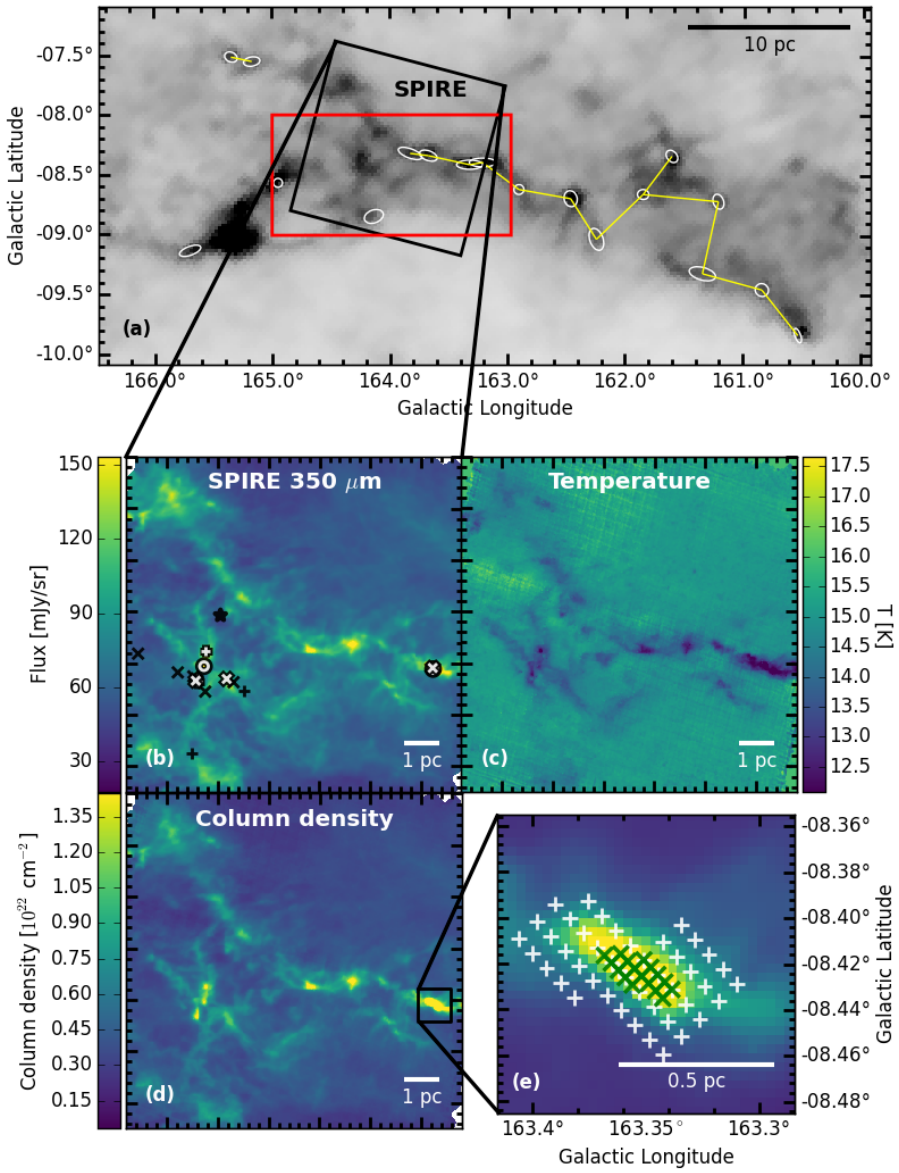

Figure 5.1: **a)** Planck 857GHz intensity map of the G163.82-8.44 region. ECC objects are represented by white ellipses. Position angles were determined on this map. Black and red rectangles indicate the Herschel satellite and Osaka-1.85 m observations, respectively. Yellow lines show the MST structures. **b)** Point source subtracted SPIRE 350μm image of G163.82-8.44. YSO candidates are shown as circles, plus signs, x's and stars for Class 0-I/0, Class I, Class II-flat and Class III sources, respectively. White symbols with black edges indicate the sources from Harvey et al. (2013). Panels **c)**, and **d)**, present the calculated temperature and column density maps, respectively. **e)** Zoomed in column density map of the densest region. White pluses and green crosses show the positions of the NH_3 measurements from 2012 and 2013, respectively. The resolution of (b)-(e) maps is 40".

They found 8 filaments in this field with $N_{scale} > 10$ (priv. comm with A. Rivera-Inghram).

Based on Paper IV, we adopted a distance of 450±23 pc, based on the extinction method. The extinction distance estimate has good quality (i.e. reasonable match between model and observations with a probability of 0.48, due to large number of stars present in the area, and a high significance of 13). It is also in good agreement with kinematic measures from Dame et al. (2001)'s CO survey and Wu et al. (2012)'s pointed observations in CO isotopologues. We note, that Lada et al. (2009) proposed another estimate of ~150 pc based on the presence of small cloud fragments that are associated with the nearby Taurus-Auriga complex, close to the line of sight to the California nebula. In this paper, we adopt the more widely supported 450±23 pc.

Montillaud et al. (2015) found 208 point sources in Herschel images with the use of the GETSOURCES algorithm. 190 of their objects are galactic, 18 are of extragalactic origin. 106 sources are categorised as starless, while 25 are protostellar. These are considered to be cold structures that host young stellar objects (YSOs). The YSOs were selected from the WISE catalogue based on the colour criteria of Koenig et al. (2012). 77 sources have "undetermined" flag in the catalogue. This "undetermined" class contains starless cores with chance alignment with some galactic infrared (IR) sources as well as more evolved prestellar objects.

Zahorecz et al. (in prep) investigated the small scale clustering properties of the ECC cores in Taurus, Auriga, California and Perseus star-forming regions with the use of the Minimal Spanning Tree (Cartwright and Whitworth, 2004, MST,) method. 35 ECC clumps are located in the California region, 5 groups were found: four of them contain only 2-5 clumps and there is a larger, filamentary group with 13 clumps. Fig. 5.1 shows the large, filamentary group and one of the small groups.

5.2 Observations and data analysis

5.2.1 NH_3 observations

We observed the NH_3 emission of a small region with $N_{H2} > 2{\times}10^{22}$ cm^{-2}. The observations were carried out with the Effelsberg 100-m telescope of the Max-Planck-Institut für Radioastronomie, Bonn, during December 12-20, 2012 and December 14-16, 2013. The total on-source integration time was ~4 hours. We used the 13 mm primary receiver of the telescope with frequency switch mode (100 MHz bandwidth and centred on 23710 MHz) to observe the NH_3(1,1) and (2,2) inversion transition lines (at 23694.495 MHz and 23722.633 MHz, respectively), with both linear polarizations simultaneously. The half-power beamwidth at this frequency is 40 arcsec, which corresponds to 0.08 pc at the distance of 450 pc. The pointing errors were within ≈9 arcsec, the velocity resolution obtained was 0.038 km/s. During our first observational run, with an integration time of 15 min, we achieved an *rms* noise of 0.25 K. In the central region, with additional observations of 10 min and 20 min integrations,

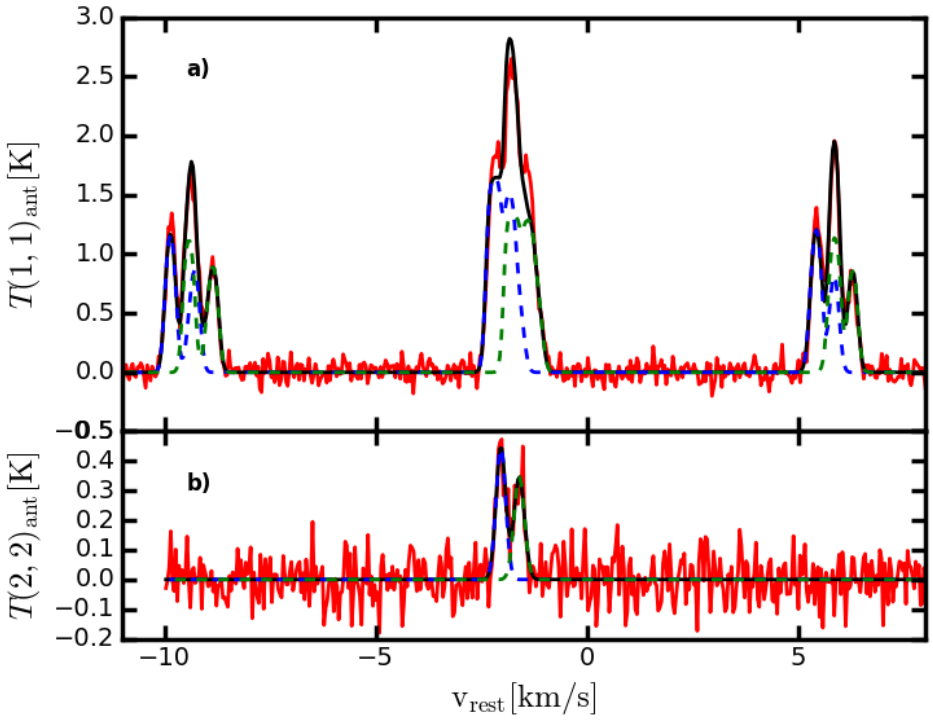

Figure 5.2: a) NH_3 (1,1) and b) (2,2) spectrum at the maximum position. Red lines show the observed spectra, while blue and green lines are the two fitted hyperfine lines with different velocities. Black curve represents the total fitted spectra.

we obtained an *rms* noise of 0.10 K and 0.06 K, respectively. We calibrated the initial spectra using continuum scans of the sources NGC7027 and W3OH (Ott et al., 1994). Data from later epochs were scaled to match our first measurements. Pointing checks were made at least 2-3 hour intervals on nearby continuum sources.

We observed the NH_3 (1,1) and (2,2) transitions in 56 positions (see Fig. 5.1e for pointing positions). Data reduction was performed with the GILDAS packages CLASS and GREG [1] following standard procedures. Fig. 5.2 presents the NH_3 (1,1) and (2,2) spectra in the maximum position with hyperfine structure fits. We clearly identified two velocity components in several positions, suggesting two cloud cores partially overlapped along the line of sight.

5.2.2 3D model of the clump

In order to determine their physical properties, radiative transfer modeling of NH_3 line emission was performed, using a non-LTE Monte-Carlo radiative transfer simulation, called CPPSIMU[2] (Juvela, 1997). The input for CPPSIMU is a model box, whose cells contain physical parameters such as gas volume density, kinetic temperature, line of sight and turbulent velocity components and the observed molecular species' abundance relative to H_2. CPPSIMU propagates a large

[1] http://www.iram.fr/IRAMFR/GILDAS

[2] https://wiki.helsinki.fi/display/~mjuvela@helsinki.fi/Cppsimu

number of photon packages through this model box calculating absorption, scatter and emission in each cell. Mock spectra are produced after convolving the resulting molecular line emission towards the observer with a pre-selected primary beam to simulate the telescope's point spread function. We simulated spectra in spatial grid that matches our observations to facilitate a straightforward model comparison to our data. For the sake of simplicity, our model box was constructed as the sum of two spherically symmetric gas density distributions, aiming to reproduce the observed double line profile. Due to the small number of high signal-to-noise NH_3 (2,2) detections, and consequently not well-resolved kinetic temperature distribution, we assumed that these model spheres are isothermal. We used a Plummer-like profile to describe each spheres' density distributions[3] in the form of

$$\rho(r) = \rho_c \left(1 + \frac{r}{r_c}\right)^{-1}, \tag{5.1}$$

where ρ is the density in a given cell, r the cell's distance from the centre of the core, ρ_c is the critical density, and r_c is the critical radius. The latter two parameters determine the normalization and cut-off distance of the model, and were used as free parameters in our fit.

These model spectra were compared to our NH_3 (1,1) and (2,2) data in 34 positions simultaneously. We optimized the model by tuning nine parameters: each cores' kinetic gas temperature ($T_{kin,1}$, $T_{kin,1}$), cloud core radii (R_1, R_2 – r_c in the Plummer model, see Eq. 5.1), central gas densities (ρ_1, ρ_2 – ρ_c in the Plummer model), both cloud cores' line of sight velocities (v_1, v_2), their turbulent velocities (σ_1, σ_2) and the distance between the cores' centres perpendicular to the line of sight ($dist_z$). All of these parameters were fitted in both cores simultaneously (denoted by indices 1 and 2). The initial parameter values were based on measured ones derived from observations (see Fig. 5.2).

The model optimization was performed with a Bayesian approach, i.e. by maximizing the posterior distribution, $P(\Theta|D)$, defined as:

$$P(\Theta|D) \propto P(D|\Theta) \cdot P(\Theta), \tag{5.2}$$

where Θ represents the set of parameters in our model, D the measured data we wish to fit, $P(\Theta|D)$ is the probability that the model corresponding to Θ is correct given the dataset, $P(D|\Theta)$ is the likelihood function, i.e. the probability of observing the data if the model is true and finally, $P(\Theta)$ is the prior function, i.e. the probability we assign to a given set of model parameters before carrying out the fit. In order to obtain the parameters for a given model that describe the data the best, one needs to find Θ that maximizes the posterior function. In this case, we defined the likelihood as the inverse of chi^2, computed as:

$$\chi^2 = \sum_{i=1}^{N_{spec}} \sum_{j=1}^{N_{chan,j}} \frac{(S_{i,j,\mathrm{obs}} - S_{i,j,\mathrm{mod}})/\sigma}{N_{chan,j}}, \tag{5.3}$$

[3]We note that a Bonnor-Ebert profile based fit yields mass estimates consistent with a Plummer one within 1σ, hence it qualitatively does not change our results.

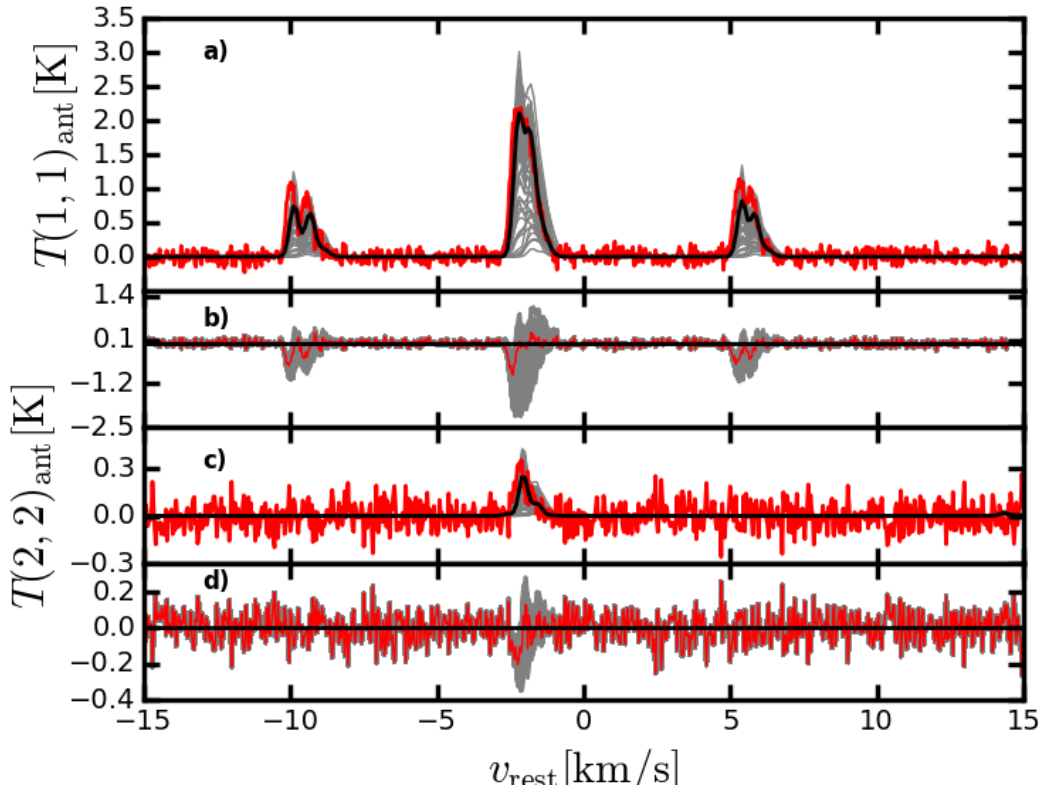

Figure 5.3: A comparison of observed and modelled NH_3 (1,1) and (2,2) spectra at (OFFSET 13). Measurements are shown in red, best fitting model in black, while grey lines are randomly selected models from the Markov chains representing the 1σ confidence intervals. **a)** shows the NH_3 (1,1), **b)** is the residual after subtracting the best fit. Panels **c)** and **d)** are the same with NH_3 (2,2) lines. We note that the relatively large uncertainties arise when we consider several spectra at the same time for our fit.

where N_{spec} is the total number of observed spectra, $N_{chan,j}$ is the total number of frequency channels in the i^{th} spectra, $S_{i,j,\text{obs}}$ ($S_{i,j,\text{mod}}$) is the observed (modelled) flux in the j^{th} channel of the i^{th} spectra, and σ is a weighting factor which equals 1 for (1,1) and 2 for (2,2) spectra. We chose uniform priors, i.e. it is 1 for any possible combination of parameters. Using EMCEE (Foreman-Mackey et al., 2013), a free, open-source Markov chain Monte Carlo (MCMC) sampler implemented in PYTHON, we mapped the posterior distribution to find its maximum. See Fig. 5.3 for an example of the NH_3 (1,1) and (2,2) best-fit lines. Upper and lower errors on each parameter were derived from the 16^{th} and 84^{th} percentiles of their marginalized distributions, respectively (see Fig. 5.4).

We used the posterior distribution to randomly sample gas masses for each cloud separately, obtaining best-fit masses with uncertainties of $M_1 = 68^{+8}_{-13}\text{M}_\odot$ and $M_2 = 4^{+1}_{-1}\text{M}_\odot$ (see Fig 5.5). In order to estimate the error from the **a)** adopted distance uncertainty and **b)** $\sim$ 10 % flux calibration error, we carried out two further MCMC model optimizations with a source distance of 473 pc (i.e. the distance with maximum $1\,\sigma$ uncertainty) and 10 % increased ammonia antenna temperatures, respectively. These yielded gas masses consistent with the initial measurements, thus we conclude they are not the dominant components of the total error, σ_{tot}, on the modelled gas mass. We calculated σ_{tot} using

$$\sigma_{\text{tot}} = \sqrt{\sigma^2_{\text{MCMC}} + \sigma^2_{\text{dist}} + \sigma^2_{\text{flux}}}, \tag{5.4}$$

where σ_{MCMC} is the initial MCMC error estimate from the posterior distribution (see Fig. 5.5), and σ_{dist} and σ_{flux} were taken as the difference between the original best-fit masses and mass estimates from 473 pc and 10 % increased fluxes, respectively. For this two cloud core system we thus obtained mass estimates with total uncertainties of $M_1 = 68^{+11}_{-15}\text{M}_\odot$ and $M_2 = 4^{+2}_{-1}\text{M}_\odot$.

5.3 Conclusion

The Galactic cold cores Herschel open time key programme seeks to investigate the link between the state of ISM and star formation within GMCs. They derived the dust properties of a representative sample of cold interstellar clumps detected by Planck. We obtained NH_3 (1,1) and (2,2) spectra towards the densest cloud cores observed by this programme. This Chapter provided a more detailed study of one particular source in this sample, G163.82-8.44. Our ammonia spectra revealed a double line structure, suggesting that the core is fragmented into two main components. In order to better constrain the physical properties of this double core, we carried out radiative transfer modelling with CPPSIMU. We assumed that the cores are spherical, both are isothermal with a Plummer density profile, and fitted their individual kinetic temperatures, line-of-sight and turbulent velocities, radial sizes, central gas densities and the distance between their centres perpendicular to the line of sight. With a Bayesian approach we obtained realistic errors on each of these parameters. The modelled central gas densities ($\rho_1 = 7.0^{+1.5}_{-0.6} \cdot 10^6 cm^{-3}$ and $\rho_2 = 8.0^{+3.2}_{-2.5} \cdot 10^6 cm^{-3}$) and kinetic temperatures

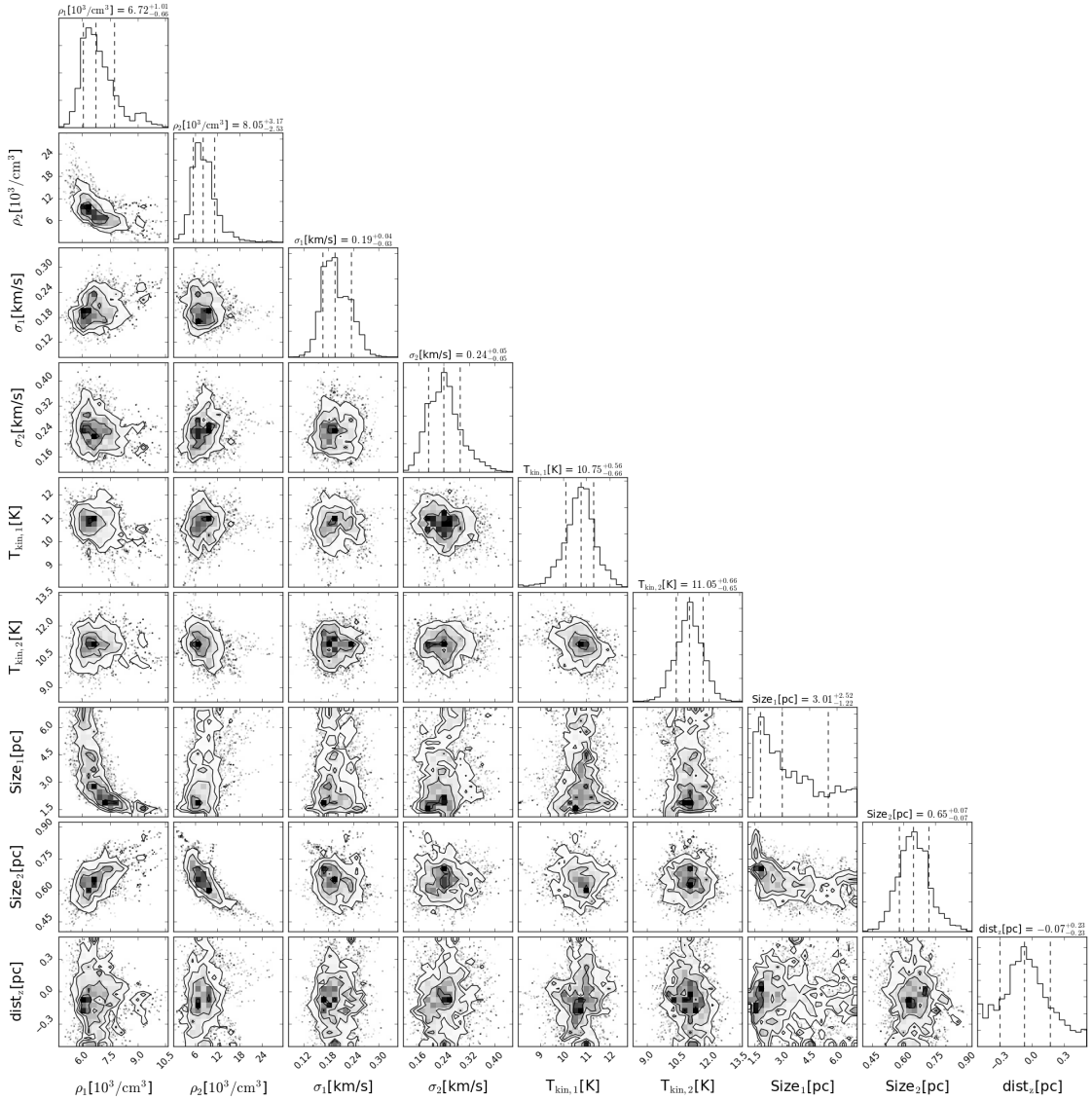

Figure 5.4: Triangle plot with marginalized distributions and cross-correlations of the nine model parameters. Median values and associated errors derived from the 16$^{\text{th}}$ and 84$^{\text{th}}$ percentiles are indicated by dashed lines.

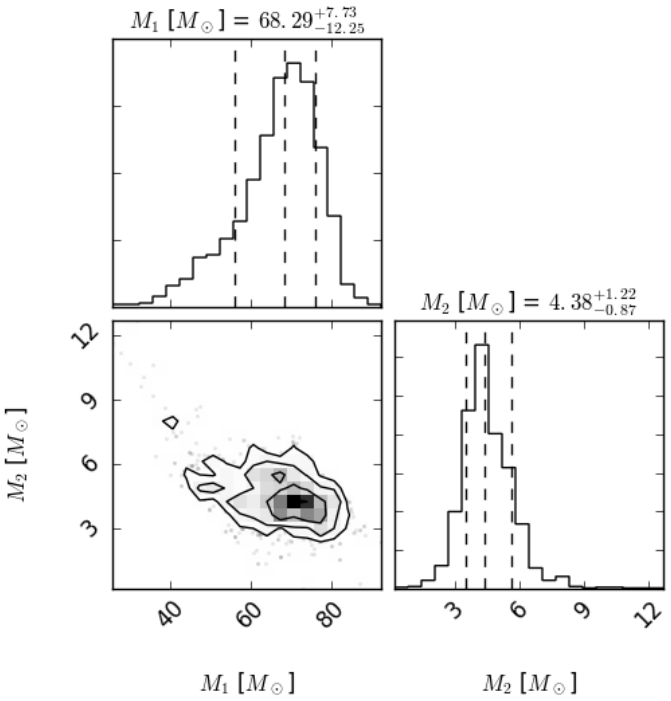

Figure 5.5: Cross-correlation and marginalized distributions of the modelled cloud cores' molecular gas masses. Median values and associated errors derived from the 16$^{\text{th}}$ and 84$^{\text{th}}$ percentiles are indicated by dashed lines.

($T_{\text{kin},1} = 10.8^{+0.6}_{-0.7}$ K and $T_{\text{kin},2} = 11.0^{+0.7}_{-0.7}$ K) are consistent between the two core components within 1 σ, suggesting overall similar ISM conditions within the cores. From the best-fit model we derived gas masses of $M_1 = 68^{+11}_{-15}\text{M}_\odot$ and $M_2 = 4^{+2}_{-1}\text{M}_\odot$. Since the densities are well-matched, this observed mass difference is due to the significantly different core sizes ($R_1 = 3.0^{+2.5}_{-1.2}$ pc and $R_2 = 0.7^{+0.1}_{-0.1}$ pc). Using the MacLaren et al. (1988) formula (Eq. 1.4), we find virial masses of $M_{\text{vir},1} = 254^{+218}_{-114} M_\odot$ and $M_{\text{vir},2} = 70^{+18}_{-18} M_\odot$. These are significantly higher than the measured values, suggesting that the cores are both gravitationally unbound. However, this virial mass estimate neglects the effect of the warmer, enveloping gas component. Thus, the result so far highlights the importance of external pressure in compressing cloud cores and facilitating star formation. Recently observed CO data will be used to extend our stability analysis.

Contribution

My main contributions to this work are implementing the Bayesian modelling approach and calculating gas masses with errors. I wrote the text of Sect. 5.2.2, produced the figures, participated in the observations in 2012, contributed to calibrating and reducing the data. I also provided comments and feedback for the rest of the paper.

Chapter 6

Summary and future work

This thesis has investigated star formation and AGN activity on various spatial scales. In the final chapter, I will give a short summary of the main findings of my works, followed by remarks on some related future research directions I plan to pursue.

6.1 Jet-induced starburst in HE0450–2958?

In my first paper (presented in Chapter 2), I studied feedback processes in an interacting QSO – starburst galaxy pair at z $\approx$ 0.3 using 1 – 6 GHz radio observations.

On sub-arcsecond 5 GHz images I mapped, for the first time, a bipolar outflow centred on the QSO. Its eastern lobe intersects the companion galaxy just north of the concentrated starburst activity at its centre (with gas depletion time-scale of order 10 Myr and a star formation rate of $\approx$ 310 $M_{\odot}$). This star formation related radio component is marginally resolved, thus with spectral bands positioned at 4 and 6 GHz I could probe the radio spectral index's spatial distribution. This revealed tentative evidence for a flattening spectral slope towards the projected point of interaction between the QSO-driven jet and the companion galaxy's interstellar medium (ISM), hinting at on-going physical interaction between them. If this scenario proves favourable, it is possible, that the jet played a crucial role in triggering the starburst – turbulent compression is capable of compressing the gas and thus accelerating HI conversion to H_2, the fuel of star formation. However, current data is not sufficient to firmly rule out a merger-driven star formation with the jet-galaxy alignment being purely a projection effect. Another curious result is the evidence for extended radio flux around the QSO, and radio emission coincident with the optical emission line 'blob', adjacent to the QSO. The former suggests some on-going star formation activity with very little gas and in the presence of a luminous QSO, while the latter raises questions about previous theories regarding the nature of this 'blob'.

Outlook

There are currently two immediate major questions regarding the physical processes in the system: (i) is there any jet-ISM interaction in the companion galaxy, and (ii) what are the main properties of the QSO host galaxy, e.g. in terms of stellar mass and SFR. To answer (i), ALMA observations of e.g. CO and HCN, tracers of warmer, less dense, and cold, high density ISM, respectively, could help. An increasing dense gas ratio towards the jet would provide strong evidence for turbulent compression present in the ISM. Issue (ii) could be resolved by VLBI observations that are only sensitive to < 100 pc scale radio emission near the AGN. A comparison between fluxes obtained this way and our VLA data from an extended array configuration would allow a more robust SFR estimation in the QSO host.

A more general question is the relative importance of systems with positive feedback, especially in the high redshift Universe, where there are some hints that it can be a more common phenomenon (e.g. Decarli et al., 2017). Thanks to the exceptional sensitivity and high resolution (~ 0.5 arcsec at 1 GHz) of SKA, it will provide powerful databases to search for QSO – starburst pairs. These can then be followed up with resolution-matched ALMA observations to probe their ISM. Detailed studies on systems like HE0450-2958 will pave the way to these investigations.

6.2 Radio continuum emission as a star formation tracer

My two other main projects focussed on the details of the radio flux – SFR calibration via the IR-radio correlation. This endeavour is topical, because a new generation of large area, deep radio surveys are on the horizon, aiming to provide a new, more complete census of star forming galaxies at radio frequencies, and their results hinge on the precision of the radio luminosity – SFR conversion. As SKA and its precursors will routinely probe higher than before redshifts, a particularly pressing problem is the redshift evolution of the infrared-radio correlation, a cornerstone of the radio – SFR calibration.

In recent years, a group of studies proposed that the IR-radio ratio ($\overline{q}_{\rm TIR}$) is decreasing as $(1+z)^{-(0.14-0.19)}$. Chapter 3 presents my second paper, which investigates the causes of this redshift trend. I combined the jointly-selected catalogue of Delhaize et al. (2017) (constructed using IR data from Herschel and 3 GHz radio measurements with VLA in the COSMOS field), with optical morphologies from the Zurich Structure and Morphology Catalog. This allowed me to identify disc- and spheroid-dominated star-forming galaxies out to z = 1.5. In order to account for selection effects that arise from a pure radio- or IR-selection criterion, I carried out survival analysis, and thus made use of detection limits as well, to measure median IR-radio ratios in redshift bins. I found that while the IR-radio ratio of spheroid-dominated sources displays a decline proportional to $(1+z)^{-0.19}$, the disc-dominated galaxies show $\overline{q}_{\rm TIR}$ values consistent with the locally measured $\overline{q}_{\rm TIR} = 2.64$ at all $z < 1.5$. Furthermore, I was able to demonstrate that the decrease observed for spheroid-dominated galaxies is due to an increasing

radio excess with redshift, hinting at some low level AGN activity associated with their bulge components, even though according to various diagnostics they harbour no prominent AGN. This result provides important clues for understanding the redshift evolution of the IRRC, and reconciles observations with theoretical models that have predicted opposite (e.g. Lacki and Thompson, 2010). It also demonstrated that radio traces star formation in the absence of AGN contamination in the redshift range covered by our study. Finally, it suggests that a more sophisticated radio – SFR calibration at high-redshifts, that can leverage synergies between upcoming radio and optical surveys, is possible, and will significantly increase the accuracy of SFRs derived from, e.g., SKA data.

Extrapolations to z~0 in deep extragalactic IR-radio correlation (IRRC) studies (Sargent et al., 2010; Delhaize et al., 2017) over predicted the local $\overline{q}_{\rm TIR}$ value, and thus raised concerns, that the more than a decade old local measurements (Yun et al., 2001; Bell, 2003) are not sufficiently reliable. Since then new surveys have provided better data, allowing a revisited, more robust low-redshift measurement of the IRRC. Thus, my following thesis project (described in Chapter 4), attempts to compile the largest and deepest low-z IRRC dataset to date. I used 1.4 GHz radio data from the FIRST and NVSS surveys, and IR fluxes from WISE, IRAS and Herschel. I first measured monochromatic IR-radio relations at many different IR wavelengths (22 – 500 μm), and found that besides the total IRRC, 100 μm luminosities have the tightest correlation with 1.4 GHz radio data in the low-z Universe. Having quantified the selection effects related to the different relative depth of IR and radio measurements, I then carefully re-measured the IR/radio ratios. For the median IR/radio ratio I find a value of $\overline{q}_{\rm TIR}$ = 2.637±0.003[1] for star-forming galaxies, consistent with the result of Bell (2003), however, with a smaller, ~0.2 dex scatter (compared to their 0.26 dex value). This confirms the findings of Bell (2003), and suggests that studies with high $\overline{q}_{\rm TIR}$ values extrapolated to z ~ 0 have some hidden systematics, that need to be corrected for. Interestingly, AGN not only have a lower (by 0.4 dex) median $\overline{q}_{\rm TIR}$ = 2.60±0.02, but also a larger (by 0.7 dex), 0.27 dex scatter. I find evidence for a decreasing $\overline{q}_{\rm TIR}$ towards high radio luminosities for both star-forming galaxies and AGN. Once the catalogue is finalised and the paper is published, it will be released to the public. With rich ancillary data, it is designed to form the basis of more multi-variate studies of the IR-radio relation.

Outlook

We plan to inspect the IRRC in the multi-dimensional parameter space of various physical properties, such as stellar and gas masses (from e.g. the COLDGASS survey; Saintonge et al., 2011), or metallicities (using SDSS spectra). Adding a more nuanced AGN classification is also possible using SDSS optical line measurements, similar to the work by Morić et al. (2010). This opens up several avenues of follow-up research that are capable of dissecting the

[1]The error estimates are only formal errors on the mean, and do not contain the possibly larger systematics yet.

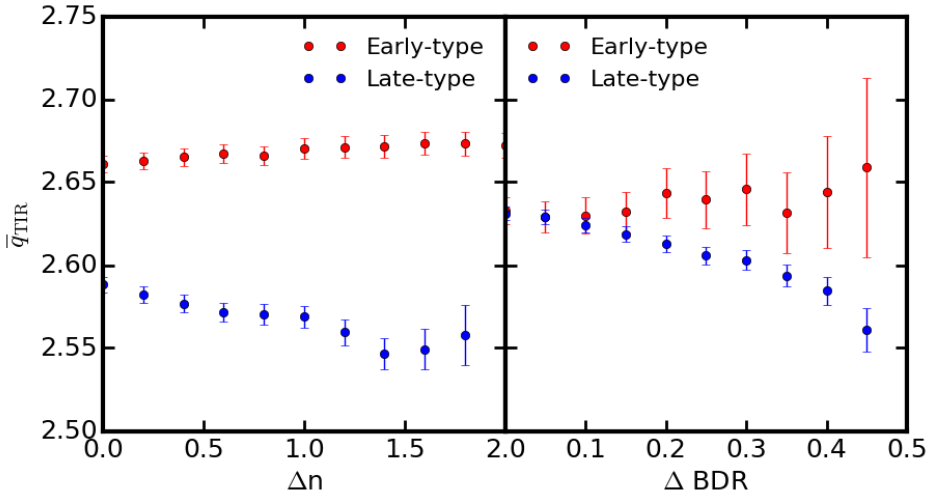

Figure 6.1: Median IR-radio ratios of early- and late-type star-forming galaxies in our low-z sample as a function of the selection criteria. On the left hand panel, Δn is the gap between Sérsic-indices used to separate early- and late-type galaxies. At $\Delta n = 0$ early-types are galaxies with $n > 1.5$ and late-types have $n < 1.5$. Similarly, in the right figure, bulge-to-disc ratio is used to separate early- and late-types, where ΔBDR = 0 corresponds to early-types being sources with > 0.5 and late-types < 0.5 bulge-to-disc ratios.

IRRC in order to learn more about its underlying physics. As a first effort in this direction, and to check the low-z fits in my work shown in Chapter 3 (anchored to z = 0 data from Bell 2003), I cross-matched the low-z galaxies with the morphological catalogue of Simard et al. (2011). They carried out Sérsic-index fitting and measured bulge-to-disk ratios in SDSS images of isolated sources. My first results find systematically higher $q_{\rm TIR}$ values for early-type galaxies, possibly due to their relatively stronger cirrus emission (in agreement with the results of e.g. Nyland et al., 2017). In fact, the $\overline{q}_{\rm TIR}$ difference between early- and late-type sources seem to increase by using more 'extreme' selections for these morphological classes, as shown in Fig. 6.1. However, the specific values depend on the precise criteria used to selecting morphological samples (e.g. whether it is based on Sérsic-indices or bulge-to-disc ratios), hence it requires more investigation to chose the most appropriate definition of early- and late-type galaxies in our sample. Nevertheless, this preliminary result is in line with my predictions at low redshifts in Chapter 4, and thus it is planned to form the basis of a letter that ties together my papers in Chapter 3 and 4.

There are some further tasks to be done before the results of Chapter 4 can be published. Calculating errors on all IRRC statistics from individual luminosity uncertainties is possible, since my SED fitting code extracts $16^{\rm th}$ and $84^{\rm th}$ percentiles (i.e. $\pm\,1\,\sigma$ uncertainty) of the marginalized $L_{\rm TIR}$ distributions, and errors on radio fluxes are available in the Unified Radio Catalog. However, these errors are often significantly smaller than the scatter of the IRRC,

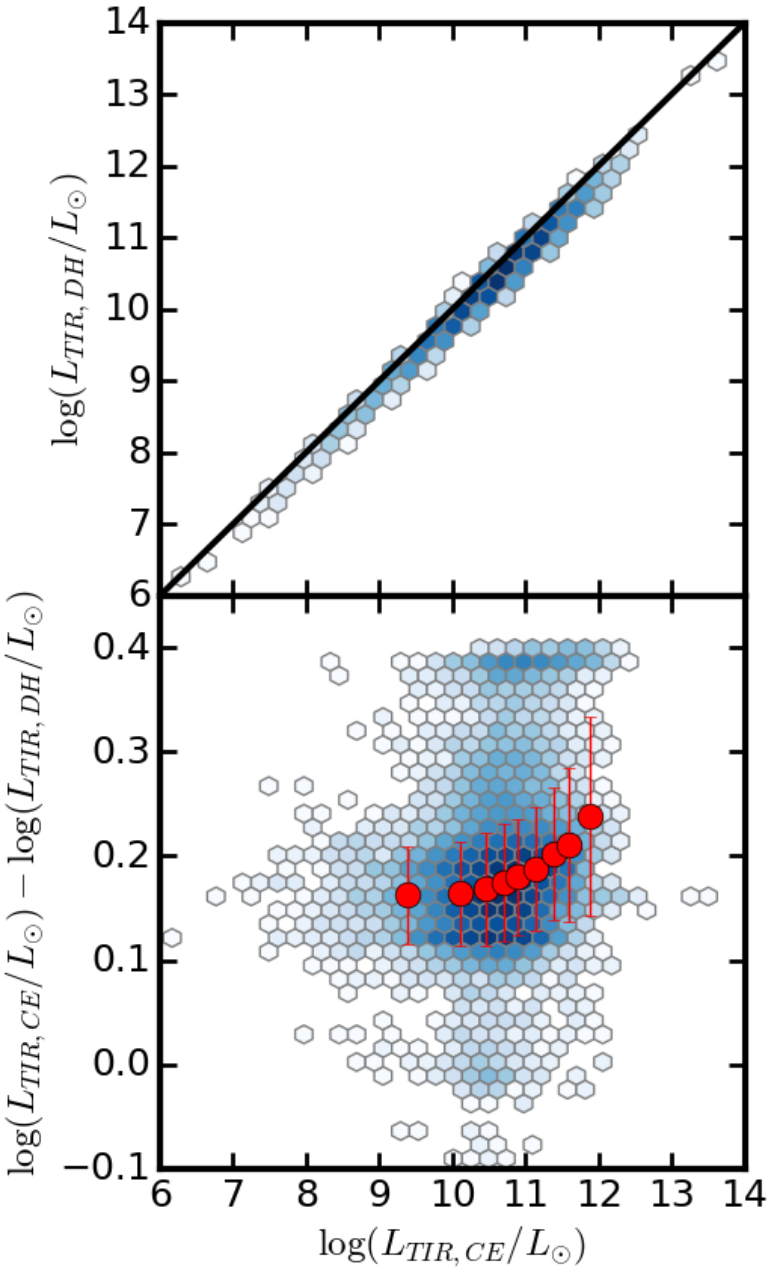

Figure 6.2: **Top**: comparison of $L_{\rm TIR}$ values obtained by using SED template libraries from Chary and Elbaz (2001) (x-axis) and Dale and Helou (2002) (y-axis). Black line represents the 1:1 relation. **Bottom:** difference of the two fits as a function of luminosity from Chary and Elbaz (2001) templates. Red points are the mean differences in $L_{TIR,CE}$ bins (same as the bins in Fig. 4.11), while errorbars represent the standard deviation in each bin. Dale and Helou (2002) fits on average return 0.17 dex lower $L_{\rm TIR}$ estimates, with a $\sim$ 0.5 dex increase towards high luminosities. There is a smaller locus of sources around 0.4 dex difference.

thus add very little to the uncertainty of the measured statistics, suggesting that the total error budget is dominated by systematics (such as the choice of IR template library used for SED fitting, choice of adopted radio spectral index, uncertainty of the flux cut used to create the sensitivity-matched sample, etc.), that need to be carefully taken into account. As a step in this direction, I have carried out IR fits with the SED library of Dale and Helou (2002). A comparison between $L_{\rm TIR}$ values obtained from Dale and Helou (2002) and Chary and Elbaz (2001) templates reveal systematic differences, as Fig. 6.2 shows. On average, $L_{\rm TIR}$ measured by Dale and Helou (2002) are $\sim 0.17\pm0.06$ dex lower than by the Chary and Elbaz (2001) fits, with a slight luminosity dependence in the $10 \leq \log(L_{\rm TIR}/L_{\odot}) \leq 12$ range. This systematic difference warrants further investigation. A possible solution could be to merge the two template libraries and carry out a joint SED fit, similar to the approach of e.g. Calistro Rivera et al. (2016).

Currently, I do not make use of the limits at radio and IR wavelengths in the low-z catalogue. A logical improvement of the study will be to try to obtain $\overline{q}_{\rm TIR}$ values from survival analysis, which would ideally negate the need for a flux-selection. Alternatively, stacking could be used to explore sources with low radio and IR fluxes.

6.3 Modelling ammonia lines in Galactic cloud cores

Finally, I collaborated on analysing ammonia spectra from a Galactic GMC core observed by the Effelsberg-100m telescope. The data are from the Auriga-California Molecular Cloud, at $\sim$ 450 pc. We found double line emission, suggesting two close cloud cores along the line of sight, possible progenitors of a future binary star. I applied the Bayesian model fitting technique with MCMC, that I also used for IR SED fits in Chapter 4, to optimise the physical parameters of a model cloud. Mock observations from our model cloud cores were calculated by a radiative transfer code called CPPSIMU. This allowed me to carefully explore the nine dimensional parameter space of the model, and thus lead to reliable error estimates for the two cores' gas masses. We found a a mass ratio of 17:1.

Outlook

The modelled physical characteristics will be used to examine the cores' gravitational stability. First calculations using the MacLaren et al. (1988) formula (Eq. 1.4) find virial masses of $M_{\rm vir,1} = 254^{+218}_{-114} M_{\odot}$ and $M_{\rm vir,2} = 70^{+18}_{-18} M_{\odot}$. This are significantly higher than the measured $M_1 = 68^{+11}_{-15} M_{\odot}$ and $M_2 = 4^{+2}_{-1} M_{\odot}$ values, suggesting that the cores need to accrete more material before they become gravitationally bound and collapse. An investigation of the velocity field in their vicinity can provide clues about accretion rates and support or disprove this picture. Molecular hydrogen column densities obtained from FIR-based dust column density estimates (assuming a given gas-to-dust ratio) will be compared to H_2 column densities inferred from our ammonia data. This will be a test whether typical 10^{-8} ammonia abundances

with respect to H_2 are accurate in these cores, and will contribute to analysing their chemical evolutionary status (in conjunction with other molecular species). Finally, the mass ratios will be compared to typical young binary star mass ratios.

Bibliography

Alam, S., Albareti, F. D., Allende Prieto, C., Anders, F., Anderson, S. F., et al. (2015). The Eleventh and Twelfth Data Releases of the Sloan Digital Sky Survey: Final Data from SDSS-III. *ApJS*, 219:12. 81

André, P., Di Francesco, J., Ward-Thompson, D., Inutsuka, S.-I., Pudritz, R. E., and Pineda, J. E. (2014). From Filamentary Networks to Dense Cores in Molecular Clouds: Toward a New Paradigm for Star Formation. *Protostars and Planets VI*, pages 27–51. 105

Appleton, P. N., Fadda, D. T., Marleau, F. R., Frayer, D. T., Helou, G., et al. (2004). The Far- and Mid-Infrared/Radio Correlations in the Spitzer Extragalactic First Look Survey. *ApJS*, 154:147–150. 56

Baldwin, J. A., Phillips, M. M., and Terlevich, R. (1981). Classification parameters for the emission-line spectra of extragalactic objects. *PASP*, 93:5–19. 21

Becker, R. H., White, R. L., and Helfand, D. J. (1995). The FIRST Survey: Faint Images of the Radio Sky at Twenty Centimeters. *ApJ*, 450:559. 86

Begelman, M. C. and Cioffi, D. F. (1989). Overpressured cocoons in extragalactic radio sources. *ApJ*, 345:L21–L24. 32

Bell, E. F. (2003). Estimating Star Formation Rates from Infrared and Radio Luminosities: The Origin of the Radio-Infrared Correlation. *ApJ*, 586:794–813. 45, 50, 56, 57, 67, 68, 71, 75, 78, 79, 80, 82, 86, 92, 93, 95, 96, 98, 99, 116, 117

Berta, S., Lutz, D., Santini, P., Wuyts, S., Rosario, D., et al. (2013). Panchromatic spectral energy distributions of Herschel sources. *A&A*, 551:A100. 62

Bianchi, S., Giovanardi, C., Smith, M. W. L., Fritz, J., Davies, J. I., et al. (2017). The Herschel Virgo Cluster Survey. XX. Dust and gas in the foreground Galactic cirrus. *A&A*, 597:A130. 76

Bourne, N., Dunne, L., Maddox, S. J., Dye, S., Furlanetto, C., et al. (2016). The Herschel-ATLAS Data Release 1 - II. Multi-wavelength counterparts to submillimetre sources. *MNRAS*, 462:1714–1734. 85

Boyce, P. J., Disney, M. J., Blades, J. C., Boksenberg, A., Crane, P., et al. (1996). The Host Galaxies of IRAS-selected Quasi-stellar Objects. *ApJ*, 473:760. 33

Bridle, A. H., Hough, D. H., Lonsdale, C. J., Burns, J. O., and Laing, R. A. (1994). Deep VLA imaging of twelve extended 3CR quasars. *AJ*, 108:766–820. 8

Briggs, D. S. (1995). High Fidelity Interferometric Imaging: Robust Weighting and NNLS Deconvolution. In *American Astronomical Society Meeting Abstracts*, volume 27 of *Bulletin of the American Astronomical Society*, page 1444. 27

Brinchmann, J., Charlot, S., White, S. D. M., Tremonti, C., Kauffmann, G., et al. (2004). The physical properties of star-forming galaxies in the low-redshift Universe. *MNRAS*, 351:1151–1179. 5

Calistro Rivera, G., Lusso, E., Hennawi, J. F., and Hogg, D. W. (2016). AGNfitter: A Bayesian MCMC Approach to Fitting Spectral Energy Distributions of AGNs. *ApJ*, 833:98. 22, 119

Calistro Rivera, G., Williams, W. L., Hardcastle, M. J., Duncan, K., Röttgering, H. J. A., et al. (2017). The LOFAR window on star-forming galaxies and AGNs - curved radio SEDs and IR-radio correlation at $0 < z < 2.5$. *MNRAS*, 469:3468–3488. 29, 57, 79, 98

Carilli, C. L. and Yun, M. S. (1999). The Radio-to-Submillimeter Spectral Index as a Redshift Indicator. *ApJ*, 513:L13–L16. 56

Carlstrom, J. E. and Kronberg, P. P. (1991). H II regions in M82 - High-resolution millimeter continuum observations. *ApJ*, 366:422–431. 19

Cartwright, A. and Whitworth, A. P. (2004). The statistical analysis of star clusters. *MNRAS*, 348:589–598. 107

Casey, C. M., Chen, C.-C., Cowie, L. L., Barger, A. J., Capak, P., et al. (2013). Characterization of SCUBA-2 450 μm and 850 μm selected galaxies in the COSMOS field. *MNRAS*, 436:1919–1954. 65

Chabrier, G. (2003). Galactic Stellar and Substellar Initial Mass Function. *PASP*, 115:763–795. 4, 63, 74, 81

Chapman, S. C., Blain, A. W., Smail, I., and Ivison, R. J. (2005). A Redshift Survey of the Submillimeter Galaxy Population. *ApJ*, 622:772–796. 56

Charmandaris, V., Combes, F., and van der Hulst, J. M. (2000). First detection of molecular gas in the shells of CenA. *A&A*, 356:L1–L4. 13, 52

Chary, R. and Elbaz, D. (2001). Interpreting the Cosmic Infrared Background: Constraints on the Evolution of the Dust-enshrouded Star Formation Rate. *ApJ*, 556:562–581. 81, 82, 86, 88, 89, 118, 119

Ciliegi, P. and Bardelli, S. (2015). Synergistic science with Euclid and SKA: the nature and history of Star Formation. *Advancing Astrophysics with the Square Kilometre Array (AASKA14)*, page 150. 77

Civano, F., Elvis, M., Brusa, M., Comastri, A., Salvato, M., et al. (2012). The Chandra COSMOS Survey. III. Optical and Infrared Identification of X-Ray Point Sources. *ApJS*, 201:30. 62

Civano, F., Marchesi, S., Comastri, A., Urry, M. C., Elvis, M., et al. (2016). The Chandra Cosmos Legacy Survey: Overview and Point Source Catalog. *ApJ*, 819:62. 62

Clark, B. G. (1980). An efficient implementation of the algorithm 'CLEAN'. *A&A*, 89:377. 27

Condon, J. J. (1992). Radio emission from normal galaxies. *ARA&A*, 30:575–611. 18, 19, 20, 23, 39, 56, 57, 79

Condon, J. J., Cotton, W. D., Greisen, E. W., Yin, Q. F., Perley, R. A., Taylor, G. B., and Broderick, J. J. (1998). The NRAO VLA Sky Survey. *AJ*, 115:1693–1716. 28, 79, 86

Cornwell, T. J. and Evans, K. F. (1985). A simple maximum entropy deconvolution algorithm. *A&A*, 143:77–83. 28

Cresci, G., Mainieri, V., Brusa, M., Marconi, A., Perna, M., et al. (2015). Blowin' in the Wind: Both "Negative" and "Positive" Feedback in an Obscured High-z Quasar. *ApJ*, 799:82. 35

Croft, S., van Breugel, W., de Vries, W., Dopita, M., Martin, C., et al. (2006). Minkowski's Object: A Starburst Triggered by a Radio Jet, Revisited. *ApJ*, 647:1040–1055. 13, 35, 52

Croton, D. J., Stevens, A. R. H., Tonini, C., Garel, T., Bernyk, M., Bibiano, A., et al. (2016). Semi-Analytic Galaxy Evolution (SAGE): Model Calibration and Basic Results. *ApJS*, 222:22. 14

da Cunha, E., Charlot, S., and Elbaz, D. (2008). A simple model to interpret the ultraviolet, optical and infrared emission from galaxies. *MNRAS*, 388:1595–1617. 17, 65

Dale, D. A. and Helou, G. (2002). The Infrared Spectral Energy Distribution of Normal Star-forming Galaxies: Calibration at Far-Infrared and Submillimeter Wavelengths. *ApJ*, 576:159–168. 118, 119

Dame, T. M., Hartmann, D., and Thaddeus, P. (2001). The Milky Way in Molecular Clouds: A New Complete CO Survey. *ApJ*, 547:792–813. 107

Davies, L. J. M., Huynh, M. T., Hopkins, A. M., Seymour, N., Driver, S. P., et al. (2017). Galaxy And Mass Assembly: the 1.4 GHz SFR indicator, SFR-M_* relation and predictions for ASKAP-GAMA. *MNRAS*, 466:2312–2324. 20, 56

De Breuck, C., Downes, D., Neri, R., van Breugel, W., Reuland, M., et al. (2005). Detection of two massive CO systems in 4C 41.17 at z = 3.8. *A&A*, 430:L1–L4. 52

de Bruyn, A. G. and Wilson, A. S. (1978). The radio properties of Seyfert galaxies. *A&A*, 64:433–444. 39

de Grijp, M. H. K., Lub, J., and Miley, G. K. (1987). Warm IRAS sources. I. A. Catalogue of AGN candidates from the point source catalog. *A&AS*, 70:95–114. 33

de Jong, T., Klein, U., Wielebinski, R., and Wunderlich, E. (1985). Radio continuum and far-infrared emission from spiral galaxies - A close correlation. *A&A*, 147:L6–L9. 20, 56, 79

de Vaucouleurs, G., de Vaucouleurs, A., Corwin, Jr., H. G., Buta, R. J., Paturel, G., and Fouqué, P. (1991). *Third Reference Catalogue of Bright Galaxies. Volume I: Explanations and references. Volume II: Data for galaxies between 0^h and 12^h. Volume III: Data for galaxies between 12^h and 24^h*. 59

Decarli, R., Walter, F., Venemans, B. P., Bañados, E., Bertoldi, F., et al. (2017). Rapidly star-forming galaxies adjacent to quasars at redshifts exceeding 6. *Nature*, 545:457–461. 13, 115

Del Moro, A., Alexander, D. M., Mullaney, J. R., Daddi, E., Pannella, M., et al. (2013). GOODS-Herschel: radio-excess signature of hidden AGN activity in distant star-forming galaxies. *A&A*, 549:A59. 21, 56

Delhaize, J., Smolčić, V., Delvecchio, I., Novak, M., Sargent, M., et al. (2017). The VLA-COSMOS 3 GHz Large Project: The infrared-radio correlation of star-forming galaxies and AGN to z < 6; D17. *A&A*, 602:A4. 56, 57, 79, 98, 115, 116

Delvecchio, I., Gruppioni, C., Pozzi, F., Berta, S., Zamorani, G., et al. (2014). Tracing the cosmic growth of supermassive black holes to z ∼ 3 with Herschel. *MNRAS*, 439:2736–2754. 62

Delvecchio, I., Smolčić, V., Zamorani, G., Lagos, C. D. P., Berta, S., et al. (2017). The VLA-COSMOS 3 GHz Large Project: AGN and host-galaxy properties out to z < 6. *A&A*, 602:A3. 62, 65

Donley, J. L., Koekemoer, A. M., Brusa, M., Capak, P., Cardamone, C. N., et al. (2012). Identifying Luminous Active Galactic Nuclei in Deep Surveys: Revised IRAC Selection Criteria. *ApJ*, 748:142. 21, 62

Donley, J. L., Rieke, G. H., Rigby, J. R., and Pérez-González, P. G. (2005). Unveiling a Population of AGNs Not Detected in X-Rays. *ApJ*, 634:169–182. 21, 56

Downes, D. and Solomon, P. M. (1998). Rotating Nuclear Rings and Extreme Starbursts in Ultraluminous Galaxies. *ApJ*, 507:615–654. 51

Driver, S. P., Hill, D. T., Kelvin, L. S., Robotham, A. S. G., Liske, J., Norberg, P., et al. (2011). Galaxy and Mass Assembly (GAMA): survey diagnostics and core data release. *MNRAS*, 413:971–995. 84

Eales, S., Dunne, L., Clements, D., Cooray, A., De Zotti, G., et al. (2010). The Herschel ATLAS. *PASP*, 122:499. 84

Elbaz, D., Daddi, E., Le Borgne, D., Dickinson, M., Alexander, D. M., et al. (2007). The reversal of the star formation-density relation in the distant universe. *A&A*, 468:33–48. 5

Elbaz, D., Dickinson, M., Hwang, H. S., Díaz-Santos, T., Magdis, G., et al. (2011). GOODS-Herschel: an infrared main sequence for star-forming galaxies. *A&A*, 533:A119. 5

Elbaz, D., Jahnke, K., Pantin, E., Le Borgne, D., and Letawe, G. (2009). Quasar induced galaxy formation: a new paradigm? *A&A*, 507:1359–1374. 32, 33, 35, 36, 43, 45, 47, 50, 51

Elvis, M., Civano, F., Vignali, C., Puccetti, S., Fiore, F., et al. (2009). The Chandra COSMOS Survey. I. Overview and Point Source Catalog. *ApJS*, 184:158–171. 62

Fabian, A. C. (2012). Observational Evidence of Active Galactic Nuclei Feedback. *ARA&A*, 50:455–489. 13, 32

Fanaroff, B. L. and Riley, J. M. (1974). The morphology of extragalactic radio sources of high and low luminosity. *MNRAS*, 167:31P–36P. 7

Fanti, C., Fanti, R., Dallacasa, D., Schilizzi, R. T., Spencer, R. E., and Stanghellini, C. (1995). Are compact steep-spectrum sources young? *A&A*, 302:317. 47

Feain, I. J., Papadopoulos, P. P., Ekers, R. D., and Middelberg, E. (2007). Dressing a Naked Quasar: Star Formation and Active Galactic Nucleus Feedback in HE 0450-2958. *ApJ*, 662:872–877. 33, 34, 35, 36, 37, 38, 39, 40, 42, 43, 44, 47, 49, 50

Fehér, O., Juvela, M., Lunttila, T., Montillaud, J., Ristorcelli, I., and others, L. V. (2017). A CO survey on a sample of Herschel cold clumps. *A&A*, 606:A102. 105

Ferrarese, L., Côté, P., Dalla Bontà, E., Peng, E. W., Merritt, D., et al. (2006). A Fundamental Relation between Compact Stellar Nuclei, Supermassive Black Holes, and Their Host Galaxies. *ApJ*, 644:L21–L24. 14, 32

Ferrarese, L. and Merritt, D. (2000). A Fundamental Relation between Supermassive Black Holes and Their Host Galaxies. *ApJ*, 539:L9–L12. 14, 32

Ferrière, K. M. (2001). The interstellar environment of our galaxy. *Reviews of Modern Physics*, 73:1031–1066. 10

Foreman-Mackey, D., Hogg, D. W., Lang, D., and Goodman, J. (2013). emcee: The MCMC Hammer. *PASP*, 125:306. 111

Frei, Z., Guhathakurta, P., Gunn, J. E., and Tyson, J. A. (1996). A Catalog of Digital Images of 113 Nearby Galaxies. *AJ*, 111:174. 59

Gaibler, V., Khochfar, S., Krause, M., and Silk, J. (2012). Jet-induced star formation in gas-rich galaxies. *MNRAS*, 425:438–449. 32

Garn, T., Green, D. A., Riley, J. M., and Alexander, P. (2009). The relationship between star formation rate and radio synchrotron luminosity at 0 < z < 2. *MNRAS*, 397:1101–1112. 56

Garrett, M. A. (2002). The FIR/Radio correlation of high redshift galaxies in the region of the HDF-N. *A&A*, 384:L19–L22. 56

Gebhardt, K., Bender, R., Bower, G., Dressler, A., Faber, S. M., et al. (2000). A Relationship between Nuclear Black Hole Mass and Galaxy Velocity Dispersion. *ApJ*, 539:L13–L16. 32

Gilli, R., Comastri, A., and Hasinger, G. (2007). The synthesis of the cosmic X-ray background in the Chandra and XMM-Newton era. *A&A*, 463:79–96. 74

Glover, S. C. O. and Mac Low, M.-M. (2007). Simulating the Formation of Molecular Clouds. II. Rapid Formation from Turbulent Initial Conditions. *ApJ*, 659:1317–1337. 13

Griffin, M. J., Abergel, A., Abreu, A., Ade, P. A. R., André, P., et al. (2010). The Herschel-SPIRE instrument and its in-flight performance. *A&A*, 518:L3. 84

Gu, Y., Fang, G., Yuan, Q., Cai, Z., and Wang, T. (2018). The Morphological Evolution, AGN Fractions, Dust Content, Environments, and Downsizing of Massive Green Valley Galaxies at 0.5 < z < 2.5 in 3D-HST/CANDELS. *ApJ*, 855:10. 6

Gürkan, G., Hardcastle, M. J., Smith, D. J. B., Best, P. N., Bourne, N., et al. (2018). LOFAR/H-ATLAS: the low-frequency radio luminosity-star formation rate relation. *MNRAS*, 475:3010–3028. 29

Harvey, P. M., Fallscheer, C., Ginsburg, A., Terebey, S., André, P., et al. (2013). A First Look at the Auriga-California Giant Molecular Cloud with Herschel and the CSO: Census of the Young Stellar Objects and the Dense Gas. *ApJ*, 764:133. 106

Hazard, C., Mackey, M. B., and Shimmins, A. J. (1963). Investigation of the Radio Source 3C 273 By The Method of Lunar Occultations. *Nature*, 197:1037–1039. 6

Helfand, D. J., White, R. L., and Becker, R. H. (2015). The Last of FIRST: The Final Catalog and Source Identifications. *ApJ*, 801:26. 28, 86

Helou, G. and Bicay, M. D. (1993). A physical model of the infrared-to-radio correlation in galaxies. *ApJ*, 415:93–100. 57

Helou, G., Soifer, B. T., and Rowan-Robinson, M. (1985). Thermal infrared and nonthermal radio - Remarkable correlation in disks of galaxies. *ApJ*, 298:L7–L11. 20, 56, 79

Henriques, B. M. B., White, S. D. M., Thomas, P. A., Angulo, R., Guo, Q., et al. (2015). Galaxy formation in the Planck cosmology - I. Matching the observed evolution of star formation rates, colours and stellar masses. *MNRAS*, 451:2663–2680. 14

Högbom, J. A. (1974). Aperture Synthesis with a Non-Regular Distribution of Interferometer Baselines. *A&AS*, 15:417. 27

Hubble, E. (1929a). A Relation between Distance and Radial Velocity among Extra-Galactic Nebulae. *Proceedings of the National Academy of Science*, 15:168–173. 2

Hubble, E. P. (1929b). A spiral nebula as a stellar system, Messier 31. *ApJ*, 69. 2

Hubble, E. P. (1936). *Realm of the Nebulae*. 3

Hwang, H. S., Elbaz, D., Dickinson, M., Charmandaris, V., Daddi, E., et al. (2011). GOODS-Herschel: the impact of galaxy-galaxy interactions on the far-infrared properties of galaxies. *A&A*, 535:A60. 52

Ibar, E., Cirasuolo, M., Ivison, R., Best, P., Smail, I., et al. (2008). Exploring the infrared/radio correlation at high redshift. *MNRAS*, 386:953–962. 56

Ivison, R. J., Magnelli, B., Ibar, E., Andreani, P., Elbaz, D., et al. (2010). The far-infrared/radio correlation as probed by Herschel. *A&A*, 518:L31. 79

Jahnke, K. and Macciò, A. V. (2011). The Non-causal Origin of the Black-hole-galaxy Scaling Relations. *ApJ*, 734:92. 14, 32

Jarvis, M. J., Smith, D. J. B., Bonfield, D. G., Hardcastle, M. J., Falder, J. T., et al. (2010). Herschel-ATLAS: the far-infrared-radio correlation at z < 0.5. *MNRAS*, 409:92–101. 56

Jarvis, M. J., Taylor, A. R., Agudo, I., Allison, J. R., Deane, R. P., et al. (2017). The MeerKAT International GHz Tiered Extragalactic Exploration (MIGHTEE) Survey. *ArXiv e-prints*. 29

Jeans, J. H. (1902). The Stability of a Spherical Nebula. *Philosophical Transactions of the Royal Society of London Series A*, 199:1–53. 11

Johnston, S., Taylor, R., Bailes, M., Bartel, N., Baugh, C., et al. (2008). Science with ASKAP. The Australian square-kilometre-array pathfinder. *Experimental Astronomy*, 22:151–273. 20

Juvela, M. (1997). Non-LTE radiative transfer in clumpy molecular clouds. *A&A*, 322:943–961. 108

Juvela, M., Malinen, J., Montillaud, J., Pelkonen, V.-M., Ristorcelli, I., and Toth, L. V. (2018). Galactic cold cores IX. Column density structures and radiative transfer modelling. *ArXiv e-prints*. 105

Juvela, M., Ristorcelli, I., Marshall, D. J., Montillaud, J., Pelkonen, V.-M., et al. (2015). Galactic cold cores. V. Dust opacity. *A&A*, 584:A93. 105

Juvela, M., Ristorcelli, I., Pagani, L., Doi, Y., Pelkonen, V.-M., et al. (2012). Galactic cold cores. III. General cloud properties. *A&A*, 541:A12. 105

Kalberla, P. M. W. and Kerp, J. (2009). The Hi Distribution of the Milky Way. *ARA&A*, 47:27–61. 10

Kaplan, E. L. and Meier, P. (1958). Nonparametric estimation from incomplete observations. *Journal of the American Statistical Association*, 53:457–481. 66

Kennicutt, Jr., R. C. (1998). The Global Schmidt Law in Star-forming Galaxies. *ApJ*, 498:541–552. 63, 74

Kewley, L. J., Groves, B., Kauffmann, G., and Heckman, T. (2006). The host galaxies and classification of active galactic nuclei. *MNRAS*, 372:961–976. 21

Kimball, A. E. and Ivezić, Ž. (2008). A Unified Catalog of Radio Objects Detected by NVSS, First, WENSS, GB6, and SDSS. *AJ*, 136:684–712. 18, 86, 88

Kimball, A. E. and Ivezić, Ž. (2014). An Updated Version of the Unified Radio Catalog: A Multi-Wavelength Radio and Optical Catalog of Quasars and Radio Galaxies. *ArXiv e-prints*. 86

Klein, U., Wielebinski, R., and Morsi, H. W. (1988). Radio continuum observations of M82. *A&A*, 190:41–46. 19

Koekemoer, A. M., Aussel, H., Calzetti, D., Capak, P., Giavalisco, M., et al. (2007). The COSMOS Survey: Hubble Space Telescope Advanced Camera for Surveys Observations and Data Processing. *ApJS*, 172:196–202. 59

Koenig, X. P., Leisawitz, D. T., Benford, D. J., Rebull, L. M., Padgett, D. L., and Assef, R. J. (2012). Wide-field Infrared Survey Explorer Observations of the Evolution of Massive Star-forming Regions. *ApJ*, 744:130. 107

Kormendy, J. and Gebhardt, K. (2001). Supermassive black holes in galactic nuclei. In Wheeler, J. C. and Martel, H., editors, *20th Texas Symposium on relativistic astrophysics*, volume 586 of *American Institute of Physics Conference Series*, pages 363–381. 32

Kormendy, J. and Richstone, D. (1995). Inward Bound—The Search For Supermassive Black Holes In Galactic Nuclei. *ARA&A*, 33:581. 32

Kroupa, P. (2001). On the variation of the initial mass function. *MNRAS*, 322:231–246. 4

Lacey, C. G., Baugh, C. M., Frenk, C. S., Benson, A. J., Bower, R. G., et al. (2016). A unified multiwavelength model of galaxy formation. *MNRAS*, 462:3854–3911. 14

Lacki, B. C. and Thompson, T. A. (2010). The Physics of the Far-infrared-Radio Correlation. II. Synchrotron Emission as a Star Formation Tracer in High-redshift Galaxies. *ApJ*, 717:196–208. 57, 71, 72, 77, 116

Lacki, B. C., Thompson, T. A., and Quataert, E. (2010). The Physics of the Far-infrared-Radio Correlation. I. Calorimetry, Conspiracy, and Implications. *ApJ*, 717:1–28. 20, 57

Lada, C. J., Lombardi, M., and Alves, J. F. (2009). The California Molecular Cloud. *ApJ*, 703:52–59. 107

Laigle, C., McCracken, H. J., Ilbert, O., Hsieh, B. C., Davidzon, I., et al. (2016). The COSMOS2015 Catalog: Exploring the 1 < z < 6 Universe with Half a Million Galaxies. *ApJS*, 224:24. 58, 59, 62, 65

Laing, R. A. and Bridle, A. H. (1987). Rotation measure variation across M84. *MNRAS*, 228:557–571. 8

Lang, D., Hogg, D. W., and Schlegel, D. J. (2014). WISE photometry for 400 million SDSS sources. *ArXiv e-prints*. 81, 84

Le Floc'h, E., Aussel, H., Ilbert, O., Riguccini, L., Frayer, D. T., et al. (2009). Deep Spitzer 24 μm COSMOS Imaging. I. The Evolution of Luminous Dusty Galaxies - Confronting the Models. *ApJ*, 703:222–239. 58

Leavitt, H. S. and Pickering, E. C. (1912). Periods of 25 Variable Stars in the Small Magellanic Cloud. *Harvard College Observatory Circular*, 173:1–3. 2

Ledlow, M. J. and Owen, F. N. (1996). 20 CM VLA Survey of Abell Clusters of Galaxies. VI. Radio/Optical Luminosity Functions. *AJ*, 112:9. 7

Leroy, A. K., Walter, F., Brinks, E., Bigiel, F., de Blok, W. J. G., et al. (2008). The Star Formation Efficiency in Nearby Galaxies: Measuring Where Gas Forms Stars Effectively. *AJ*, 136:2782–2845. 51, 52

Letawe, G. and Magain, P. (2010). Deep near-infrared imaging of the HE0450-2958 system. *A&A*, 515:A84. 33, 35, 45, 50

Letawe, G., Magain, P., Chantry, V., and Letawe, Y. (2009). Near-infrared observations of the HE0450-2958 system: discovery of a second active galactic nucleus? *MNRAS*, 396:78–84. 45

Letawe, G., Magain, P., and Courbin, F. (2008). Slit and integral-field optical spectroscopy of the enigmatic quasar HE 0450-2958. *A&A*, 480:69–77. 33, 35, 43, 49, 50, 53

Lutz, D., Poglitsch, A., Altieri, B., Andreani, P., Aussel, H., et al. (2011). PACS Evolutionary Probe (PEP) - A Herschel key program. *A&A*, 532:A90. 58

MacLaren, I., Richardson, K. M., and Wolfendale, A. W. (1988). Corrections to virial estimates of molecular cloud masses. *ApJ*, 333:821–825. 11, 113, 119

Madau, P. and Dickinson, M. (2014). Cosmic Star-Formation History. *ARA&A*, 52:415–486. 6, 14, 15

Magain, P., Letawe, G., Courbin, F., Jablonka, P., Jahnke, K., et al. (2005). Discovery of a bright quasar without a massive host galaxy; M05. *Nature*, 437:381–384. 33

Magnelli, B., Ivison, R. J., Lutz, D., Valtchanov, I., Farrah, D., et al. (2015). The far-infrared/radio correlation and radio spectral index of galaxies in the SFR-M plane up to z ~ 2. *A&A*, 573:A45. 57, 71, 79

Magorrian, J., Tremaine, S., Richstone, D., Bender, R., Bower, G., et al. (1998). The Demography of Massive Dark Objects in Galaxy Centers. *AJ*, 115:2285–2305. 14, 32, 33

Mao, M. Y., Huynh, M. T., Norris, R. P., Dickinson, M., Frayer, D., et al. (2011). No Evidence for Evolution in the Far-infrared-Radio Correlation out to z ~ 2 in the Extended Chandra Deep Field South. *ApJ*, 731:79. 56, 79

Marchesi, S., Civano, F., Elvis, M., Salvato, M., Brusa, M., et al. (2016). The Chandra COSMOS Legacy survey: optical/IR identifications. *ApJ*, 817:34. 62

Marconi, A. and Hunt, L. K. (2003). The Relation between Black Hole Mass, Bulge Mass, and Near-Infrared Luminosity. *ApJ*, 589:L21–L24. 32

Marvil, J., Owen, F., and Eilek, J. (2015). Integrated Radio Continuum Spectra of Galaxies. *AJ*, 149:32. 75

Matthews, T. A. and Sandage, A. R. (1963). Optical Identification of 3C 48, 3C 196, and 3C 286 with Stellar Objects. *ApJ*, 138:30. 6

McCarthy, P. J., van Breugel, W., Spinrad, H., and Djorgovski, S. (1987). A correlation between the radio and optical morphologies of distant 3Cr radio galaxies. *ApJ*, 321:L29–L33. 53

McLure, R. J. and Dunlop, J. S. (2001). The black hole masses of Seyfert galaxies and quasars. *MNRAS*, 327:199–207. 32

McLure, R. J. and Dunlop, J. S. (2002). On the black hole-bulge mass relation in active and inactive galaxies. *MNRAS*, 331:795–804. 32

Merritt, D., Storchi-Bergmann, T., Robinson, A., Batcheldor, D., Axon, D., and Cid Fernandes, R. (2006). The nature of the HE0450-2958 system. *MNRAS*, 367:1746–1750. 33

Molnár, D. C., Sargent, M. T., Delhaize, J., Delvecchio, I., Smolčić, V., et al. (2018). The infrared-radio correlation of spheroid- and disc-dominated star-forming galaxies to z ∼ 1.5 in the COSMOS field. *MNRAS*, 475:827–838. 98

Montillaud, J., Juvela, M., Rivera-Ingraham, A., Malinen, J., Pelkonen, V.-M., et al. (2015). Galactic cold cores. IV. Cold submillimetre sources: catalogue and statistical analysis. *A&A*, 584:A92. 105, 107

Morić, I., Smolčić, V., Kimball, A., Riechers, D. A., Ivezić, Ž., and Scoville, N. (2010). A Closer View of the Radio-FIR Correlation: Disentangling the Contributions of Star Formation and Active Galactic Nucleus Activity. *ApJ*, 724:779–790. 96, 98, 116

Mullaney, J. R., Daddi, E., Béthermin, M., Elbaz, D., Juneau, S., et al. (2012). The Hidden "AGN Main Sequence": Evidence for a Universal Black Hole Accretion to Star Formation Rate Ratio since z ∼ 2 Producing an M $_{BH}$-M $_{*}$ Relation. *ApJ*, 753:L30. 14, 32, 75

Murphy, E. J. (2009). The Far-Infrared-Radio Correlation at High Redshifts: Physical Considerations and Prospects for the Square Kilometer Array. *ApJ*, 706:482–496. 56, 57

Murphy, E. J., Bremseth, J., Mason, B. S., Condon, J. J., Schinnerer, E., et al. (2012). The Star Formation in Radio Survey: GBT 33 GHz Observations of Nearby Galaxy Nuclei and Extranuclear Star-forming Regions. *ApJ*, 761:97. 56

Murphy, E. J., Condon, J. J., Schinnerer, E., Kennicutt, R. C., Calzetti, D., et al. (2011). Calibrating Extinction-free Star Formation Rate Diagnostics with 33 GHz Free-free Emission in NGC 6946. *ApJ*, 737:67. 56

Murphy, E. J., Momjian, E., Condon, J. J., Chary, R.-R., Dickinson, M., et al. (2017). The GOODS-N Jansky VLA 10 GHz Pilot Survey: Sizes of Star-forming μJY Radio Sources. *ApJ*, 839:35. 28, 72, 75

Murray, N. (2011). Star Formation Efficiencies and Lifetimes of Giant Molecular Clouds in the Milky Way. *ApJ*, 729:133. 11

Nelson, E. J., van Dokkum, P. G., Förster Schreiber, N. M., Franx, M., Brammer, G. B., et al. (2016). Where Stars Form: Inside-out Growth and Coherent Star Formation from HST Hα Maps of 3200 Galaxies across the Main Sequence at 0.7 < z < 1.5. *ApJ*, 828:27. 72

Nesvadba, N. P. H., Boulanger, F., Lehnert, M. D., Guillard, P., and Salome, P. (2011). Dense gas without star formation: the kpc-sized turbulent molecular disk in 3C 326 N. *A&A*, 536:L5. 13, 32, 53

Neugebauer, G., Habing, H. J., van Duinen, R., Aumann, H. H., Baud, B., Beichman, C. A., et al. (1984). The Infrared Astronomical Satellite (IRAS) mission. *ApJ*, 278:L1–L6. 79, 84

Niklas, S., Klein, U., and Wielebinski, R. (1997). A radio continuum survey of Shapley-Ames galaxies at λ 2.8cm. II. Separation of thermal and non-thermal radio emission. *A&A*, 322:19–28. 75

Noeske, K. G., Weiner, B. J., Faber, S. M., Papovich, C., Koo, D. C., Somerville, R. S., et al. (2007). Star Formation in AEGIS Field Galaxies since z=1.1: The Dominance of Gradually Declining Star Formation, and the Main Sequence of Star-forming Galaxies. *ApJ*, 660:L43–L46. 5

Norris, R. P., Afonso, J., Appleton, P. N., Boyle, B. J., Ciliegi, P., et al. (2006). Deep ATLAS Radio Observations of the Chandra Deep Field-South/Spitzer Wide-Area Infrared Extragalactic Field. *AJ*, 132:2409–2423. 21, 56

Norris, R. P., Kesteven, M. J., Wellington, K. J., and Batty, M. J. (1988). The Parkes-Tidbinbilla interferometer. *ApJS*, 67:85–91. 49

Nyland, K., Harwood, J. J., Mukherjee, D., Jagannathan, P., Rujopakarn, W., et al. (2018). Revolutionizing Our Understanding of AGN Feedback and its Importance to Galaxy Evolution in the Era of the Next Generation Very Large Array. *ArXiv e-prints*. 29

Nyland, K., Young, L. M., Wrobel, J. M., Davis, T. A., Bureau, M., et al. (2017). Star formation in nearby early-type galaxies: the radio continuum perspective. *MNRAS*, 464:1029–1064. 75, 117

O'Dea, C. P. (1998). The Compact Steep-Spectrum and Gigahertz Peaked-Spectrum Radio Sources. *PASP*, 110:493–532. 47

Oesch, P. A., Carollo, C. M., Feldmann, R., Hahn, O., Lilly, S. J., et al. (2010). The Buildup of the Hubble Sequence in the Cosmos Field. *ApJ*, 714:L47–L51. 62

Oliver, S. J., Bock, J., Altieri, B., Amblard, A., Arumugam, V., et al. (2012). The Herschel Multi-tiered Extragalactic Survey: HerMES. *MNRAS*, 424:1614–1635. 58

Osterbrock, D. E. (1981). Seyfert galaxies with weak broad H alpha emission lines. *ApJ*, 249:462–470. 7

Oteo, I., Ivison, R. J., Dunne, L., Smail, I., Swinbank, A. M., et al. (2016). Witnessing the Birth of the Red Sequence: ALMA High-resolution Imaging of [C II] and Dust in Two Interacting Ultra-red Starbursts at z = 4.425. *ApJ*, 827:34. 32

Oteo, I., Zwaan, M. A., Ivison, R. J., Smail, I., and Biggs, A. D. (2017). ALMACAL II: Extreme Star Formation Rate Densities in Dusty Starbursts Revealed by ALMA 20 mas Resolution Imaging. *ApJ*, 837:182. 32

Ott, M., Witzel, A., Quirrenbach, A., Krichbaum, T. P., Standke, K. J., et al. (1994). An updated list of radio flux density calibrators. *A&A*, 284:331–339. 108

Pannella, M., Elbaz, D., Daddi, E., Dickinson, M., Hwang, H. S., et al. (2015). GOODS-Herschel: Star Formation, Dust Attenuation, and the FIR-radio Correlation on the Main Sequence of Star-forming Galaxies up to z 4. *ApJ*, 807:141. 57

Papadopoulos, P. P., Feain, I. J., Wagg, J., and Wilner, D. J. (2008). A New Twist to an Old Story: HE 0450-2958 and the ULIRG – Optically Bright QSO Transition Hypothesis. *ApJ*, 684:845–852. 13, 34, 35, 49, 50, 51, 52

Papadopoulos, P. P., Greve, T. R., Ivison, R. J., and De Breuck, C. (2005). A sensitive search for CO J = 1-0 emission in 4C 41.17: high-excitation molecular gas at z = 3.8. *A&A*, 444:813–819. 52

Papadopoulos, P. P., van der Werf, P., Xilouris, E., Isaak, K. G., and Gao, Y. (2012). The Molecular Gas in Luminous Infrared Galaxies. II. Extreme Physical Conditions and Their Effects on the X $_{co}$ Factor. *ApJ*, 751:10. 51

Park, S. Q., Barmby, P., Fazio, G. G., Nandra, K., Laird, E. S., et al. (2008). AEGIS: Radio and Mid-Infrared Selection of Obscured AGN Candidates. *ApJ*, 678:744–750. 56

Patil, A. H., Yatawatta, S., Koopmans, L. V. E., de Bruyn, A. G., Brentjens, M. A., et al. (2017). Upper Limits on the 21 cm Epoch of Reionization Power Spectrum from One Night with LOFAR. *ApJ*, 838:65. 29

Peng, C. Y. (2007). How Mergers May Affect the Mass Scaling Relation between Gravitationally Bound Systems. *ApJ*, 671:1098–1107. 32

Pérez-Torres, M. A., Romero-Cañizales, C., Alberdi, A., and Polatidis, A. (2009). An extremely prolific supernova factory in the buried nucleus of the starburst galaxy IC 694. *A&A*, 507:L17–L20. 20

Pilbratt, G. L., Riedinger, J. R., Passvogel, T., Crone, G., Doyle, D., et al. (2010). Herschel Space Observatory. An ESA facility for far-infrared and submillimetre astronomy. *A&A*, 518:L1. 57, 81

Planck Collaboration, Ade, P. A. R., Aghanim, N., Armitage-Caplan, C., Arnaud, M., Ashdown, M., et al. (2014). Planck 2013 results. XVI. Cosmological parameters. *A&A*, 571:A16. 35

Planck Collaboration, Ade, P. A. R., Aghanim, N., Arnaud, M., Ashdown, M., Aumont, J., et al. (2011). Planck early results. XXIII. The first all-sky survey of Galactic cold clumps. *A&A*, 536:A23. 104

Planck Collaboration, Ade, P. A. R., Aghanim, N., Arnaud, M., Ashdown, M., Aumont, J., et al. (2016). Planck 2015 results. XIII. Cosmological parameters. *A&A*, 594:A13. 2

Poglitsch, A., Waelkens, C., Geis, N., Feuchtgruber, H., Vandenbussche, B., et al. (2010). The Photodetector Array Camera and Spectrometer (PACS) on the Herschel Space Observatory. *A&A*, 518:L2. 58, 84

Qiu, J., Shi, Y., Wang, J., Zhang, Z.-Y., and Zhou, L. (2017). The Dependence of the IR-Radio Correlation on the Metallicity. *ApJ*, 846:68. 79

Rau, U. and Cornwell, T. J. (2011). A multi-scale multi-frequency deconvolution algorithm for synthesis imaging in radio interferometry. *A&A*, 532:A71. 27, 37

Renaud, F., Kraljic, K., and Bournaud, F. (2012). Star Formation Laws and Thresholds from Interstellar Medium Structure and Turbulence. *ApJ*, 760:L16. 53

Rivera-Ingraham, A., Ristorcelli, I., Juvela, M., Montillaud, J., Men'shchikov, A., et al. (2016). Galactic cold cores. VII. Filament formation and evolution: Methods and observational constraints. *A&A*, 591:A90. 105

Rivera-Ingraham, A., Ristorcelli, I., Juvela, M., Montillaud, J., Men'shchikov, A., et al. (2017). Galactic cold cores. VIII. Filament formation and evolution: Filament properties in context with evolutionary models. *A&A*, 601:A94. 105

Roseboom, I. G., Ivison, R. J., Greve, T. R., Amblard, A., Arumugam, V., et al. (2012). The Herschel Multi-tiered Extragalactic Survey: SPIRE-mm photometric redshifts. *MNRAS*, 419:2758–2773. 85

Rowan-Robinson, M. (1977). On the unity of activity in galaxies. *ApJ*, 213:635–647. 7

Rowlands, K., Dunne, L., Dye, S., Aragón-Salamanca, A., Maddox, S., et al. (2014). Herschel-ATLAS: properties of dusty massive galaxies at low and high redshifts. *MNRAS*, 441:1017–1039. 65

Roy, A. L., Norris, R. P., Kesteven, M. J., Troup, E. R., and Reynolds, J. E. (1994). Compact radio cores in Seyfert galaxies. *ApJ*, 432:496–507. 49

Rujopakarn, W., Dunlop, J. S., Rieke, G. H., Ivison, R. J., Cibinel, A., et al. (2016). VLA and ALMA Imaging of Intense Galaxy-wide Star Formation in z ~ 2 Galaxies. *ApJ*, 833:12. 72

Rush, B., Malkan, M. A., and Edelson, R. A. (1996). The Radio Properties of Seyfert Galaxies in the 12 Micron and CfA Samples. *ApJ*, 473:130. 39

Ryle, M. and Vonberg, D. D. (1946). Solar Radiation on 175 Mc./s. *Nature*, 158:339–340. 24

Saintonge, A., Kauffmann, G., Wang, J., Kramer, C., Tacconi, L. J., et al. (2011). COLD GASS, an IRAM legacy survey of molecular gas in massive galaxies - II. The non-universality of the molecular gas depletion time-scale. *MNRAS*, 415:61–76. 51, 116

Sajina, A., Yan, L., Lutz, D., Steffen, A., Helou, G., et al. (2008). Spitzer Mid-Infrared Spectroscopy of Infrared Luminous Galaxies at z ∼ 2. III. Far-IR to Radio Properties and Optical Spectral Diagnostics. *ApJ*, 683:659–682. 56

Salomé, Q., Salomé, P., and Combes, F. (2015). Jet-induced star formation in 3C 285 and Minkowski's Object. *A&A*, 574:A34. 13, 53

Salpeter, E. E. (1955). The Luminosity Function and Stellar Evolution. *ApJ*, 121:161. 4

Sanders, D. B., Mazzarella, J. M., Kim, D.-C., Surace, J. A., and Soifer, B. T. (2003). The IRAS Revised Bright Galaxy Sample. *AJ*, 126:1607–1664. 52

Sanders, D. B. and Mirabel, I. F. (1996). Luminous Infrared Galaxies. *ARA&A*, 34:749. 52

Santos, M. G., Cluver, M., Hilton, M., Jarvis, M., Jozsa, G. I. G., et al. (2017). MeerKLASS: MeerKAT Large Area Synoptic Survey. *ArXiv e-prints*. 29

Sargent, M. T., Béthermin, M., Daddi, E., and Elbaz, D. (2012). The Contribution of Starbursts and Normal Galaxies to Infrared Luminosity Functions at z < 2. *ApJ*, 747:L31. 6

Sargent, M. T., Carollo, C. M., Lilly, S. J., Scarlata, C., Feldmann, R., et al. (2007). The Evolution of the Number Density of Large Disk Galaxies in COSMOS. *ApJS*, 172:434–455. 59

Sargent, M. T., Daddi, E., Béthermin, M., Aussel, H., Magdis, G., et al. (2014). Regularity Underlying Complexity: A Redshift-independent Description of the Continuous Variation of Galaxy-scale Molecular Gas Properties in the Mass-star Formation Rate Plane. *ApJ*, 793:19. 6, 51, 60

Sargent, M. T., Schinnerer, E., Murphy, E., Aussel, H., Le Floc'h, E., et al. (2010). The VLA-COSMOS Perspective on the Infrared-Radio Relation. I. New Constraints on Selection Biases and the Non-Evolution of the Infrared/Radio Properties of Star-Forming and Active Galactic Nucleus Galaxies at Intermediate and High Redshift. *ApJS*, 186:341–377. 51, 56, 58, 67, 79, 80, 81, 88, 92, 98, 116

Scarlata, C., Carollo, C. M., Lilly, S., Sargent, M. T., Feldmann, R., et al. (2007). COSMOS Morphological Classification with the Zurich Estimator of Structural Types (ZEST) and the Evolution Since z = 1 of the Luminosity Function of Early, Disk, and Irregular Galaxies. *ApJS*, 172:406–433. 59, 62

Schaye, J., Crain, R. A., Bower, R. G., Furlong, M., Schaller, M., et al. (2015). The EAGLE project: simulating the evolution and assembly of galaxies and their environments. *MNRAS*, 446:521–554. 15

Schechter, P. (1976). An analytic expression for the luminosity function for galaxies. *ApJ*, 203:297–306. 12, 13

Schiminovich, D., van Gorkom, J. H., van der Hulst, J. M., and Kasow, S. (1994). Discovery of Neutral Hydrogen Associated with the Diffuse Shells of NGC 5128 (Centaurus A). *ApJ*, 423:L101. 13, 52

Schinnerer, E., Sargent, M. T., Bondi, M., Smolčić, V., Datta, A., et al. (2010). The VLA-COSMOS Survey. IV. Deep Data and Joint Catalog. *ApJS*, 188:384–404. 56, 63

Schinnerer, E., Smolčić, V., Carilli, C. L., Bondi, M., Ciliegi, P., et al. (2007). The VLA-COSMOS Survey. II. Source Catalog of the Large Project. *ApJS*, 172:46–69. 56, 59

Schleicher, D. R. G. and Beck, R. (2013). A new interpretation of the far-infrared - radio correlation and the expected breakdown at high redshift. *A&A*, 556:A142. 57

Schmidt, M. (1963). 3C 273 : A Star-Like Object with Large Red-Shift. *Nature*, 197:1040. 6

Schmitt, J. H. M. M., Kahabka, P., Stauffer, J., and Piters, A. J. M. (1993). ROSAT All-Sky X-Ray Survey of the Core Region of the Pleiades Cluster. *A&A*, 277:114. 66, 67

Schreiber, C., Pannella, M., Elbaz, D., Béthermin, M., Inami, H., et al. (2015). The Herschel view of the dominant mode of galaxy growth from z = 4 to the present day. *A&A*, 575:A74. 5

Schwab, F. R. (1984). Optimal Gridding of Visibility Data in Radio Interferometry. In Roberts, J. A., editor, *Indirect Imaging. Measurement and Processing for Indirect Imaging*, pages 333–346. 27

Scoville, N., Arnouts, S., Aussel, H., Benson, A., Bongiorno, A., et al. (2013). Evolution of Galaxies and Their Environments at z = 0.1-3 in COSMOS. *ApJS*, 206:3. 98

Scoville, N., Aussel, H., Brusa, M., Capak, P., Carollo, C. M., et al. (2007). The Cosmic Evolution Survey (COSMOS): Overview. *ApJS*, 172:1–8. 28, 56

Seyfert, C. K. (1943). Nuclear Emission in Spiral Nebulae. *ApJ*, 97:28. 7

Silk, J. (2005). Ultraluminous starbursts from supermassive black hole-induced outflows. *MNRAS*, 364:1337–1342. 32

Silk, J. (2013). Unleashing Positive Feedback: Linking the Rates of Star Formation, Supermassive Black Hole Accretion, and Outflows in Distant Galaxies. *ApJ*, 772:112. 13, 32

Silk, J. and Mamon, G. A. (2012). The current status of galaxy formation. *Research in Astronomy and Astrophysics*, 12:917–946. 13, 14, 32

Silk, J. and Norman, C. (2009). Global Star Formation Revisited. *ApJ*, 700:262–275. 32

Simard, L., Mendel, J. T., Patton, D. R., Ellison, S. L., and McConnachie, A. W. (2011). A Catalog of Bulge+disk Decompositions and Updated Photometry for 1.12 Million Galaxies in the Sloan Digital Sky Survey. *ApJS*, 196:11. 117

Smith, D. J. B., Dunne, L., da Cunha, E., Rowlands, K., Maddox, S. J., et al. (2012). Herschel-ATLAS: multi-wavelength SEDs and physical properties of 250 μm selected galaxies at z < 0.5. *MNRAS*, 427:703–727. 66

Smith, D. J. B., Jarvis, M. J., Hardcastle, M. J., Vaccari, M., Bourne, N., et al. (2014). The temperature dependence of the far-infrared-radio correlation in the Herschel-ATLAS. *MNRAS*, 445:2232–2243. 56

Smolčić, V., Delvecchio, I., Zamorani, G., Baran, N., Novak, M., et al. (2017a). The VLA-COSMOS 3 GHz Large Project: Multiwavelength counterparts and the composition of the faint radio population. *A&A*, 602:A2. 58, 62

Smolčić, V., Novak, M., Bondi, M., Ciliegi, P., Mooley, K. P., et al. (2017b). The VLA-COSMOS 3 GHz Large Project: Continuum data and source catalog release. *A&A*, 602:A1. 28, 58

Speagle, J. S., Steinhardt, C. L., Capak, P. L., and Silverman, J. D. (2014). A Highly Consistent Framework for the Evolution of the Star-Forming "Main Sequence" from z ~ 0-6. *ApJS*, 214:15. 5

Springel, V., White, S. D. M., Jenkins, A., Frenk, C. S., Yoshida, N., et al. (2005). Simulations of the formation, evolution and clustering of galaxies and quasars. *Nature*, 435:629–636. 12

Symeonidis, M., Georgakakis, A., Page, M. J., Bock, J., Bonzini, M., et al. (2014). Linking the X-ray and infrared properties of star-forming galaxies at z <1.5. *MNRAS*, 443:3728–3740. 18, 74

Symeonidis, M., Giblin, B. M., Page, M. J., Pearson, C., Bendo, G., et al. (2016). AGN are cooler than you think: the intrinsic far-IR emission from QSOs. *MNRAS*, 459:257–276. 8, 21

Szokoly, G. P., Bergeron, J., Hasinger, G., Lehmann, I., Kewley, L., et al. (2004). The Chandra Deep Field-South: Optical Spectroscopy. I. *ApJS*, 155:271–349. 21

Tabatabaei, F. S., Beck, R., Krügel, E., Krause, M., Berkhuijsen, E. M., Gordon, K. D., and Menten, K. M. (2007). High-resolution radio continuum survey of M 33. II. Thermal and nonthermal emission. *A&A*, 475:133–143. 18

Tabatabaei, F. S., Schinnerer, E., Krause, M., Dumas, G., Meidt, S., et al. (2017). The Radio Spectral Energy Distribution and Star-formation Rate Calibration in Galaxies. *ApJ*, 836:185. 20

Tacchella, S., Dekel, A., Carollo, C. M., Ceverino, D., DeGraf, C., et al. (2016). The confinement of star-forming galaxies into a main sequence through episodes of gas compaction, depletion and replenishment. *MNRAS*, 457:2790–2813. 5

Tauber, J. A., Mandolesi, N., Puget, J.-L., Banos, T., Bersanelli, M., et al. (2010). Planck pre-launch status: The Planck mission. *A&A*, 520:A1. 104

Tomczak, A. R., Quadri, R. F., Tran, K.-V. H., Labbé, I., Straatman, C. M. S., et al. (2016). The SFR-M* Relation and Empirical Star-Formation Histories from ZFOURGE* at 0.5 < z < 4. *ApJ*, 817:118. 5

Tunnard, R., Greve, T. R., Garcia-Burillo, S., Graciá Carpio, J., Fischer, J., et al. (2015). Chemically Distinct Nuclei and Outflowing Shocked Molecular Gas in Arp 220. *ApJ*, 800:25. 32

Urry, C. M. and Padovani, P. (1995). Unified Schemes for Radio-Loud Active Galactic Nuclei. *PASP*, 107:803. 7

Valiante, E., Smith, M. W. L., Eales, S., Maddox, S. J., Ibar, E., et al. (2016). The Herschel-ATLAS data release 1 - I. Maps, catalogues and number counts. *MNRAS*, 462:3146–3179. 84

van Breugel, W. J. M. and Dey, A. (1993). Induced star formation in a radio lobe of 3C 285? *ApJ*, 414:563–572. 52

van der Kruit, P. C. (1971). Observations of core sources in Seyfert and normal galaxies with the Westerbork synthesis radio telescope at 1415 MHz. *A&A*, 15:110–122. 20, 56, 79

van der Kruit, P. C. (1973). High-resolution Radio Continuum Observations of Bright Spiral Galaxies at 1415 MHz: A General Discussion. *A&A*, 29:263. 20, 56, 79

van Haarlem, M. P., Wise, M. W., Gunst, A. W., Heald, G., McKean, J. P., et al. (2013). LOFAR: The LOw-Frequency ARray. *A&A*, 556:A2. 29, 57

Viero, M. P., Asboth, V., Roseboom, I. G., Moncelsi, L., Marsden, G., et al. (2014). The Herschel Stripe 82 Survey (HerS): Maps and Early Catalog. *ApJS*, 210:22. 84, 85

Voelk, H. J. (1989). The correlation between radio and far-infrared emission for disk galaxies - A calorimeter theory. *A&A*, 218:67–70. 20, 57

Vogelsberger, M., Genel, S., Springel, V., Torrey, P., Sijacki, D., et al. (2014). Introducing the Illustris Project: simulating the coevolution of dark and visible matter in the Universe. *MNRAS*, 444:1518–1547. 15

Wang, L., Rowan-Robinson, M., Norberg, P., Heinis, S., and Han, J. (2014a). The Revised IRAS-FSC Redshift Catalogue (RIFSCz). *MNRAS*, 442:2739–2750. 84

Wang, L., Viero, M., Clarke, C., Bock, J., Buat, V., et al. (2014b). HerMES: point source catalogues from Herschel-SPIRE observations II. *MNRAS*, 444:2870–2883. 85

Whitaker, K. E., van Dokkum, P. G., Brammer, G., and Franx, M. (2012). The Star Formation Mass Sequence Out to z = 2.5. *ApJ*, 754:L29. 5, 17

Wilson, T. L., Rohlfs, K., and Hüttemeister, S. (2009). *Tools of Radio Astronomy*. Springer-Verlag. 23, 25

Wright, E. L., Eisenhardt, P. R. M., Mainzer, A. K., Ressler, M. E., Cutri, R. M., et al. (2010). The Wide-field Infrared Survey Explorer (WISE): Mission Description and Initial On-orbit Performance. *AJ*, 140:1868–1881. 84

Wu, Y., Liu, T., Meng, F., Li, D., Qin, S.-L., and Ju, B.-G. (2012). Gas Emissions in Planck Cold Dust Clumps – A Survey of the J = 1-0 Transitions of ^{12}CO, ^{13}CO, and C^{18}O. *ApJ*, 756:76. 107

Wuyts, S., Förster Schreiber, N. M., van der Wel, A., Magnelli, B., Guo, Y., et al. (2011). Galaxy Structure and Mode of Star Formation in the SFR-Mass Plane from z $\sim$ 2.5 to z $\sim$ 0.1. *ApJ*, 742:96. 61

Yun, M. S., Reddy, N. A., and Condon, J. J. (2001). Radio Properties of Infrared-selected Galaxies in the IRAS 2 Jy Sample. *ApJ*, 554:803–822. 20, 50, 51, 56, 58, 78, 79, 80, 86, 92, 95, 96, 100, 116